TOWARD SIMULATING COMPLEX SYSTEMS WITH QUANTUM EFFECTS

A Dissertation

Presented to the Faculty of the Graduate School

of Cornell University

in Partial Fulfillment of the Requirements for the Degree of

Doctor of Philosophy

by

Rachel Lynn Kenion-Hanrath

January 2017

TOWARD SIMULATING COMPLEX SYSTEMS WITH QUANTUM EFFECTS

Rachel Lynn Kenion-Hanrath, Ph.D.

Cornell University 2017

Quantum effects like tunneling, coherence, and zero point energy often play a significant role in phenomena on the scales of atoms and molecules. However, the exact quantum treatment of a system scales exponentially with dimensionality, making it impractical for characterizing reaction rates and mechanisms in complex systems. An ongoing effort in the field of theoretical chemistry and physics is extending scalable, classical trajectory-based simulation methods capable of capturing quantum effects to describe dynamic processes in many-body systems; in the work presented here we explore two such techniques.

First, we detail an explicit electron, path integral (PI)-based simulation protocol for predicting the rate of electron transfer in condensed-phase transition metal complex systems [1]. Using a PI representation of the transferring electron and a classical representation of the transition metal complex and solvent atoms, we compute the outer sphere free energy barrier and dynamical recrossing factor of the electron transfer rate while accounting for quantum tunneling and zero point energy effects. We are able to achieve this employing only a single set of force field parameters to describe the system rather than parameterizing along the reaction coordinate. Following our success in describing a simple model system, we discuss our next steps in extending our protocol to technologically relevant materials systems.

The latter half focuses on the Mixed Quantum-Classical Initial Value Repre-

sentation (MQC-IVR) [2] of real-time correlation functions, a semiclassical method which has demonstrated its ability to "tune" between quantum- and classical-limit correlation functions while maintaining dynamic consistency. Specifically, this is achieved through a parameter that determines the quantumness of individual degrees of freedom. Here, we derive a semiclassical correction term for the MQC-IVR to systematically characterize the error introduced by different choices of simulation parameters, and demonstrate the ability of this approach to optimize MQC-IVR simulations.

BIOGRAPHICAL SKETCH

Rachel Kenion-Hanrath grew up in northeastern Pennsylvania. She attended New York University, initially having declared her major in Chemistry, and later decided to pursue Chemical Engineering as well through a dual-degree program with Stevens Institute of Technology. In 2011, she began her tenure as a graduate student at Cornell University, where she worked under the guidance of Professor Nandini Ananth.

This is for you, Max.

ACKNOWLEDGEMENTS

A special thanks to my adviser Professor Nandini Ananth, for all of her patient guidance and support. Thank you to all past and present members of the Ananth group for the many stimulating research discussions and good company at lunch. Finally, thank you to my friends and family for their love and encouragement.

This work was funded by a National Science Foundation Graduate Research Fellowship under Grant No. DGE-1144153, a startup grant from Cornell University, the President's Council of Cornell Women Affinito-Stewart Grant, and a Cottrell Scholar Award. This work used the Extreme Science and Engineering Discovery Environment, which is supported by National Science Foundation grant number ACI-1053575.

Chapter 2 was reproduced from Ref. [1] with permission from the PCCP Owner Societies.

TABLE OF CONTENTS

LIST OF TABLES

LIST OF FIGURES

LIST OF ABBREVIATIONS

DSC	Dye-sensitized Solar Cell
FB-IVR	Forward-Backward Initial Value Representation
MC	Monte Carlo
MD	molecular dynamics
MQC-IVR	Mixed Quantum-Classical Initial Value Representation
PI	Path Integral
eePI	explicit electron Path Integral
PIMD	Path Integral Molecular Dynamics
RP	Ring Polymer
RPMD	Ring Polymer Molecular Dynamics
SC-IVR	Semiclassical Initial Value Representation
SPC	simple point charge
TMC	transition metal complex
TST	transition state theory
VV	Velocity-Verlet

CHAPTER 1

INTRODUCTION

Within the field of theoretical chemistry, there is great interest in extending simulation capabilities to describe charge and energy transfer processes in complex molecular systems. These phenomena are characterized by motion over disparate length and time scales, resulting in the challenging task of treating the coupling between the dynamics of electronic transitions, which are intrinsically quantum mechanical, and the more classically behaved surroundings. Exact quantum dynamic descriptions are out of reach at these scales, and so in general, we seek to find an optimal compromise between the desired accuracy of an exact treatment and the scalability of an empirically-fit, classical description. The work in this dissertation focuses on two different methods, both of which exploit the more scalable nature of classical trajectories in a way that enables us to capture quantum effects.

The first project uses path integral (PI)-based methods to incorporate quantum effects, whereby an exact mapping between a quantum mechanical particle and a classical "ring polymer" (RP) in an extended phase space enables us to extract equilibrium properties and approximate dynamics from molecular dynamics (MD) simulations [3]. These methods are well suited for condensed-phase systems given their ability to describe quantum zero point energy and tunneling effects. They have been particularly useful for calculating diffusion coefficients [4–9] and chemical reaction rates [10–14] in many-body model systems, and often times, offer a level of physical understanding of the role of quantum effects.

More recent efforts have focused on the application of these methods to broader, and more technologically relevant classes of systems: the dynamics of enzyme catalysis [15], diffusion of hydrogen on a nickel surface [16], the mechanism of proton

coupled electron transfer [17], and outer sphere charge transfer in solvated transition metal complexes (TMCs) [1, 18]. Detailed in Chapter 2 is one such effort [1], where we begin exploring the use of a RP electron to simulate electron transfer in condensed-phase TMC systems. TMCs are of increasing interest given their revived role in light harvesting systems, showing promise in dye-sensitized solar cells [19–22] and for artificial photosynthesis [23–27]. However, TMCs pose additional challenges for molecular simulation techniques: the geometries they adopt depend on both the chemical nature of the ligands and the oxidation state of the TMC which hinders a general and straightforward approach to parameterization, especially when describing electron transfer processes.

We propose overcoming the obstacle to parameterization by decoupling the energetic barrier to electron transfer that results from changes in the central coordination sphere of the TMC, from that which arises due to solvent rearrangement in response to a redistribution of charge. By decoupling these two effects, we could rely on electronic structure calculations to obtain the inner sphere reorganization, and atomistic PI-based simulations to compute the solvent barrier. Adopting a geometry intermediate to the two oxidation states at play when calculating the barrier due to solvent reorganization, we avoid using tunable force fields, and conveniently, also avoid biasing the system toward a particular reaction path. In Chapter 2, we detail our first attempt at this approach for a TMC to begin to get a sense for the validity of these assumptions. *Will the change in partial charges about the TMC caused by the RP electron tunneling between the donor and acceptor sites be sufficient for capturing the solvent response? Is a basic force field description sufficient for this purpose?*

In Chapter 3, we provide a detailed description of the modifications to the

DL_POLY software package to include particles in the path integral representation. Then, in Chapter 4, we begin to lay out the next steps toward applying this approach to simulating electron transfer in more technologically relevant (and complex) TMC systems, proposing some related fundamental studies to explore the limits of this approach.

In Chapter 5, we shift to a more methodology-driven exploration. Whereas in the condensed-phase, quantum coherences often dampen rapidly and can be neglected, in the gas-phase this generally does not hold. Instead, when effects like quantum coherence and tunneling are at play, we turn to a semiclassical approach. Here, one exploits classical sampling trajectories evolved from initially quantized distributions to capture quantum effects. While these methods have been generally successful for small model systems, they are currently too computationally expensive to apply to complex systems. The mixed quantum-classical initial value representation (MQC-IVR) was recently developed in the Ananth group [2] as a dynamically consistent way to evaluate real-time correlation functions by individually treating system degrees of freedom with different levels of approximation. This way, we are able to simulate the system in a way that can describe quantum coherence effects for degrees of freedom where its deemed necessary, but can treat a majority of the modes more approximately to reduce the computational workload. This is of practical interest for the description of gas-phase reactions at metal surfaces, for example, where quantum coherence effects are important for a faithful representation of the observed energy transfer phenomena [28], but may not be necessary to describe the more distant surrounding modes of the metal lattice. However, while the full classical- and semiclassical-limiting cases of the MQC-IVR are well-defined, the mixed limit scenario—where the primary system is treated in the full semiclassical limit and its surroundings in the classical limit—

is less well understood. In Chapter 5, we derive two correction terms that can serve as a measure of error for comparing the 'tuning' and coherent state width parameters in the MQC-IVR. These efforts aim to quantify the error associated with the MQC-IVR and ultimately guide the choice of simulation parameters.

CHAPTER 2

DIRECT SIMULATION OF ELECTRON TRANSFER IN THE COBALT(III/II) HEXAMMINE SELF-EXCHANGE REACTION

2.1 Introduction

The redox reactions of transition metal complexes (TMCs) play a central role in biological processes such as photosynthesis and respiration [29–31], and in emerging renewable energy technologies including photocatalytic water splitting [23–27] and dye-sensitized solar cells [19–21]. Direct simulation of these electron transfer processes can provide the mechanistic insights necessary to better understand and control the redox reactions of TMCs. However, the inherently quantum nature of electron transfer and its coupling to collective nuclear motions of the extended complex and solvent molecules (outer sphere) as well as the immediate coordination environment of the metal center (inner sphere) pose a significant challenge to theory.

In recent years, developments in electronic structure approaches have made it possible to accurately calculate the inner sphere reorganization contribution to the total electron transfer free energy barrier [32–36]. However, calculating the outer sphere contribution remains an outstanding challenge [37,38]. Cavity models have had some success describing solvent effects using the polarizable continuum model, but they cannot provide information on the mechanistic role of solvent [39–42]. On-the-fly quantum mechanical/molecular mechanical dynamics have been used to perform atomistic simulations of TMC systems, and although they uncover some charge and energy transfer mechanisms [43–45], they are difficult to generalize. In addition, unphysical boundary effects due to feedback between the 'quan-

tum mechanical' region described by electronic structure and 'molecular mechanical' region described by force fields introduces uncontrolled approximations [46]. Molecular dynamics (MD) simulations, in contrast, employ a uniform dynamic framework, but rely on empirical force fields to describe both the TMC and its environment [47,48], and fail to account for quantum dynamic effects. Path Integral (PI)-based methods to simulate charge transfer [13, 17, 18, 49, 50] have emerged as a partial solution: they account for quantum effects using only classical MD trajectories. However, like MD, they rely on complex force field parameterization schemes.

Although modern force fields developed for TMCs are able to accurately capture coordination geometry [51–54], successfully describing changes to the TMC geometry and charge distribution that occur during an electron transfer reaction requires detailed re-parameterization. Existing simulation methods typically involve at least two independently parameterized force fields to describe the TMC reactant and product states in an electron transfer reaction. Over the course of the simulation, the force field is tuned between the two states based on parameters obtained from fitting to kinetic or non-kinetic experimental data [18,48,50,55,56]. While these methods have proven successful for a number of TMC systems, the need to explicitly tune the force field along an assumed and system-specific reaction coordinate renders them difficult to generalize and typically imposes a mechanistic bias that limits their predictive utility.

In this chapter, we describe a simplified protocol for the simulation of electron transfer in TMC reactions that leverages the effective separation between the inner and outer sphere contributions to the free energy barrier [57,58] and circumvents the need to parameterize a force field as the reaction progresses. We employ a sin-

gle set of standard force field parameters to describe the bonded and non-bonded interactions between metal, ligand and solvent atoms for the system in its reactant state. In addition, the transferring electron is treated as a distinguishable, excess electron that is represented as a ring polymer (RP) in the PI framework, [6, 13] and interacts electrostatically with all atoms in the simulation. We then calculate the outer sphere contribution to the electron transfer free energy barrier, explicitly accounting for quantum effects including tunneling, [59–61] using Path Integral Molecular Dynamics (PIMD) [62] along a reaction coordinate that tracks the position of the transferring electron RP [13]. In our PIMD simulation we eliminate contributions from inner sphere reorganization by fixing the metal-ligand bond lengths to their transition state values. The total free energy barrier to electron transfer is then determined by combining the calculated outer sphere contribution with values from the literature for the inner sphere reorganization energy [63, 64]. Finally, we estimate the reaction rate from a direct dynamic simulation of the electron transfer event using Ring Polymer Molecular Dynamics (RPMD) [3, 11, 13]. The ensemble of RPMD trajectories preserves detailed balance, yields a reaction rate that is independent of the choice of transition state, and analysis of this ensemble can be used to gain mechanistic insights including the role of solvent [13].

The prototype reaction studied here is the cobalt(III/II) hexammine electron self-exchange,

$$\mathrm{Co(NH_3)_6^{2+}} + \mathrm{Co(NH_3)_6^{3+}} \rightleftharpoons \mathrm{Co(NH_3)_6^{3+}} + \mathrm{Co(NH_3)_6^{2+}}. \tag{2.1}$$

This reaction has been extensively studied both experimentally and theoretically, but there is little agreement on the reaction rate [56, 63–75]. Experimental studies estimate rates in the range $\geq 10^{-7}$ $\mathrm{M^{-1}\ s^{-1}}$ at room temperature [70]. Using the protocol outlined here, we are able to calculate reaction rates from an atomistic simulation and achieve good agreement with experimental values. We emphasize

that our protocol, unlike previous work, does not rely on complex force field parameterization schemes and is equally applicable to both adiabatic and nonadiabatic electron transfer reactions.

2.2 Methodology

2.2.1 A brief introduction to path integral-based simulations

Consider the canonical partition function describing a quantum particle,

$$Z = \mathrm{Tr}\left[e^{-\beta\hat{H}}\right], \tag{2.2}$$

where $\beta = (k_B T)^{-1}$, k_B is the Boltzmann factor, T is the system temperature, and $\hat{H}$ is the system Hamiltonian. For a simple, one-dimensional Hamiltonian of the form

$$\hat{H} = \frac{\hat{p}^2}{2m} + U(\hat{q}), \tag{2.3}$$

with position and momentum operators, $\hat{q}$ and $\hat{p}$, respectively, and system potential $U(\hat{q})$, path integral discretization of the partition function enables its evaluation as

$$Z_{\mathrm{RP}} = \frac{1}{(2\pi\hbar)^n} \int d^n\mathbf{q} \int d^n\mathbf{v}\ e^{-\beta H_{\mathrm{RP}}(\mathbf{q},\mathbf{v})} \tag{2.4}$$

in the limit that $n \to \infty$, where v is velocity and $\hbar$ is the reduced Planck constant. The RP Hamiltonian derived in this way is [76]

$$H_{\mathrm{RP}}(\mathbf{q},\mathbf{v}) = \frac{1}{n}\sum_{\alpha=1}^{n}\left[\frac{1}{2}mv_\alpha^2 + \frac{1}{2}m\omega_n^2(q_\alpha - q_{\alpha-1})^2 + U(q_\alpha)\right], \tag{2.5}$$

with $\omega_n = n/(\beta\hbar)$ and $q_0 \equiv q_n$; its physical interpretation amounts to representing the initial quantum particle in classical phase space as a closed loop of n replicas of itself, or imaginary time path "beads", where neighboring beads interact by harmonic "springs" with frequency ω_n—this entity is referred to as a "ring polymer" (RP). Exploiting this convenient manipulation of the quantum partition function into a classically isomorphic RP enables us to run sampling trajectories with conventional MD approaches to extract exact equilibrium statistics.

The RP representation is introduced here to selectively quantize components of the simulation in a way that enables the incorporation of quantum effects, *i.e.* tunneling and zero point energy, in a scalable fashion. Here, we choose to quantize just the transferring electron. In the same vein as before, we express the canonical partition function of the system with an explicit, quantized electron interacting with classical atoms (both TMC and solvent in this case) in the path integral framework as,

$$Z = \lim_{n\to\infty} \frac{1}{(2\pi\hbar)^{n+N}} \int d^n\mathbf{q} \int d^n\mathbf{v} \int d^N\mathbf{Q} \int d^N\mathbf{V}\ e^{-\beta H_n(\mathbf{q},\mathbf{Q},\mathbf{v},\mathbf{V})}. \tag{2.6}$$

Here, n is the number of imaginary time path beads we employ for the electron, and N is the number of classical atoms in the system. In Eq. 2.6, the full system RP Hamiltonian is

$$H_n = \sum_{j=1}^{N} \frac{1}{2} M_j \mathbf{V}_j^2 + \sum_{\alpha=1}^{n} \frac{1}{2} m_b \mathbf{v}_\alpha^2 + U_n(\mathbf{q},\mathbf{Q}), \tag{2.7}$$

where, M_j and $\mathbf{V}_j$ are the mass and velocity associated with the j^{th} atom, $\mathbf{v}_\alpha$ is the velocity of the α^{th} electron RP bead, m_b denotes the fictitious Parrinello-Rahman RP bead mass [62, 77], $\mathbf{Q} \equiv \{\mathbf{Q}_j\}$ is the vector of classical atom positions, and $\mathbf{q} \equiv \{\mathbf{q}_\alpha\}$ is the vector of RP bead positions. The RP potential in Eq. 2.7 is

$$U_n(\mathbf{q},\mathbf{Q}) = \frac{1}{n} \sum_{\alpha=1}^{n} \frac{1}{2} m_e \omega_n^2 (\mathbf{q}_\alpha - \mathbf{q}_{\alpha-1})^2 + U(\mathbf{q},\mathbf{Q}) \tag{2.8}$$

where m_e is the electron mass, $\omega_n = nk_{\mathrm{B}}T/\hbar$, the electron RP is cyclic with $\mathbf{q}_0 = \mathbf{q}_n$, and $U(\mathbf{q}, \mathbf{Q})$ is the external potential that includes all atom-atom and atom-electron bead interactions. Additional details for the specific system under consideration here are provided in Section 2.3.2. The first term in Eq. 2.8 describes the harmonic interaction of the α^{th} bead with neighboring beads with characteristic frequency ω_n. We note that the Parrinello-Rahman mass, m_b, in Eq. 2.7 is an arbitrary parameter and can be chosen to enable efficient configurational sampling since all calculated statistical averages are independent of this choice. [62]

PIMD sampling trajectories are an exact approach to describing static equilibrium properties in the condensed-phase, where the assumption that quantum coherence effects do not contribute is valid. However, the extension of these methods to simulate quantum dynamics *via* real-time evolution of the RP, known as RPMD, was only originally suggested as an *ad hoc* approximation [10, 11, 78]. It was demonstrated in the short time limit that the RP correlation function is analogous to the exact Kubo transformed correlation function, and is exact for a harmonic oscillator [78]. RPMD rate theory had been successful in myriad applications [3, 4, 9, 12–15], but was lacking a systematic derivation. It was later shown that RPMD is an approximate form of Matsubara dynamics, offering insight into nature of the approximations inherent in RPMD [79,80]. However, it was not until more recently, that the RPMD approach was further validated by analogy to a quantum transition-state theory [81].

2.2.2 Reaction rate theory

Following the Bennett-Chandler approach [82], the RPMD reaction rate can be expressed as [11]

$$k_{\mathrm{RPMD}} = \lim_{t\to\infty} \kappa(t)\, k_{\mathrm{TST}}. \tag{2.9}$$

In Eq. 2.9, the transition state theory (TST) rate constant is defined as

$$k_{\mathrm{TST}} = (2\pi\beta)^{-1/2} \langle g_\xi \rangle_{\mathrm{c}} \frac{e^{-\beta\Delta G(\xi^\ddagger)}}{\int_{-\infty}^{\xi^\ddagger} d\xi\, e^{-\beta\Delta G(\xi)}}, \tag{2.10}$$

where ξ is a general reaction coordinate, the geometric factor $g_\xi(\mathbf{r}) = \left[\sum_{i=1}^{d} \frac{1}{m_i}\left(\frac{\partial\xi(\mathbf{r})}{\partial r_i}\right)^2\right]^{1/2}$ where $\mathbf{r}$ represents the full set of system degrees of freedom, and the notation $\langle\cdots\rangle_{\mathrm{c}}$ is used to indicate an ensemble average over trajectories initially restrained to the dividing surface, $\xi(\mathbf{r}) = \xi^\ddagger$. We further define $\Delta G(\xi)$ as the free energy difference of the system with configuration ξ and any arbitrarily chosen reference configuration in the reactant well. We compute the TST rate constant in Eq. 2.10 from a free energy profile computed along the reaction coordinate using standard umbrella sampling [83] and weighted histogram analysis methods [84], where a harmonic restraint is used to center simulation "windows" at different values of the reaction coordinate. Configurations within each window are sampled using classical MD trajectories generated by the Hamiltonian in Eq. 2.7 as is typical in a PIMD simulation.

Dynamic recrossing of the TST dividing surface in Eq. 2.9 is computed as,

$$\kappa(t) = \frac{\langle \dot{\xi}_0\, h[\xi(\mathbf{r}_t) - \xi^\ddagger]\rangle_{\mathrm{c}}}{\langle \dot{\xi}_0\, h[\dot{\xi}_0]\rangle_{\mathrm{c}}}, \tag{2.11}$$

where $\dot{\xi}_0$ is the initial velocity corresponding to the reaction coordinate, h is the Heaviside function, and $\xi(\mathbf{r}_t)$ denotes the system configuration at time t. Using the RPMD approach, the initial distribution is evolved in time using the RP Hamiltonian in Eq. 2.7 and setting the Parrinello Rahman mass to the physical mass of

the transferring electron, $m_b = m_e$ [11]. The transmission coefficient is obtained from the long-time limit of $\kappa(t)$.

2.2.3 Reaction coordinate for electron transfer

The reaction coordinate employed to describe the progress of the electron transfer reaction is a collective "bead-count" coordinate [13],

$$f_b(z_1, ..., z_n) = \frac{1}{n} \sum_{\alpha=1}^{n} \frac{1}{2} \left(\tanh(b z_\alpha) + 1 \right), \tag{2.12}$$

where z_α is the position along the z-axis of the α^{th} RP bead and $b = 1.25$ Å^{-1}. The bead-count coordinate tracks the fraction of RP beads on the electron donor and acceptor TMCs, changing continuously from 0 to 1 as the electron transfer reaction progresses.

2.3 Computational Details

2.3.1 Atomistic simulation details

The atomistic simulation includes 430 water molecules, two cobalt hexammine complexes and a 1024-bead RP as the excess electron. The Co metal centers are fixed to the apex-to-apex ligand shell van der Waals distance previously estimated using an *ab initio* crystal field model to be 7 Å [63, 64, 73], symmetric about the z-axis of a cubic simulation cell with side lengths 23.46 Å and periodic boundary conditions. In Figure 2.1, we show two snapshots of the solvated TMC system with the explicit RP electron from the atomistic simulation. The snapshots correspond

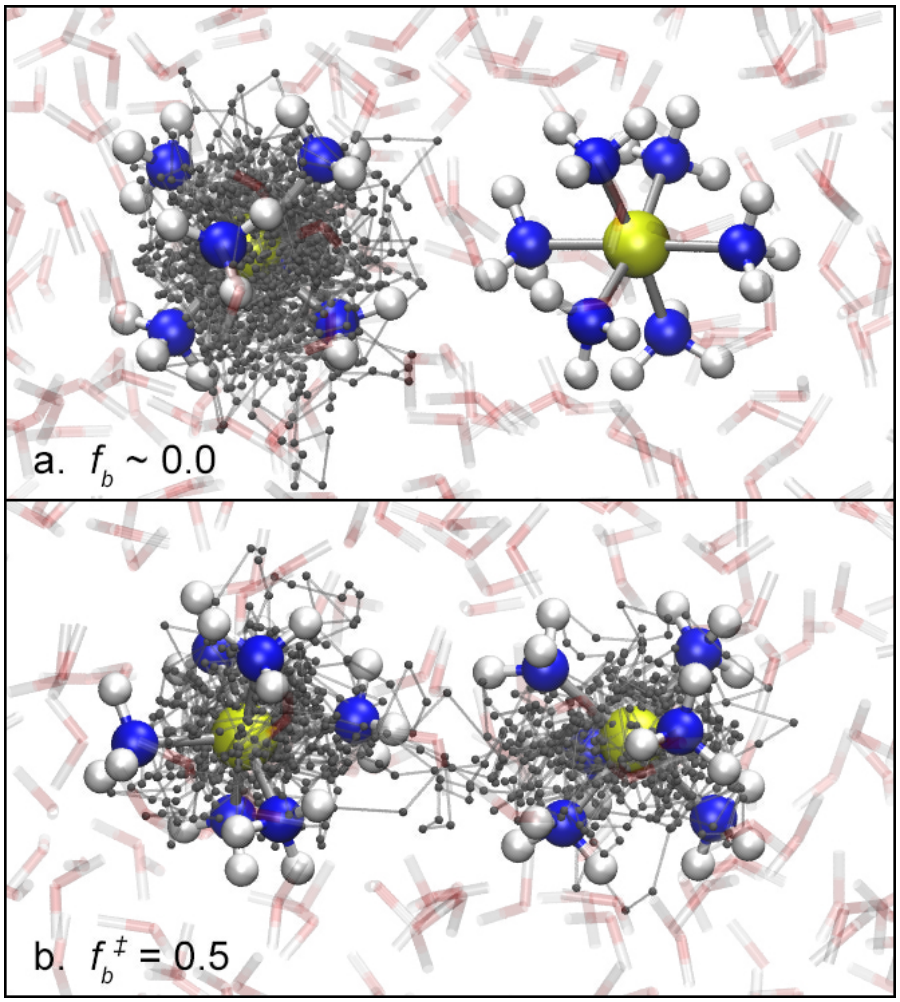

Figure 2.1: Representative snapshots [85] of the atomistic simulations in the (a.) reactant basin and (b.) "transition state" configurations of the symmetric $Co(NH_3)_6^{3+/2+}$ self-exchange reaction. The Co centers are shown in yellow, N in blue, H in white, the RP electron in gray, with red and white solvent (water) molecules (made semitransparent for clarity).

to the system in its 'reactant' state, where the RP is localized on the donor TMC ($f_b \sim 0.0$, Figure 2.1 a.), and the system at the dividing surface where the RP electron is delocalized over both TMCs ($f_b^{\ddagger} = 0.5$, Figure 2.1 b.).

The TMCs in the reactant state are both parameterized as Co^{3+}, where the reduced species Co^{2+} is represented as a Co^{3+} on which the explicit RP electron is localized. Pairwise interactions are truncated at half the length of the box

and the long-range electrostatics are treated with force-shifting to smoothly damp the potential and its force at the cutoff [86]. The canonical (NVT) ensemble is sampled at a temperature $T = 300$ K using a Nosé-Hoover thermostat with a time constant of 0.5 ps. MD simulations are performed using the DL_POLY 4.04 software package [87], modified in-house to implement both the PIMD simulations from which we obtain the free energy profile and the real-time RPMD simulations used to calculate reaction rates.

2.3.2 The interaction potential

The interaction potential for our atomistic simulations is

$$\begin{aligned} U(\mathbf{q},\mathbf{Q}) = U_{\mathrm{sol}}(\mathbf{Q}) + U_{\mathrm{TMC}}(\mathbf{Q}) + \frac{1}{n}\sum_{\alpha=1}^{n} U_{\mathrm{e-sol}}(\mathbf{q},\mathbf{Q}) \\ + \frac{1}{n}\sum_{\alpha=1}^{n} U_{\mathrm{e-TMC}}(\mathbf{q},\mathbf{Q}) + U_{\mathrm{sol-TMC}}(\mathbf{Q}), \end{aligned} \tag{2.13}$$

where, as defined previously, $\mathbf{q}$ is the set of electron RP bead positions and $\mathbf{Q}$ represent positions of the TMC and solvent atoms. Solvent-solvent interactions, $U_{\mathrm{sol}}(\mathbf{Q})$, are treated explicitly with the simple point charge (SPC) water model [88] [1]. The electron-water and electron-TMC interactions are both described as electrostatic interactions with short range cutoffs (r_{cut}) for the attractive interactions,

$$\begin{aligned} U_{\mathrm{e-sol/TMC}}(\mathbf{q},\mathbf{Q}) &= \sum_{k=1}^{N} U^{k}_{\mathrm{e-sol/TMC}}(|\mathbf{q}-\mathbf{Q}_k|) \\ U^{k}_{\mathrm{e-sol/TMC}}(|\mathbf{q}-\mathbf{Q}_k|) &= \begin{cases} -\frac{\mathrm{q}_k e}{4\pi\varepsilon_0 r^{k}_{\mathrm{cut}}}, & r_k \leq r^{k}_{\mathrm{cut}} \\ -\frac{\mathrm{q}_k e}{4\pi\varepsilon_0 r_k}, & r_k > r^{k}_{\mathrm{cut}} \end{cases} \end{aligned} \tag{2.14}$$

[1] Despite the shortcomings of the SPC water model it is sufficiently accurate to capture free energies of solvation in the complexes considered here. See, for instance,
(i) J. Åqvist and A. Warshel, *J. Mol. Biol.*, 1992, **224**, 7–14
(ii) F. Duarte, P. Bauer, A. Barrozo, B. A. Amrein, M. Purg, J. Åqvist and S. C. L. Kamerlin, *J. Phys. Chem. B*, 2014, **118**, 4351–4362

where k indexes atoms with positive partial charges, q_k and e are the charges of atom k and the electron, respectively, ε_0 is the coefficient of vacuum permittivity, $r_{\text{cut}}^{\text{Co,N}}$ is 1.1 Å, $r_{\text{cut}}^{\text{H}}$ is 1.0 Å, and r_k denotes the distance between the k^{th} atom and RP bead [13]. Standard electrostatics dictate the electron-O interactions,

$$U_{\text{e-O}}^{k}(|\mathbf{q} - \mathbf{Q}_k|) = -\frac{q_O e}{4\pi\varepsilon_0 r_k}, \tag{2.15}$$

where q_O denotes the charge on O atoms.

The intramolecular TMC potential $U_{\text{TMC}}(\mathbf{Q})$ and solvent-TMC intermolecular potential $U_{\text{sol-TMC}}(\mathbf{Q})$ are defined using parameters from the literature as well as electronic structure calculations. The Co-N bond is treated in two different ways: using a 'harmonic bond' model that employs previously used force field parameters [56] and using a 'rigid bond' model where the Co-N bond lengths are fixed at the observed "transition state" value of 2.05 Å, corresponding to $Co^{2.5+}$ [64, 73]. Mulliken analysis is used to assign partial charges to the TMC atoms from the geometry optimized structures of gas-phase density functional theory carried out with the Gaussian 09 software package [89]; the M06 hybrid functional [90] was used with the LANL2DZ [91] basis set for Co and the 6-31G(d,p) basis set [92] for N and H atoms. The optimized geometry and each analogous atom type's partial charge is included in Appendix A. Following previous work, a single point charge representation is used for the NH_3 ligand with the effective partial charge obtained by summing over the charges on the H and the N atoms [56]. The N-H bond length, Co-N-H and H-N-H bond angles are obtained from the geometry optimized structures obtained from the density functional theory calculation described above. Angle force constants are assigned based on analogous atom types in CHARMM22 [93]. All van der Waals interactions are described using CHARMM22 parameters. The complexes maintain their octahedral structure without explicit constraints on the dihedral angles and following conventional wisdom we do not

include these terms in the force field [94, 95]. All force field parameters employed in our simulation are provided in Appendix A (Table A2).

Our parameterization protocol here is relatively simple, but we believe sufficient since the outer sphere free energy due to solvent rearrangement is dictated largely by electrostatics. [48]. We note that by employing an explicit transferring electron, we ensure a net change in charge of 1 e between the two TMCs. In addition, as noted in previous work [96], the outer sphere reorganization is relatively robust with respect to the specific charge distribution in the TMCs.

2.3.3 Computing the outer sphere free energy barrier using PIMD

Umbrella sampling with PIMD trajectories was employed for the efficient and ergodic sampling of atomistic system configurations along the f_b reaction coordinate for electron transfer. The specific sampling parameters are provided in Table 2.1. For windows in the range $0.0 \leq f_b \leq 0.1$, statistics are collected for at least 16 ps (post-equilibration) sampling time, and for windows with $f_b > 0.1$, at least 56 ps (given greater inter-window 'distance' along the reaction coordinate and weaker constraints) to achieve convergence. Classical equations of motion are integrated using the Velocity Verlet algorithm [97], and rigid bond constraints are

Table 2.1: Umbrella sampling parameters

f_b range	windows[a]	k_{f_b} (kcal/mol)
$[0, 0.007]$	8	2.0×10^6
$[0.008, 0.1)$	22	2.0×10^5
$[0.1, 0.54]$	23	3.0×10^4

[a] This denotes the number of equally spaced simulation windows for the given f_b range.

implemented with the RATTLE algorithm [98]. Since the free energy, a purely statistical quantity, is independent of the mass employed, we choose a bead mass of 364.6 a.u. to allow for the use of a larger timestep (0.025 fs). We use the standard split-propagator approach to implement a multi-step time evolution that separates evolution due to external potential (the second term in Eq. 2.8) from the internal motion of the RP that is treated exactly in the normal mode representation using fast Fourier transforms [99].

2.3.4 Computing the dynamic recrossing factor using RPMD

RPMD trajectories for real-time dynamics are generated from the classical RP Hamiltonian used in the PIMD simulations (Eq. 2.7) with the fictitious mass value set to the physical mass of the electron, $m_b = m_e$ [11]. Converged values are obtained using 840 trajectories initialized from representative configurations sampled at the reaction barrier with $f_b^{\ddagger} = 0.5$. Trajectories are time-evolved using a timestep of 5×10^{-3} fs for a total time of 1 ps, sufficiently long for the RP electron to fully localize on either the donor or acceptor TMC complex, and for the flux-side correlation function to achieve a plateau.

2.3.5 Equilibrium constant for a bimolecular reaction rate

The RPMD rate calculated here corresponds to the rate of a unimolecular reaction. To obtain the bimolecular reaction rate for the cobalt hexammine self-exchange

reaction, we compute an equilibrium constant defined as

$$K = P_r e^{-\beta\omega_r}, \tag{2.16}$$

associated with the formation of the reactive precursor complex as the two hexammine complexes come together in solution. The prefactor is approximated using [96]

$$P_r = 4\pi N_A r^2 \delta r \times 10^{-27}, \tag{2.17}$$

where N_A is Avogadro's constant, r is the inter-Co distance (7.0 Å), and we use $\delta r = r/3$ as defined for systems where the transition state involves close contact between the reactants [58]. The factor of 10^{-27} accounts for unit conversion from Å^3 to liters. In Eq. 2.16, ω_r is the work required to bring the two hexammine complexes together [100],

$$\omega_r = \frac{e^2 Z_1 Z_2}{D_s r}\left[1 + r\left(\frac{8\pi e^2 \mu}{10^{27}\epsilon_s k_B T}\right)^{1/2}\right]^{-1}, \tag{2.18}$$

where e represents the elementary charge such that e^2 is 332.1 kcal Å mol^{-1}, Z_1 and Z_2 are the charges on each complex, ϵ_s is the static dielectric constant of the solvent (assumed here to be 78.2 for water), and μ is the ionic strength of the solutions, taken here to be 1.0 M consistent with the experimental values that we compare against.

2.4 Results and Discussion

Since the self-exchange reaction is symmetric with respect to electron transfer, there is no thermodynamic driving force for the reaction ($\Delta G^{\circ} = 0$). This allows us to compute only half of the free energy profile along the bead count coordinate ($0.0 \leq f_b \leq 0.5$) to find the barrier to electron transfer. In Fig. 2.2, we show the free

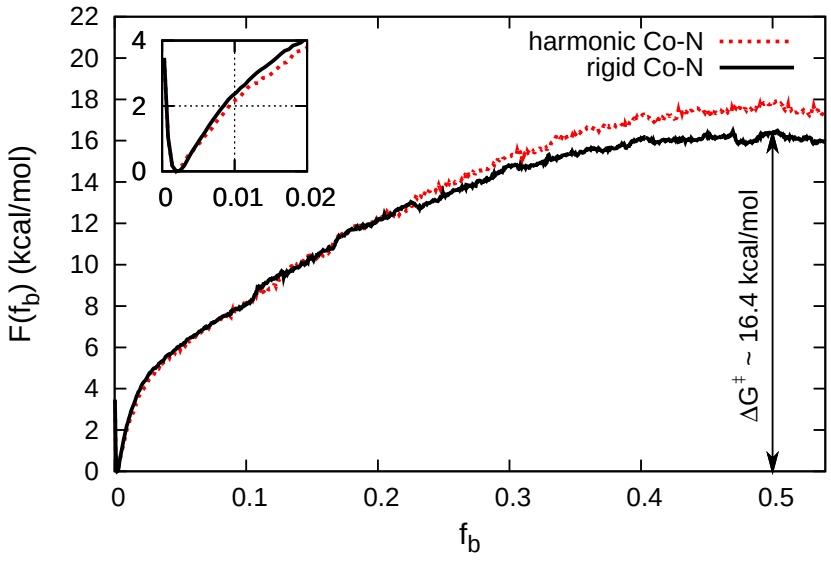

Figure 2.2: Free energy profiles of the $Co(NH_3)_6^{2+/3+}$ self-exchange reaction along f_b coordinate for a harmonic (dotted red) and rigid (solid black) Co-N bond treatment.

energy profiles for the electron transfer reaction corresponding to two cases: the harmonic bond model where the TMC Co-N bond is harmonic and parameterized for a Co^{3+} complex, and the rigid bond model where the Co-N bond length is fixed to its transition state value. In both cases, we see the expected reaction minimum at $f_b \approx 0$ (highlighted in the inset of Fig. 2.2) and the barrier maximum at $f_b = 0.5$. The harmonic bond model yields a free energy barrier of 17.9 kcal/mol, while the rigid Co-N bond model yields a value of 16.4 kcal/mol. The small difference in the barrier energies (1.5 kcal/mol) can be attributed to ligand-solvent interactions and confirms that the primary contribution to the calculated free energy barrier is outer sphere reorganization contribution. Again, we note that this is consistent with cavity models [39–42] and more recent work that employs rigorous, TMC-specific, force field parameterization schemes: the solvent rearrangement is driven largely by electronic effects rather than small structural changes in the TMC geometries [48].

We analyze solvent structure along the electron transfer reaction coordinate to

further characterize the interactions that contribute to the calculated free energy barrier. In Fig. 2.3, we show the Co-O radial distribution function, $g_{\text{Co-O}}(r)$, about the donor TMC (denoted Co^{3+} + RP) in the reactant, product, and transition states. A significant shift in the first peak of the Co-O radial distribution func-

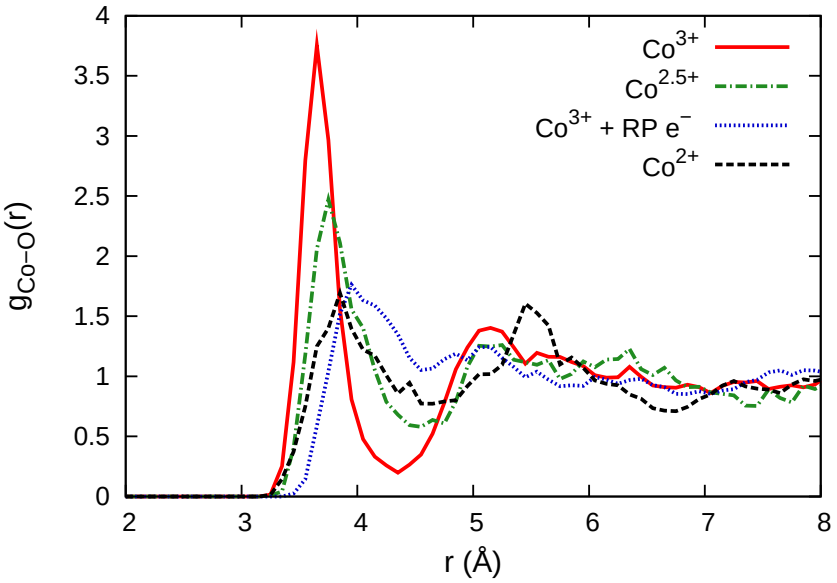

Figure 2.3: The Co-O radial distribution functions corresponding to the Co^{3+} (solid red line) is compared against the $Co^{2.5+}$ (dot-dashed green line), the *effective* Co^{2+} (dotted blue line)—a Co^{3+} with the localized RP electron, and a re-parameterized Co^{2+} (dashed black line).

tions is seen in going from the Co^{2+} species, where the RP electron is localized on the TMC, to the "transition state" species $Co^{2.5+}$, to the Co^{3+} state after the electron transfer event. This reorganization is consistent with the shift in charge accompanying the electron transfer process—electrostatic repulsion between the negatively charged RP electron and the O atoms of the water pushes the first solvent shell of Co^{2+} complex outward relative to the Co^{3+} species. We also calculate the Co-O radial distribution function using force field parameters corresponding to a Co^{2+} metal center and find that it is in reasonable agreement with the *effective* Co^{2+} of our simulation. The broadening in the first peak is consistent with the diffuse nature of the RP electron, as is the shift towards slightly greater Co-O

distances.

In Fig. 2.4 we show the distribution of the Co-N bond lengths along the electron transfer reaction coordinate in the harmonic bond model for the donor metal center in the reactant well, the transition state, and the product well. We find, in keeping with our earlier observation, a minimal change in the average Co-N bond length between the Co^{2+} and Co^{3+} oxidation states, $|\Delta r| \sim 0.04$ Å, about a fifth of the values observed experimentally [68]. In addition, we note an unphysical contraction of the Co-N bond for the Co^{2+} species relative to that of the Co^{3+} is a result of the particular partial charge assignment—there is a net positive charge on the NH_3 ligands resulting in an attractive interaction with the RP electron. Despite this, we find that the reported transition state Co-N bond length of 2.05 Å [64, 73] is successfully captured in our simulation. Our analysis of solvent and Co-N bond reorganization serves to establish that our PIMD simulation can accurately capture the solvent reorganization contribution to free energy but does not properly account for any inner sphere contribution. Moving forward, we employ the rigid bond model for both the transition state theory rate estimate and as the initial structure for our RPMD simulation.

The rigid bond model yields an outer sphere free energy barrier of 16.4 kcal/mol. This barrier is considerably larger than the 7 kcal/mol inferred from prior work that assumes the Marcus continuum model for solvent reorganization energy[55] and could be due to their implicit treatment of the solvent. It is closer to that of an inferred outer sphere contribution of about 20 kcal/mol from a previous PI-based simulation[41]; however, this particular work employed extensive re-parameterization of the force field along an assumed electron transfer reaction coordinate. Unfortunately, these values cannot be directly compared because the simulations employ

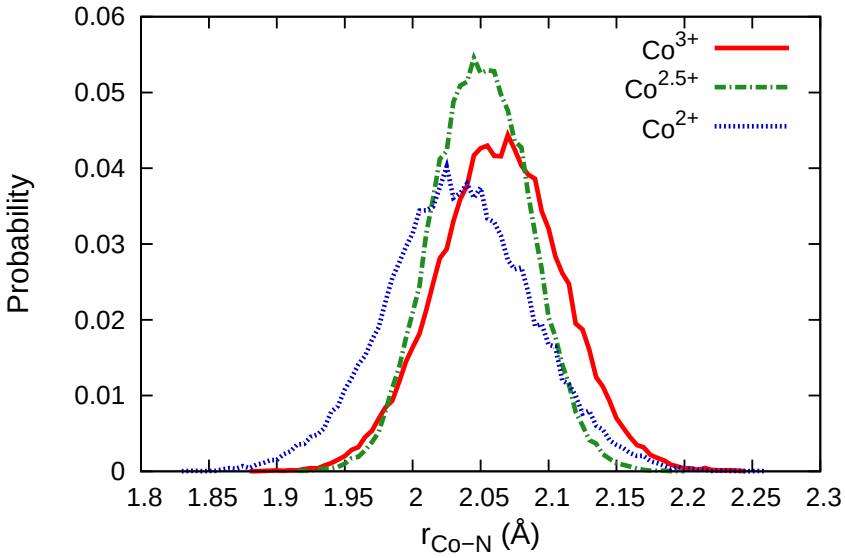

Figure 2.4: Normalized distributions of the Co-N bond length for Co^{3+} species (solid red line) compared against the $Co^{2.5+}$ (dot-dashed green line), and the Co^{2+} (dotted blue line).

different force fields and different reaction coordinates.

Using the rigid bond model parameters for the TMCs, we initialize our real-time dynamic trajectories in the RPMD framework to the barrier with the bead-count coordinate restrained to $f_b = 0.5$. The resulting RPMD flux-side correlation is shown in Fig. 2.5, and we observe the function reaches a plateau value of 0.64 in 300 fs. The relatively high value of κ at long times corresponds to reasonable amount of recrossing at the dividing surface, and is comparable to electron transmission coefficients values, 0.5 and 0.73 estimated from Landau-Zener theory [63, 64]. In addition, the ensemble of reactive trajectories from RPMD can be analyzed to extract mechanistic information about statistical and dynamic correlations. For the self-exchange reaction studied here, we calculate a solvent autocorrelation function to establish the timescale of solvent motion. In keeping with previous observations [47, 48] we find two timescales, one that matches the charge transfer reaction timescale and a second much longer relaxation time. Details are

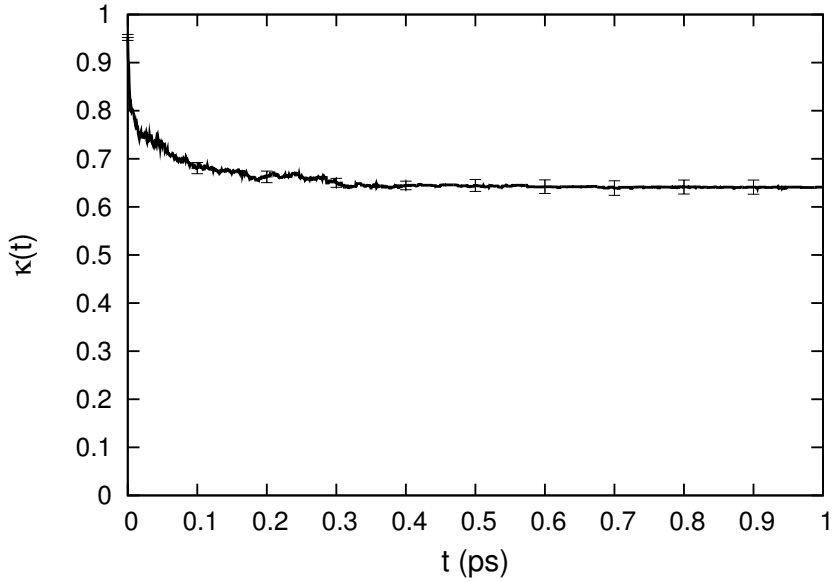

Figure 2.5: Electronic transmission coefficient for the self-exchange process.

provided in Appendix A.

The thermal electron transfer rate for the bimolecular cobalt hexammine self-exchange reaction is calculated using the expression

$$k_{\mathrm{ET}} = K k_{\mathrm{RPMD}} e^{-\beta \Delta G_{\mathrm{in}}}. \tag{2.19}$$

In Eq. 2.19, the unimolecular k_{RPMD} is defined in Eq. 2.9 and contains the transition state rate estimate for the outer sphere electron transfer reaction, $k_{\mathrm{TST}} = 1.2\ s^{-1}$, and the transmission coefficient, $\kappa = 0.64$. As described in the Computational Details section, we find a value for the equilibrium constant, $K = 0.14\ \mathrm{M}^{-1}$ necessary to obtain a bimolecular reaction rate. For the inner sphere reorganization energy, ΔG_{in}, several values based on *ab-initio* calculations have been reported in the literature [56,63,64,73,74]. To include contributions from both the Co-N bond stretch as well as the accompanying transition from the high-spin ($^4\mathrm{T}_{1g}$) to low-spin ($^2\mathrm{E}$) state of the Co^{2+} as it approaches the transition state geometry, we use a range of values between 9.69 kcal/mol and 7.78 kcal/mol as reported in multiple refer-

ences [64,73,74]. Substituting all values in Eq. 2.19, we obtain a range of values for our electron transfer rate constant from $0.09 \times 10^{-7}\,\mathrm{M}^{-1}\,\mathrm{s}^{-1}$ to $2.2 \times 10^{-7}\,\mathrm{M}^{-1}\,\mathrm{s}^{-1}$. We note that this value is obtained without any parameterization to experimental measures and is in excellent agreement with the observed rate $\geq 10^{-7}\,\mathrm{M}^{-1}\,\mathrm{s}^{-1}$ at room temperature [70, 73].

2.5 Conclusions

We introduce a general, PI-based protocol for the atomistic simulation of outer sphere electron transfer reactions in TMCs. We leverage the separation of inner and outer sphere contributions to the free energy barrier to obtain accurate estimates of outer sphere with only a single set of force field parameters. The PIMD approach employed here allows us to calculate the quantum outer sphere free energy barrier to electron transfer, taking into account electron tunneling as well as zero point energy effects. For the particular case of the cobalt hexammine self-exchange reaction, we rely on literature values for the inner sphere contribution to free energy. In applying this protocol to TMCs with extended ligand structures, we will undertake electronic structure calculations that quantify the inner sphere contributions to the barrier from geometric changes in the immediate coordination environment of the metal centers.

Reactions rates for electron transfer are computed using RPMD and are independent of any *a priori* mechanistic assumptions. However, the current implementation is limited to one-electron thermal electron transfer reactions. If necessary, multi-electron extensions to RPMD have been developed [101–104] and can be used for the direct dynamic simulation of electron transfer. We find that the simple force

field parameterization required for our protocol combined with quantization of an explicit, transferring electron yields important mechanistic insights and can be use to calculate accurate reaction rate constants. We believe this protocol will be useful for a wide range of applications including the rational design of TMCs for use in dye-sensitized solar cells.

CHAPTER 3

PATH INTEGRAL MOLECULAR DYNAMICS SIMULATIONS WITH DL_POLY

3.1 An Overview of our Utilization of DL_POLY

The path integral (PI)-based approach employed above to simulate an explicit electron transfer in complex, condensed-phase systems exploits the classical isomorphism of a PI to introduce relevant quantum effects. Specifically, we treat all the atoms of the system by conventional molecular dynamics means, and allow them to interact by electrostatics with a single, explicit transferring path integral, or "ring polymer" (RP), electron. This way, we are able to mimic the quantum effects of primary importance here, namely tunneling and zero point energy of the electron, while maintaining desirable scalability. We mention this here merely to offer the reader some context, however, the focus of this chapter is on the implementation details concerning how to incorporate the path integral electron and modify the DL_POLY source code to account for its interactions with the surrounding, conventionally treated environment (here, solvent and transition metal complex atoms).

We begin with a brief introduction to the general workflow associated with running molecular dynamics (MD) simulations using the DL_POLY_4.04 program[1],

[1]In keeping with the conventions followed by the DL_POLY manual [105], we use the following text styles to indicate specific meanings:

1. FILENAME is used for filenames,
2. SUBROUTINE is used for programs, subroutines, and functions,
3. **keyword** is used for keywords and program directives, and
4. `variable` is used for named variables and parameters.

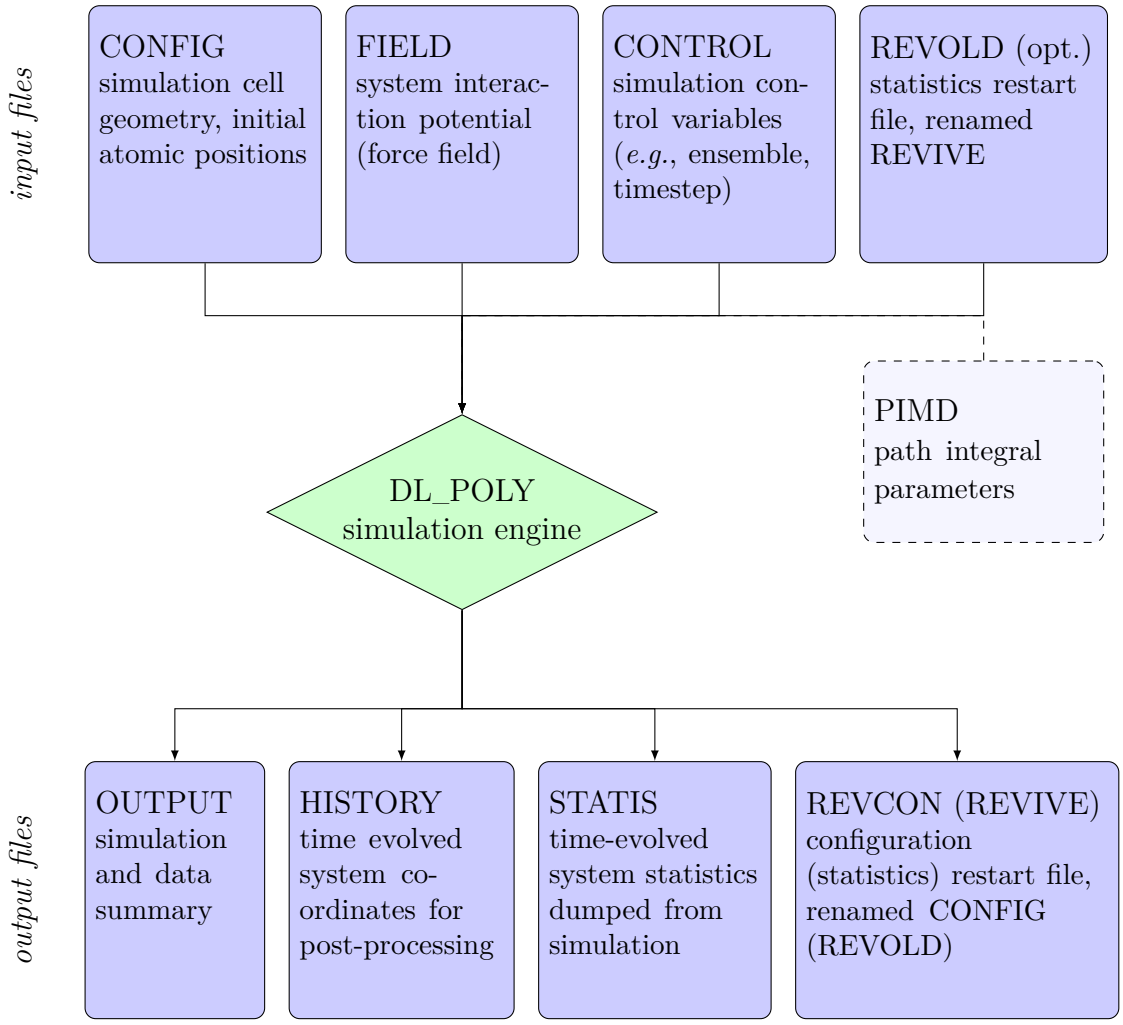

Figure 3.1: A flow chart outlining the primary input files provided by the user to, and output files reported by, the DL_POLY simulation engine. Solid-lined rectangles represent the conventional input and output files, the dashed rectangle represents an additional input file required for introducing a path integral into the simulation, and the diamond represents the program's simulation engine.

though one should refer to the user manual [105] for a more in-depth description of the software and a complete listing of its various functionalities.

Fig. 3.1 outlines the primary input and output files required to run a simulation with DL_POLY. At the very least, the user must provide the CONFIG, FIELD, and CONTROL files for the simulation engine to proceed. The CONFIG file

provides DL_POLY with all of the simulation initial conditions, which must include at least the atom positions, but optionally their velocities and forces, as well, in addition to the simulation unit cell geometry. The force field parameterization scheme that defines all atomic interactions is provided in the FIELD file. The CONTROL file provides the program with the simulation control variables for run time. If the continuation of a simulation is requested by the user, they should also provide the system statistics from a previous run, renaming the REVIVE file REVOLD. To execute a path integral-based simulation, an additional file, PIMD, is also required. This file provides the total number of beads there are in the RP, as well as how many steps the RP beads should take for each step of the remaining, conventionally treated atoms.

Following the simulation, DL_POLY will always provide the user with the OUTPUT file which includes a summary of the simulation input specifications, the initial run time configuration, statistical information from the simulation, as well as structural data of the final configuration. The HISTORY file is where DL_POLY dumps system coordinates (and velocities and forces, if requested) at a given frequency throughout the simulation. This file is convenient for post-processing purposes. The STATIS file contains statistical information such as the system temperature, individual components of the system intra- and inter-molecular interaction energies and virials, and is also dumped by DL_POLY at a set frequency throughout the run. The REVCON and REVIVE files are intended to serve as a restarting system configuration and statistics files to be renamed CONFIG and REVOLD by the user, respectively. For a more extensive list and description of the many possible input and output files, we refer the reader to the DL_POLY manual [105].

To set the stage for the descriptions of the code modifications described below, we now briefly summarize the steps DL_POLY takes during a simulation run. For the sake of simplicity, we will assume the simulation is a single processor production run of an (already equilibrated) NVT ensemble of atoms time evolved using the Velocity Verlet (VV) integrator [97] and a Nosé-Hoover themostat. Then, we will point out where these modifications fit into the main simulation for the case where the user includes a quantum particle described according to the path integral formalism which interacts with its classically treated environment only by electrostatics.

After declaring and defining all of the necessary modules and variables, communications, clocking, and output files are initialized by the main DL_POLY program. Essential program arrays (configuration, interaction, statistics, *etc.*) are allocated after the subroutine READ_CONFIG reads in the CONFIG input file. Then, the CONTROL and FIELD files are read, from which DL_POLY interprets the user-defined simulation run specifications, and force field parameterization scheme, respectively. When a restarting job, the REVOLD input file is also read, and then the initial system temperature is set, and the forces and velocities of any frozen atoms are quenched *via* the FREEZE_ATOMS subroutine. Then, initialization of the variables necessary for describing the different components of the kinetic stress and energy components, as well as their accumulators, for all of the different interactions defined within the system takes place. Finally, the MD subroutine specific to the VV algorithm is called; for this example, MD_VV.

Within MD_VV, the system is time evolved by integrating Newton's equations of motion according to the VV algorithm [97], calling the VV subroutine specific to the ensemble chosen step by step until the counter indicates that the final timestep

has been reached.[2] Here, the NVT_H0_VV subroutine is called, and the atomic positions $\mathbf{Q}$, velocities $\mathbf{V}$, and forces $\mathbf{F}(\mathbf{Q}(\mathbf{t})) = -\frac{\partial \mathbf{U}(\mathbf{Q}(\mathbf{t}))}{\partial \mathbf{Q}}$, (where $U(\mathbf{Q})$ is the defined interaction potential) are read in from an array within the CONFIG_MODULE. The VV scheme is carried out in the following steps:

1. First, the velocities are advanced a half time step (Δt) by integration of the force,
$$\mathbf{V}(t + \frac{1}{2}\Delta t) \leftarrow \mathbf{V}(t) - \frac{\Delta t}{2m}\frac{\partial U(\mathbf{Q}(t))}{\partial \mathbf{Q}}.$$

2. Then, these new velocities are used to update the positions a whole step,
$$\mathbf{Q}(t + \Delta t) \leftarrow \mathbf{Q}(t) + \Delta t\, \mathbf{V}(t + \frac{1}{2}\Delta t).$$

3. In accord with the force field, the forces are updated using the new atomic positions,
$$\frac{\partial U(\mathbf{Q}(t + \Delta t))}{\partial \mathbf{Q}} \leftarrow \frac{\partial U(\mathbf{Q}(t))}{\partial \mathbf{Q}}.$$

4. Lastly, the velocities are updated an additional half step according to these updated forces,
$$\mathbf{V}(t + \Delta t) \leftarrow \mathbf{V}(t + \frac{1}{2}\Delta t) - \frac{\Delta t}{2m}\frac{\partial U(\mathbf{Q}(t + \Delta t))}{\partial \mathbf{Q}}.$$

[2] An aside: previously, when the main program read the input files, it took note of which ensemble was requested, each of which is associated with a particular identification number. In this stage of the simulation, it uses this number to search (by a sequence of IF statements) through all possible available ensembles, until the associated subroutine, here NVT_H0_VV, is located.

This is a common technique throughout the DL_POLY source. Many of the **directives** provided by the user in the input files belongs to a family of related **directives** (here, the available ensembles, but other examples include the functional forms of different bonding or vdW interactions). Within each of these "families", each of the different options has an associated number, and this value is what serves as its identifier to the DL_POLY source. When we are interested in adding alternative functional forms to the available interaction potentials, for example, we will introduce a new identifier which then connects the (usually) more intuitive abbreviated name that the user will provide in the input files, with the functional form we define within the code.

The NVT_H0_VV subroutine updates the forces in the third step by calling on a variety of other subroutines, each of which is responsible for updating the atomic forces with respect to the different types of interactions defined as part of the force field in the FIELD input file. This includes two-body interactions like vdW and electrostatics, bonds, angles, and any applied external field, for example. As discussed in more detail below, this time evolution scheme is modified for PI-based simulations to lift the need for an extremely small time step and accelerate sampling efforts.

For thermostatting purposes, the Nosé-Hoover-flavored VV algorithm varies slightly from the conventional VV stages. For this thermostat specifically, the equation of motion for velocity is modified to incorporate a friction coefficient that is updated in accord with the target system kinetic energy and a user defined time constant. The friction coefficient is time evolved a quarter time step, the velocity updated, and then time evolved an additional quarter time step, both before and then after, sandwiching the standard VV scheme described above. The program then returns to the MD_VV subroutine where physical quantities of the system are calculated (energies, virials, *etc.*) and statistics are collected. The output files are then updated, and the main DL_POLY program is revisited, where the output files are then finalized and the job is terminated. As described in detail below, the primary changes to the source code involve adding additional functional forms to the interaction potentials, and modifying the VV algorithm for the RP beads.

3.2 Modifications to the DL_POLY Source Code

Below, we provide a general overview of how we incorporate PI theory into the code described above. The intent is to familiarize both those interested in utilizing the current implementation as well as anyone interested in a modified, improved, or alternative version of it. We recall the physical picture of the RP Hamiltonian introduced in Chapter 1 and use this context describe the modifications that were made to the DL_POLY source code for running sampling "trajectories" with the VV integrator. Pieces of the source code are included as Appendix B to serve as guidance to the reader. However, for the sake of brevity, only those that are modified from the original DL_POLY code are explicitly presented. Lastly, potential sources of improvement to the current approach are discussed, with a more general and robust implementation strategy in mind.

The RP is included as the last n atoms of the simulation input files, such that when the simulation is running for a system of $(n + N)$ total atoms, the last n RP bead "atoms" make up the RP "molecule"; these "atoms" are treated differently than the N conventionally treated classical atoms of the system (solvent, transition metal complexes, *etc.*). A slight modification to config_module.f90 in the DL_POLY source code is made which defines the variable for the total number of n RP beads (treated here as atoms which make up this "molecule") which is read in from an additional required input file named PIMD by the READ_FIELD.F90 DL_POLY subroutine.

This discussion is broken down by the different terms of the system Hamiltonian,

$$H_n = \sum_{j=1}^{N} \frac{1}{2} M_j \mathbf{V}_j^2 + \sum_{\alpha=1}^{n} \frac{1}{2} m_b \mathbf{v}_\alpha^2 + \frac{1}{n} \sum_{\alpha=1}^{n} \frac{1}{2} m_e \omega_n^2 (\mathbf{q}_\alpha - \mathbf{q}_{\alpha-1})^2 + U(\mathbf{q}, \mathbf{Q}), \quad (3.1)$$

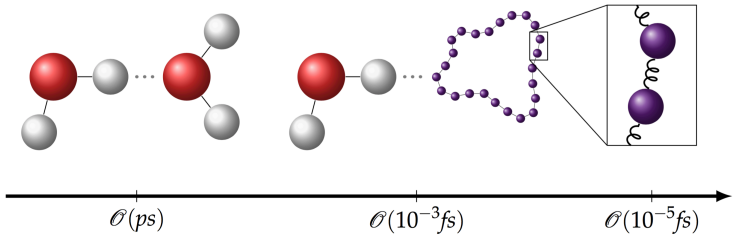

Figure 3.2: PI-based simulations encompass a wide range of timescales, ranging from on the order of ps with standard intermolecular interactions (left) to fast intramolecular 10^{-5} fs vibrations (right).

where M and m represent the masses, $\mathbf{V}$ and $\mathbf{v}$ the velocities, and $\mathbf{Q}$ and $\mathbf{q}$ the positions of the classical atoms and RP beads, respectively. We recall that the first and second terms represent the kinetic energy of the classical atoms and the RP electron (considered here a RP "molecule" made up of n beads), respectively. The third term represents the harmonic interactions, or "springs", between neighboring beads where $\mathbf{q}_0 \equiv \mathbf{q}_n$. The last term encompasses the full system interaction potential, including atom-atom, atom-bead, and bead-bead interactions. As discussed in further detail below, the bead mass m_b associated with the kinetic energy term in Eqn. 3.1 above is arbitrary and chosen to facilitate statistical sampling, unlike the physical mass m_e present in the bead-bead harmonic interaction term. However, if these simulations are used to describe system dynamics, the bead mass must be equivalent to the physical mass of the particle.

3.2.1 Mixed time scales and efficient system evolution

As mentioned previously, disparate timescales are characteristic of charge transfer in complex chemical systems. Figure 3.2 emphasizes the large span of timescales described by the RP Hamiltonian. Using examples of interactions between a RP and a conventionally (classical MD) simulated water molecule. On one end, the

fast "intramolecular" RP interactions take place on the order of 10^{-5} fs, where as interactions between water molecules generally call for a simulation timestep in accord with ps-scale motions. The careful reader may notice a difference in denotation of the RP electron bead mass between the second and third terms of Eqn. 3.1. We point out that the kinetic contribution of the RP is introduced to facilitate the phase space statistical sampling by molecular dynamics simulations rendering the "bead mass" (m_b) an arbitrary choice; it is therefore chosen to help alleviate this timescale discrepancy. However, though technically arbitrary, practical considerations should be made. Described below, one can efficiently and exactly evolve the RP with respect its intramolecular interactions such that these interactions will not call for an prohibitive timestep. However, the external forces on the RP beads with the physical electron mass may still be limiting and is thus overcome by using a larger mass for m_b. An optimal choice should not be so large that the RP is significantly slowed down to the point of inhibiting timely, ergodic sampling, but should be sufficiently large (nearer that of the lighter classical atoms in the simulation) to avoid limiting the simulation timestep.

The kinetic energy and bead-bead harmonic terms of Eqn. 3.1 are dealt with, in part, in the NVE_0_VV.F90 or NVT_H0_VV.F90 subroutines of the DL_POLY source code. As the changes in each of these codes are similar, only those snippets of the NVE code are included in Appendix B for demonstrative purposes. Newton's equations of motion are solved for the first N atoms using the standard VV integration approach. As was mentioned previously, given the relatively small mass of the RP beads, there is a rather large disparity of timescales at play and their conventional time evolution is inefficient and undesirable. Instead, as is standard for the implementation of PI-based approaches, a symplectic integration scheme is adopted whereby the system evolves according to a symmetric split

propagator [99],

$$e^{-\Delta t L} \simeq e^{-(\Delta t/2)L_U} e^{-\Delta t L_0} e^{-(\Delta t/2)L_U}. \tag{3.2}$$

L_0 is the Liouvillian associated with the free RP Hamiltonian (the second and third terms of Eqn. 3.1) and L_U that of the external potential (last term of Eqn. 3.1). In this way, by transforming to a normal mode representation and exploiting fast Fourier transforms (FFTs) to time evolve what is effectively a ring of coupled harmonic oscillators, the RP bead positions and momenta can be evolved exactly with respect to the free RP Hamiltonian. This time evolution scheme is incorporated into the NVE_0_VV subroutine, and summarized in the following steps [99]:

1. Half step the beads' momenta (here, $\mathbf{p}_\alpha = m_b \mathbf{v}_\alpha$) under the influence of the external potential $U(\mathbf{q}, \mathbf{Q})$,

$$\mathbf{p}_\alpha(t + \frac{1}{2}\Delta t) \leftarrow \mathbf{p}_\alpha(t) - \frac{\Delta t}{2} \frac{\partial U((\mathbf{q}, \mathbf{Q}))}{\partial \mathbf{q}_\alpha}.$$

2. Transform both the position and momenta from the bead representations to the normal mode representation (done using FFTs), where $C_{\alpha\mu}$ is the orthogonal transformation matrix [99] for even n,

$$\tilde{\mathbf{p}}_\mu \leftarrow \sum_{\alpha=1}^{n} \mathbf{p}_\alpha C_{\alpha\mu} \text{ and } \tilde{\mathbf{q}}_\mu \leftarrow \sum_{\alpha=1}^{n} \mathbf{q}_\alpha C_{\alpha\mu}.$$

3. Full step the beads position and momenta under the free RP Hamiltonian,

$$\begin{pmatrix} \tilde{\mathbf{p}}_\mu(t + \Delta t) \\ \tilde{\mathbf{q}}_\mu(t + \Delta t) \end{pmatrix} \leftarrow \begin{pmatrix} \cos(\omega_\mu \Delta t) & -m_e \omega_\mu \sin(\omega_\mu \Delta t) \\ (m_e \omega_\mu)^{-1} \sin(\omega_\mu \Delta t) & \cos(\omega_\mu \Delta t) \end{pmatrix} \begin{pmatrix} \tilde{\mathbf{p}}_\mu(t) \\ \tilde{\mathbf{q}}_\mu(t) \end{pmatrix},$$

   where $\omega_\mu = 2\omega_n \sin(\mu\pi/n)$.

4. Transform back from the normal mode representations to the bead representation,

$$\mathbf{p}_\alpha \leftarrow \sum_{\mu=0}^{n-1} C_{\alpha\mu} \tilde{\mathbf{p}}_\mu \text{ and } \mathbf{q}_\alpha \leftarrow \sum_{\mu=0}^{n-1} C_{\alpha\mu} \tilde{\mathbf{q}}_\mu.$$

5. Update the forces using the new atomic positions,

$$\frac{\partial U(\mathbf{q}, \mathbf{Q}; t + \Delta t)}{\partial \mathbf{q}_\alpha} \leftarrow \frac{\partial U(\mathbf{q}, \mathbf{Q}; t)}{\partial \mathbf{q}_\alpha}.$$

6. Half step the beads' momenta using updated the forces,

$$\mathbf{p}_\alpha(t + \Delta t) \leftarrow \mathbf{p}_\alpha(t + \frac{1}{2}\Delta t) - \frac{\Delta t}{2}\frac{\partial U(\mathbf{q}_\alpha, \mathbf{Q}_1, ..., \mathbf{Q}_N)}{\partial \mathbf{q}_\alpha}.$$

Here, the transformations to and from the normal mode representation (steps 2 and 4 above) are achieved with the FFTW3 [106] package. This scheme is similar to the previously described VV scheme, except now, the bead momenta are updated according to the external forces, and forces due to the spring terms separately. Specific pieces of the code that execute this mixed time evolution scheme are included as part of Appendix B.1.

Staying true to the PI Hamiltonian

While exploiting FFTs enables the efficient time evolution of the RP-containing system, treating the bead-bead harmonic interactions exactly, the energy contributions associated with this term of the Hamiltonian must also be incorporated into the full system energy of the simulation. Moreover, the default mode for DL_POLY is to include electrostatic interactions between all atoms not directly bonded to one another. However, this is not representative of the RP Hamiltonian, and so a new harmonic "bond" functional is defined, called with **bdbd** within DL_POLY whose purpose is twofold: it enables us to add the bead-bead interaction energy to the full system energy, and by defining null bead-bead interactions between all *non-neighboring* RP beads (using a force constant of zero), bead-bead electrostatics are excluded and a simulation true to the full system Hamiltonian

described above is ensured. This modification, provided in Appendix B.2, is made to BONDS_FORCES.F90.

3.2.2 Short-ranged electrostatic cutoffs

Treating the attractive electrostatic interactions between the (negatively) charged RP beads and the surrounding (positively) charged environment calls for additional modifications to be made to the DL_POLY source code. Because electrostatics are the only mode by which the RP electron interacts with the surroundings, we impose a short range cutoff to ensure the relatively light RP electron beads do not become coulombically bound to oppositely charged atom(s). Because DL_POLY includes these electrostatics *without* the cutoff by default, to avoid double counting the electrostatics, we simply correct for those interactions that occur within the cutoff distance; here, we have called the correction for the short range cutoffs a van der Waals interaction **crlk**, treated within VDW_FORCES.F90. The relevant code is provided in Appendix B.3. *Note:* This implementation assumes a direct treatment of the vdW interactions; that is, DL_POLY must calculate directly, instead of interpolating from a spline, the vdW interactions (for reasons mentioned below). The user must ensure they are signalling DL_POLY to do this with the keywords **vdw direct** within the CONTROL input file. Additionally, the specific correction made in the code (shown above) assumes a force-shifted treatment of the electrostatic interactions at the long range cutoff, also set within the CONTROL file, using the keyword **shift**.

3.2.3 Efficient bead count coordinate sampling

Lastly, we touch on incorporating the umbrella sampling constraints, in this case, harmonic biasing potentials, to facilitate the statistical sampling of energetically unfavorable configurations. Because these processes generally take place in high energy regions of the free energy surface, running unbiased sampling simulations to the extent necessary to capture a statistically significant number of them is generally not feasible. Instead, by introducing artificial biases on the system, we can more efficiently accomplish ergodic sampling along the progress of these processes using relatively short sampling runs to extract the free energy barrier relevant to the reaction of interest.

With these constraints, one can "umbrella sample" [83] efficiently and ergodically along the reaction coordinate to determine the free energy barrier to the reaction of interest. The example collective coordinate included here is the RP "bead count" variable:

$$f_b(z_1, ..., z_n) = \frac{1}{n} \sum_{\alpha=1}^{n} \frac{1}{2} \left(\tanh(b z_\alpha) + 1 \right). \tag{3.3}$$

As the reaction coordinates of interest here are collective variables—that is, dependent on the collective positions of a given type of atoms (here, those of the RP electron)—the constraints along them fit most naturally when defined within DL_POLY as a form of van der Waals interaction (instead of a pairwise bond functional). In this implementation, the bead count constraint is called between the *bd* and an otherwise interaction-less *ghost* atom types in the vdW list of the FIELD input file. Additionally, given the dependence on many interatomic distances, direct evaluation of this term is performed by averaging over the RP beads within the DL_POLY subroutine VDW_FORCES.F90. The code modifications made are

provided in Appendix B.4. For similar purposes, constraints for the RP center of mass and collective solvent reaction coordinates are available with directives **bdus** and **csc**, respectively. When considering alternative reaction coordinates, the associated long range force-shifted corrections should be included as a part of VDW_DIRECT_FS_GENERATE.F90 code, if necessary.

3.3 Suggested Improvements to this Implementation Approach

While there certainly exist more general and robust ways to accomplish incorporating path integral-based simulation abilities into DL_POLY, this was not the primary objective of the efforts outlined above. Below, we list some suggested improvements toward a more user-friendly implementation:

- modify the PIMD input file to include
    1. the physical and/or fictitious masses of the RP beads
    2. a flag which indicates whether a statistical or dynamical PI-based run is to be performed
    3. the spring term describing bead-bead interactions
    4. an indicator that tells DL_POLY to assume direct evaluation of the vdW interactions (or an alternative approach to adding collective coordinates used for umbrella sampling purposes)
- incorporate the RP in a way that is independent of the order of molecules provided to DL_POLY in the input files, instead of ensuring it is always the last N-beads indexed

- modify the treatment of either form of coulombic interaction being called to automatically correct for any short range cutoffs being imposed
- negate unwanted bead-bead electrostatic interactions *via* an exclusion list, instead of defining null interactions between non-neighboring beads in the FIELD file

Moreover, the implementation detailed above is limited to a system of conventionally simulated classical atoms and the addition of a single explicit electron. In theory, the PI-based theory has potential to be extended to systems with multiple (interacting) explicit electrons in the system but not, however, without significant modifications—the implementation here may only act as a guide to how one might begin thinking about incorporating this idea for multi-electronic state systems.

CHAPTER 4

SIMULATING ELECTRON TRANSFER IN TRANSITION METAL COMPLEX SYSTEMS: FUTURE DIRECTIONS

Dye-sensitized solar cells (DSCs) are a lower cost solution to converting sunlight to electricity than traditional silicon cells. In recent years, transition metal complexes (TMCs) have played an increasingly prominent role in liquid electrolyte DSCs [19–22]. Whereas traditional DSCs employed an iodide/triiodide electrolyte solution, TMC-based electrolytes have been of great interest lately due to their tunable molecular nature which can be optimized to overcome the shortcomings of the traditional redox shuttle like its high dye regeneration overpotential and competitive light absorption [19,107]. However, the introduction of new redox shuttles calls for reoptimizing the entire system. In Figure 4.1 we show a schematic diagram of the working principles of a DSC to highlight the complexity of the system kinetics at play and really underscore the need for theoretical approaches capable of studying each of these steps and their interdependence. The ideal pathway involves the excitation of the sensitizing dye by incident sunlight (k_1), the injection of an electron from the dye to a semiconductor coating on one electrode (k_2), and then the regeneration of the dye by a redox shuttle (k_3) followed by its reduction at the counter electrode (k_4). Competing pathways include the recombination of an electron from the semiconductor surface to the either the oxidized dye (k_5) or redox shuttle molecules (k_6). The energy level alignment of the different components of the system, and in particular the injection potential (ΔG_{inj}) and regeneration potential (ΔG_{reg}), play a large role in dictating the efficiency of these systems and clearly will depend on their chemical makeup.

We are interested in using the explicit electron path integral (eePI)-based ap-

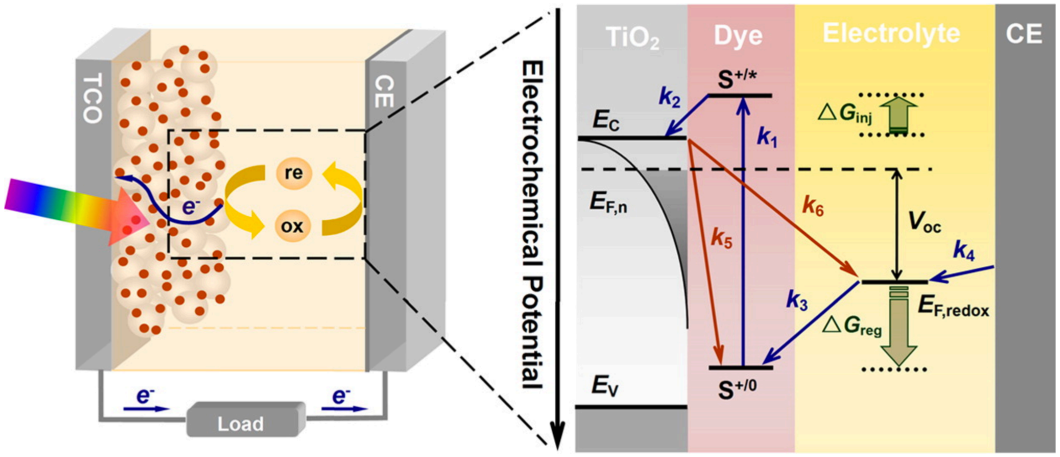

Figure 4.1: Schematic representation of the operating principles of a liquid electrolyte DSC showing the various electron transfer pathways (k, described in the text) and relevant energy level offsets (ΔG). Reprinted with permission from Zhe Sun, Mao Liang, and Jun Chen. Kinetics of iodine-free redox shuttles in dye-sensitized solar cells: Interfacial recombination and dye regeneration. *Accounts of Chemical Research*, 48(6):1541–1550, 2015. Copyright 2015 American Chemical Society.

proach described in Chapter 2 above to study the electron transfer kinetics for different combinations of redox shuttles and dye molecules. In particular, we would like to look at these processes in systems relevant to DSCs, like the regeneration of a zinc porphyrin-based dye by a cobalt-based redox shuttle [21]. However, though initially motivated by these systems, the above eePI study only begins to assess the appropriateness of using this particular PI-based protocol to describe bimolecular electron transfer involving TMCs. When considering the extension of this approach to a more general set of TMCs and systems of increasing complexity, several questions of more fundamental interest remain:

1. Are we able to accurately capture the distance dependence of the rate of electron transfer in TMC systems with this approach? And if so, could we use these studies to distinguish between statistical and dynamical contributions

to these trends for ligands of varying chemical nature, or solvents of different polarity?

2. Do these simulations, even when parameterized to an intermediate, "transition state" model, maintain predictive power for less symmetric electron transfer reactions? Or is it possible to get decent estimates of cross-exchange rates from simulating sets of (symmetric) self-exchange processes?

3. How strongly does the particular partial charge scheme or solvent model used influence the free energy barrier extracted with this method? Are any discrepancies dampened with increasing complexity of the TMCs?

Answers to questions like these will inform, and ultimately shape, the utilization of eePI simulations for describing these phenomena. In this chapter, we propose some next steps toward addressing them. After introducing the model system motivated by DSCs, we begin with a brief overview of electron transfer rate theory. Then, we revisit each of the questions from above and, using the proposed model system, offer some next steps geared towards addressing them.

4.1 Introducing the New Model System

To provide a reference point for the discussion below, we briefly mention here the system that we have taken the initial steps toward modeling. Though quite a bit more complex than the cobalt(III/II) hexammine system studied above, we have chosen a Zn-based porphyrin known as SM371 [21], and the more routinely used tris(2,2'-bipyridine)cobalt(III/II) redox shuttle, referred to herein as Co(bpy) [107]. Not only will this case serve as a somewhat extreme test of the eePI protocol, but, this could also be the beginning steps of the extension of the eePI approach to

a DSC system. Moreover, there are literature values associated with these (or similar) molecules' inner sphere reorganization energies, which will be useful when determining the rate [34, 108].

4.2 A Brief Recollection of Electron Transfer Theory

The theory of bimolecular electron transfer is well-established, and we take advantage of this here to explore the boundaries of the eePI approach, referring the reader to the literature for more in-depth reviews of the theory [58, 109, 110]. In Marcus' solvent polarization model [110, 111], as refined by Libby [112], electron transfer can be described generally as a rare event event in which thermal fluctuations of the system environment serendipitously result in the formation of an "activated complex" at the point of degeneracy between the reactant and product states. The electronic transition can take place at this point, free of any energetic cost, after which the environment would adapt to the new charge distribution.

With the eePI approach, we use classical molecular dynamics to describe all but the electron, which we represent as a 1024-bead RP to account for the effects of quantum tunneling and zero point energy. In Chapter 2, we express the rate of electron transfer consistent with the Ring Polymer Molecular Dynamics (RPMD) formalism (k_{RPMD}, Eqn. 2.9), as a contribution from two independently computed terms: a statistical term, k_{TST} (Eqn. 2.10), the transition state theory rate constant, and a dynamical term, $\kappa(t)$ (Eqn. 2.11), whose infinite time limit describes the probability of the system recrossing the dividing surface after having reached the product state. While this rate formulation is independent of the choice of dividing surface [11], one should be careful when comparing these individual terms to

alternative forms (below), to maintain consistency by restricting their comparison to situations where the conventional transition state description is used.

In general, the rate constant of electron transfer can be written as

$$k_{\mathrm{ET}} = \kappa_{\mathrm{el}} \nu_{\mathrm{n}} k_{\mathrm{n}} \tag{4.1}$$

when nuclear tunneling effects are neglected [29]. Again, κ_{el} is the electronic transmission coefficient which, though it bears the same physical significance, it is denoted differently here to distinguish it from that which is evaluated by the RPMD approach. ν_{n} is an effective vibrational frequency of the activated complex, and k_{n} is a nuclear factor which accounts for the energy barrier associated with the configurational reorganization of the system.

In the context of this chapter, one particularly notable feature of our evaluation of k_{RPMD} *via* the eePI approach is its applicability to both adiabatic and nonadiabatic reactions. On the other hand, the functional form of the factor of $\kappa_{\mathrm{el}}\nu_{\mathrm{n}}$ in Eqn. 4.1 depends on whether the process is nonadiabatic ($\kappa_{\mathrm{el}} << 1$), where there is minimal electronic coupling between the reactants, or adiabatic ($\kappa_{\mathrm{el}} \sim 1$), when this coupling is strong. In the nonadiabatic case, the rate constant of electron transfer between reactants at a distance r apart is

$$k_{\mathrm{naET}} = \frac{H_0^2}{\hbar} \left(\frac{\pi}{\lambda k_{\mathrm{B}} T} \right)^{1/2} e^{-\sigma(r-r_0)} e^{-\frac{(\lambda+\Delta G^0)^2}{4\lambda k_{\mathrm{B}} T}}, \tag{4.2}$$

where H_0 is the the electronic coupling matrix element at the close-contact separation r_0 of the reactants. λ is the total reorganization energy—the total energy required to push the system into the nuclear configuration of the products without the electronic transition having taken place—which, as we recall from Chapter 2, consists of an inner contribution (λ_{in}) associated with intramolecular changes (bond distances, angles, *etc.*), and an outer contribution (λ_{out}) associated with reorganization of the surrounding environment. The rate of decrease of the electronic

coupling with separation distance r is denoted by σ, and ΔG_0 is the Gibbs free energy change of the reaction. In the case of adiabatic electron transfer, given the strong coupling between the reactants, the electronic transition is generally much faster than the surrounding nuclear modes ($\kappa_{\mathrm{el}} \sim 1$) and the rate at separation distance r is expressed as

$$k_{\mathrm{adET}} = \nu_{\mathrm{n}} e^{-\sigma(r-r_0)} e^{-\frac{(\lambda+\Delta G^0)^2}{4\lambda k_{\mathrm{B}} T}}. \tag{4.3}$$

A notable distinction between the eePI approach to determining the rate and the rate expressions described here is the definition of the reaction coordinate along which the free energy differences are determined.

4.3 Exploring the Distance-dependence on the Electron Transfer Rates Predicted using the eePI Approach

Are we able to accurately capture the distance dependence of the rate of electron transfer [113] in TMC systems with this approach? And if so, could we use these studies to distinguish between statistical and dynamical contributions to these trends for ligands of varying chemical nature, or solvents of different polarity?

The fact that the RPMD rate k_{RPMD} is determined by evaluating the free energy barrier separate from the dynamical correction κ_{el} is particularly well suited to study reactant separation distance-dependences . The first exponential term (that with explicit distance-dependence) of both of the rate equations above can be grouped in with the remainder of the dynamical terms that precede it and compared to the trends observed for the infinite time limit of $\kappa(t)$ using RPMD at different reactant separation distances. As is shown below, the distance dependence

of this term may also arise from its influence on the reorganization energy (see Eqn. 4.4 below). The remaining term, $k_{\mathrm{n}} = \exp\left[-\frac{(\lambda+\Delta G^0)^2}{4\lambda k_{\mathrm{B}}T}\right]$, only exhibits the distance dependence inherent in λ, and generally only in the contribution from λ_{out} [113] which can be approximated as

$$\lambda_{\mathrm{out}} = \frac{e^2}{4\pi\epsilon_0}\left(\frac{1}{2r_1}+\frac{1}{2r_2}-\frac{1}{r}\right)\left(\frac{1}{\epsilon_{\mathrm{op}}}-\frac{1}{\epsilon_s}\right) \tag{4.4}$$

by assuming a transfer of charge e between two spheres of radii r_1 and r_2 with a dielectric continuum model of the solvent, where ϵ_0, ϵ_{op}, and ϵ_s are the vacuum permittivity, and optical and static dielectric constants of the bulk solvent, respectively. As we mentioned, in the eePI approach, this value can be approximated using the outer sphere free energy barrier that we capture.

By comparing both the distance-dependent trends in the dynamical term we compute ($\lim_{t\to\infty}\kappa(t)$), as well as the statistical term (k_{TST}), to those described by the different forms of the electron transfer rate described above, we should be able to address the ability of the eePI approach to capture the expected distance-dependence. Moreover, by comparing such trends, it might be possible to distinguish between regions of separation distance that follow adiabatic versus nonadiabatic pathways as indicated by an agreement between the eePI trends and those predicted by the various terms of the electron transfer rate. In combination with a comparison to literature values (of perhaps the rate itself or the free energy barrier) at particular separation distances, this analysis should provide a better sense of the possible shortcomings of the eePI approach and be able to indicate whether they are due to the free energy barrier calculation or a result of the transmission coefficient extracted by RPMD. One important factor to keep in mind throughout this analysis is the possibility that the constraint we impose on the metal-ligand bond length alters the transmission coefficient we observe from our simulations, as we discuss below.

Once these preliminary points are established, we can begin to address how these trends might change with a difference in the intermolecular space: How is this affected by solvent of varying polarities, or even when using different solvent models? Are we able to capture the expected differences that result by altering the chemical nature of the ligand structure? While these are more fundamental questions, their answers will certainly help set limitations and guide the use of the eePI approach for systems relevant to DSCs.

4.4 Exploring the Potential of the eePI Approach to Describe Asymmetric Electron Transfer Reactions

Do these simulations, even when parameterized to an intermediate, "transition state" model, maintain predictive power for less symmetric electron transfer reactions? Or is it possible to get decent estimates of cross-exchange rates from simulating sets of (symmetric) self-exchange processes?

In the eePI study detailed above (Chapter 2), we treated the self-exchange reaction by fixing the metal-ligand bond lengths to their "transition state" values after noting a minimal difference in the computed outer sphere free energy barrier to that found using a flexible bond. Moreover, because each reactant species maintains its (roughly) spherical symmetry irrespective of its oxidation state, this seems a reasonable representation if we would only like to compute the free energy barrier due to the reorganization of the solvent outer sphere that accompanies the electron transfer. However, provided that the large set of electron transfer couples that we would like to consider can deviate in geometry quite considerably from this simple model system (consider porphyrins, extended ligand structures, *etc.*), we

need to further explore possible limitations of this constrained transition state-like approach.

As we alluded to earlier, one should more closely explore the implications of fixing the metal-ligand bond lengths on the transmission coefficient we extract from the simulation. Could it be that by fixing this bond length, we diminish much of the contribution to the nuclear vibration, and an as a result, overestimate our $\kappa(t)$ at long times?

For adiabatic electron transfer in the normal regime, the Marcus cross-relation [114] can be employed as a useful point of departure for the analysis of our predicted rate values. [1] This cross-relation estimates the cross-exchange rate k_{12} between two chemically distinct moieties using their self exchange rates k_{11} and k_{22} as

$$k_{12} = (k_{11}k_{22}K_{12}f_{12})^{\frac{1}{2}} \tag{4.5}$$

with

$$\ln f_{12} = \frac{(\ln K_{12})^2}{4\ln(k_{11}k_{22}/Z^2)} \tag{4.6}$$

where K_{12} is the equilibrium constant of the cross reaction and Z is the bimolecular collision frequency in solution. What we do know about the pitfalls of the Marcus cross-exchange relationship [115–117] may offer valuable insight to help explain any deviations in our rate predictions from expected values. There is reason to believe that the more constrained our transition state representation, the closer the agreement with the Marcus cross-relation provided the effective dampening of intramolecular motions.

[1] If necessary, a similar relationship can also be used in the case of nonadiabatic reactions [58].

4.5 Exploring the "Potential" for Force Field Dependence

How strongly does the particular partial charge scheme or solvent model used influence the free energy barrier extracted with this method? Are any discrepancies dampened with increasing complexity of the TMCs?

We would like to determine how sensitive our computed free energy barriers are to the details of the partial charge assignment schemes and the adopted force field description. Comparing the influence each of these aspects has on the SM371 and Co(bpy) systems should help provide a sense of whether or not such dependences are diminished with increasing complexity.

4.6 Summary

In summary, we list suggested next steps toward addressing the questions discussed above. One should note that the most logical execution of these investigations is not as sequential as we describe above, and in fact, may be nearer the reverse order of their presentation above. First, we want to understand the implications of our choice of force field and then we can study the limitations of different 'transition state' representations in the eePI approach. Then, after having optimized the protocol with respect to these two aspects, we can begin to explore the ability of the eePI protocol to capture the distance dependence on the rate of electron transfer.

- Optimize the force field by testing the dependence of the outer sphere free energy barrier to electron transfer computed using the eePI protocol on the

choice of the (1) partial charge scheme, (2) solvent model, and (3) electron transfer reaction coordinate.

- Apply the eePI approach to compute the outer sphere free energy barrier and transmission coefficient for the SM371 and Co(bpy) self-exchanges, as well as their cross-exchange, for transition state representations where the TMCs are described as having multiple levels of rigidity: (1) fully rigid bodies, only free to rotate, (2) flexible, without constrained bonds, angles, *etc.*, and (3) a few variations in between these limiting cases, where the portion of the molecule associated with the defined "inner sphere" is treated more rigidly than the extended ligands, or perhaps a united atom approach is adopted for bulky ligand structures.
- For each level of rigidity, compare the cross exchange rate determined through the eePI simulations with those: (1) known from the literature, and (2) predicted using the appropriate cross-relations with the computed self-exchange rates – Does this comparison tell us about the boundaries of the eePI approach? Is there an obvious best choice of how we define our "transition state"?
- Having optimized the force field description, redetermine the outer sphere barrier and the transmission coefficient to the self- and cross- exchanges above to study their distance dependence, as captured by the eePI protocol.
- Compare the trends observed with the eePI protocol to the well-developed ideas of electron transfer theory discussed above to draw conclusions regarding the successes and limitations of this approach to describing electron transfer reactions of TMCs in the condensed-phase.

Provided that the explorations mentioned above indicate a bright future for the

eePI protocol, the answers to these very fundamental questions will certainly help us to best define our simulation parameters for the longer range goal of studying TMCs relevant to DSCs.

CHAPTER 5

QUANTIFYING THE ERROR OF TIME CORRELATION FUNCTIONS IN THE SEMICLASSICAL MIXED QUANTUM CLASSICAL INITIAL VALUE REPRESENTATION

5.1 Introduction

Semiclassical methods have had the most success describing complex chemical dynamics when the inclusion of quantum effects like coherence and tunneling is necessary. However, despite significant progress in the field, these methods are not presently applicable to many-body systems. Consider simulating the energy transfer that takes place when a highly excited NO molecule is scattered off of a gold surface [28]; ideally, to minimize computational expense, the components of the system involved directly in the energy transfer (*i.e.*, the NO molecule and the Au atoms in the vicinity of its incidence) in the most quantum (full semiclassical) limit, and treat those surrounding atoms in the classical limit. The mixed quantum-classical initial value representation (MQC-IVR) recently introduced by Antipov *et al.* [2] is a dynamically consistent way of doing this. They show how the MQC-IVR enables one to tune, by individual system degrees of freedom, between the full semiclassical- and classical-limits of the double Herman-Kluk (HK) time correlation function. However, the approximate nature of the mixed limit—where some degrees of freedom are treated in the full semiclassical limit, and others in the classical limit—is not well understood. Moreover, with increasing dimensionality, there is inherently more guesswork in the parameterization schemes involved in these calculations. The motivation of the work described herein is twofold: we would like to quantify the error associated with different choices of the "tuning

parameter" within the mixed-limit of the MQC-IVR framework, and then, using this information, optimize the MQC-IVR with respect to each of the simulation parameters as a step toward its application to systems of higher-dimensionality.

We explore here two possible routes of assessing the relative error associated with the MQC-IVR method. The first approach utilizes a series-based representation to compute the first order physical correction to the correlation function. Then, we consider an alternative way of deriving a correction term to report more generally on the error associated with the approximate propagation scheme. This second approach is more computationally friendly, and we believe could offer more general guidance than comparing the observable of interest directly.

We begin this chapter with a brief introduction to the semiclassical approximation of the quantum propagator, focusing on the initial value representation and its application to the evaluation of time correlation functions in Section 5.2.1. To preface the concepts exploited in the MQC-IVR, we share some "tricks" commonly used to evaluate the semiclassical expressions of interest. Then, the MQC-IVR approach to approximating quantum time correlation functions is more formally introduced.

Section 5.2.2 provides an overview of the semiclassical correction term introduced by Pollak et al. [118] to systematically improve the semiclassical evaluation of the quantum propagator. In the first approach to quantifying the error, we expand the correlation function in a series with this correction operator; by convention, the zeroth order term of the series propagator is that generally considered for semiclassical treatments, and every n^{th} term thereafter is assumed n^{th} order in this correction operator. Here, we derive the first order correction term for a general time correlation function using the MQC approach and look at the extreme

limiting cases. Then, we test its application to approximating the physical error in the average position of the one-dimensional anharmonic model system relative to the exact quantum result. However, initial analysis indicates that, at least for for the model system tested, it is computationally intractable for the timescales of interest. We explore the root of this limitation here.

In Section 5.2.4 we introduce a second approach that, while less physically motivated, proves to be a more feasible route to systematically quantify the relative error between different levels of tuning in the MQC-IVR. We demonstrate that with minimal computational effort, one is able to extract a relative measure of error specific to the chosen MQC-IVR tuning parameters. This approach also shows promise as a general metric one can use to not only assess the relative error of different choices of tuning parameters, but also to guide the choice of other simulation parameters, like the (arbitrary) coherent state widths, in an attempt to minimize sampling efforts.

5.2 Methodology

5.2.1 The semiclassical initial value representation

Semiclassical methods, or approaches that exploit sampling semiclassical trajectories evolved from initially quantized distributions, offer a route to approximating the quantum propagator to describe chemical dynamics in a way that is capable of capturing quantum effects like coherence and tunneling. The original, semiclassical Van Vleck-Gutzwiller approximation to the quantum propagator [119, 120] can be derived by taking the stationary phase approximation to its Feynman PI

representation [121]. However, the evaluation of this expression requires solving a boundary value problem, a prohibitive task for high-dimensional systems. Moreover, an additional numerical obstacle is faced due to the fact that this expression is divergent at turning points of the classical trajectories.

An alternative, semiclassical initial value representation (SC-IVR) approximation to the quantum propagator can be derived by exploiting a transformation from a sum of trajectories of the integral over final positions to that of initial momentum [122–125]. It has the added advantage that it lifts the singularities from the integrand. The coherent state form of the SC-IVR, originally proposed by Herman and Kluk (HK) [123], is expressed as

$$e^{-\frac{i}{\hbar}\hat{\mathrm{H}}t} = \frac{1}{(2\pi\hbar)^N}\int \mathrm{d}\mathbf{q}_0 \int \mathrm{d}\mathbf{p}_0\, C_t(\mathbf{p}_0,\mathbf{q}_0,\gamma_0,\gamma_t)\, e^{\frac{i}{\hbar}S_t(\mathbf{p}_0,\mathbf{q}_0)} |\mathbf{p}_t\mathbf{q}_t\gamma_t\rangle\langle\mathbf{p}_0\mathbf{q}_0\gamma_0| \quad (5.1)$$

for an N-dimensional system. The sets of initial momenta and positions $(\mathbf{p}_0, \mathbf{q}_0)$ of individual trajectories are classically time-evolved by t to $(\mathbf{p}_t, \mathbf{q}_t)$, where γ_0 and γ_t denote the coherent state widths. Here, $S_t(\mathbf{p}_0, \mathbf{q}_0; t)$ is the classical action along the trajectory,

$$S_t(\mathbf{p}_0,\mathbf{q}_0;t) = \int_0^t \mathrm{dt}'[\mathbf{p}(\mathrm{t}')\dot{\mathrm{q}}(\mathrm{t}') - \mathrm{H}(\mathbf{p},\mathbf{q};\mathrm{t}')], \quad (5.2)$$

and $C_t(\mathbf{p}_0, \mathbf{q}_0, \gamma_0, \gamma_t)$ is the HK prefactor

$$\begin{aligned} C_t(\mathbf{p}_0,\mathbf{q}_0,\gamma_0,\gamma_t) = \det\Bigg(\frac{1}{2}\Bigg[&\gamma_t^{\frac{1}{2}}\mathbf{M}_{qq}\gamma_0^{-\frac{1}{2}} + \gamma_t^{-\frac{1}{2}}\mathbf{M}_{pp}\gamma_0^{\frac{1}{2}} \\ &- i\hbar\gamma_t^{\frac{1}{2}}\mathbf{M}_{qp}\gamma_0^{\frac{1}{2}} + \frac{i}{\hbar}\gamma_t^{-\frac{1}{2}}\mathbf{M}_{pq}\gamma_0^{-\frac{1}{2}}\Bigg]\Bigg)^{1/2} \end{aligned} \quad (5.3)$$

with monodromy matrix elements $\mathbf{M}_{jk} = \frac{\partial j_t}{\partial k_0}$. The superposition of the matrix element probability amplitudes describing the semiclassical propagator acting on some initial state $|\mathbf{q}_i\rangle$ for time t until it reaches its final state, $|\mathbf{q}_f\rangle$, across large ensembles of classical trajectories is what enables these approaches to capture

quantum effects like coherence and tunneling. The position space coherent state wavefunctions are defined as

$$\langle \mathbf{x}|\mathbf{pq}\gamma\rangle = \left(\frac{\det(\gamma)}{\pi^{\mathbf{N}}}\right)^{\frac{\mathbf{1}}{\mathbf{4}}} \exp\left[-\frac{\mathbf{1}}{\mathbf{2}}(\mathbf{x}-\mathbf{q})\cdot\gamma\cdot(\mathbf{x}-\mathbf{q}) + \frac{\mathbf{i}}{\hbar}\mathbf{p}\cdot(\mathbf{x}-\mathbf{q})\right]. \tag{5.4}$$

Moving forward, explicit inclusion of the the coherent state widths are left out of our notation.

The Filinov transformation

Now, as an integral over initial points in phase space, the HK SC-IVR lends itself to standard Monte Carlo (MC) integration techniques for computing transition amplitudes. However, in its purest form, it poses a challenge to straightforward MC evaluation as the oscillatory nature of the integrand often results in poor sampling statistics. While some oscillatory features are essential for capturing quantum behavior, others just introduce 'noise' and contribute little to the overall integral. Over the years, in an attempt to extend semiclassical simulations to larger systems, several integral-filtering techniques have been employed [124]; the primary goal of these techniques is to dampen the 'noisey' oscillations and thus facilitate the evaluation of the integral by MC sampling. The Filinov transformation is of the most promising of the efforts. Here, an integral of the form

$$I = \int \mathrm{d}\mathbf{z}\, g(\mathbf{z}) e^{i\phi(\mathbf{z})} \tag{5.5}$$

is written as

$$I(\mathbf{c}) = \int \mathrm{d}\mathbf{z}\, g(\mathbf{z}) e^{i\phi(\mathbf{z})} F(\mathbf{z},\mathbf{c}), \tag{5.6}$$

where $\mathbf{z}$ is an N-dimensional vector, g and f are, in general, complex functions, and $F(\mathbf{z},\mathbf{c})$ is the smoothing factor given by

$$F(\mathbf{z},\mathbf{c}) = \det\left(\mathbf{I} + i\mathbf{c}\frac{\partial^2\phi}{\partial\mathbf{z}^2}\right)^{1/2} \exp\left[-\frac{1}{2}\frac{\partial\phi}{\partial\mathbf{z}}\mathbf{c}\frac{\partial\phi}{\partial\mathbf{z}}\right]. \tag{5.7}$$

The diagonal Filinov parameter matrix, $\mathbf{c}$, takes on positive values and determines the level of approximation being introduced by this approach. When $\mathbf{c} = 0$, the original integral is recovered, and when $\mathbf{c} \to \infty$, one is left with the stationary phase approximation to the integral. By choosing optimized intermediate values of $\mathbf{c}$, one aims to smooth the integrand to a point where MC statistics are improved, but the necessary description of quantum effects is maintained.

Real-time correlation functions

Real-time correlation functions provide a means of extracting dynamical macroscopic properties like chemical reaction rates, diffusion coefficients, and infrared absorption spectra from the microscopic physical quantities of systems in thermal equilibrium. Semiclassical methods offer a means to calculate these properties by evolving classical trajectories from quantum distributions. Consider the quantum mechanical time correlation function between operators $\hat{\mathrm{A}}$ and $\hat{\mathrm{B}}$, written generically as

$$C_{\mathrm{AB}}(t) = \mathrm{Tr}\left[\hat{\mathrm{A}}\mathrm{e}^{\frac{i}{\hbar}\hat{\mathrm{H}}t}\hat{\mathrm{B}}\mathrm{e}^{-\frac{i}{\hbar}\hat{\mathrm{H}}t}\right], \tag{5.8}$$

where $\hat{\mathrm{H}}$ is the Hamiltonian governing the system of interest. Straightforward substitution of the HK SC-IVR of the propagator is possible such that one arrives at an expression containing a double-phase space integral:

$$\begin{aligned} C_{\mathrm{AB},0}(t) = (2\pi\hbar)^{-2N} \int \mathrm{d}\mathbf{q}_0 \int \mathrm{d}\mathbf{p}_0 \int \mathrm{d}\mathbf{q}'_{\mathrm{t}} \int \mathrm{d}\mathbf{p}'_{\mathrm{t}} \\ \times\, C_t(\mathbf{p}_0, \mathbf{q}_0)\, C_{-t}(\mathbf{p}'_t, \mathbf{q}'_t) \\ \times\, e^{\frac{i}{\hbar}S_t(\mathbf{p}_0,\mathbf{q}_0)} e^{\frac{i}{\hbar}S_{-t}(\mathbf{q}'_t,\mathbf{p}'_t)} \\ \times\, \langle \mathbf{p}_0\mathbf{q}_0|\hat{\mathrm{A}}|\mathbf{p}'_0\mathbf{q}'_0\rangle\langle \mathbf{p}'_t\mathbf{q}'_t|\hat{\mathrm{B}}|\mathbf{p}_t\mathbf{q}_t\rangle. \end{aligned} \tag{5.9}$$

Instead of single trajectories, Eqn. 5.9 can now be evaluated by the classical evolution of sets of forward and backward trajectories. For one such set, a trajectory

beginning with initial conditions (p_0, q_0) is time evolved for t under the system Hamiltonian to (p_t, q_t). The operator $\hat{B}$ then acts on the system, resulting in a distribution of jumps in position and momentum, to arrive at initial conditions for backward trajectories; lastly, the system is time evolved $-t$ from each new initial condition, (p'_t, q'_t), to (p'_0, q'_0). While a seemingly straightforward approach, given the increased dimensionality and the fact that it contains two HK prefactors, the resulting integrand of Eqn. 5.9 is, in general, even more oscillatory than that of the SC-IVR transition amplitude, and so plagued by even worse numerical challenges.

The forward-backward IVR

Instead of evaluating the time correlation function as a set of two trajectories, separated by a distribution of jumps due to operator $\hat{B}$, combining the forward and backward stretches to form a single forward-backward semiclassical trajectory [126], has proven one of the more fruitful approaches. The basic concept and advantages of the forward-backward initial value representation (FB-IVR) are presented here to preface its use below. This approach is based upon the assumption that the operator $\hat{B}$ is a unitary operator; writing it in the general form $e^{-i\phi(p,q)}$, a single semiclassical trajectory can be considered whereby the system experiences a sequence of operations: $e^{\frac{i}{\hbar}\hat{\mathrm{H}}t}e^{-i\phi(p,q)}e^{-\frac{i}{\hbar}\hat{\mathrm{H}}t}$. In between the forward and backward trajectories, the system experiences an instantaneous jump specific to the operator $\hat{B}$ of interest. A schematic of FB-IVR approach is provided in Figure 5.1. The solid black lines represent the classical trajectories, and the dotted gray line the jump due to operator $\hat{B}$.

We consider the benefits of using this approach for a situation like that described below, where the average position is evaluated by considering the real-time

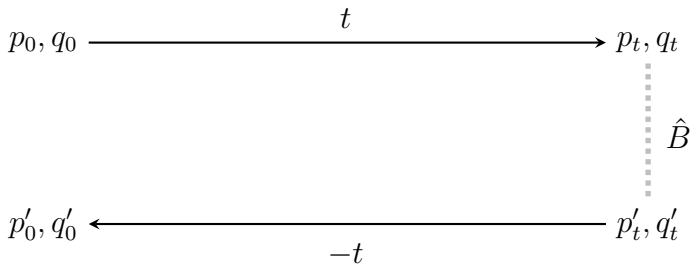

Figure 5.1: Schematic of the FB-IVR approach, showing a single forward-backward trajectory, for computing time correlation functions according to a SC-IVR of the propagator.

correlation function rewritten in terms of the integrals over the jumps due to $\hat{B}$, specifically for $\hat{B} = \hat{q}$ and $\hat{A} \equiv |\Psi_i\rangle\langle\Psi_i|$ where $|\Psi_i\rangle$ are coherent states. We can simplify this expression by performing the integral over the initial position of the backward trajectory (q'_t). This is numerically advantageous because it reduces the double phase space integral of expression (Eqn. 5.9) to a single phase space integration plus an additional integration over the momentum jump variable. Moreover, the forward-backward trajectory scheme also aids in cancellation of both the undesirable oscillatory phase of the integrand, as well as the magnitude of the HK prefactors. With increasing dimensionality, these nice features become increasingly necessary.

The MQC-IVR

The MQC-IVR is a promising method that exploits both of these concepts: it employs the Filinov filtration technique, introduced in line with the FB-IVR approach. It was proposed as a way to describe chemical dynamics *via* real-time correlation functions in a way that enables tuning between their full semiclassical and classical limits by individual degrees of freedom. With the ability to assign each degree of freedom its own "tuning parameter", it is possible to quantize only a few impor-

tant degrees of freedom in the presence of a more classically-behaved environment. The hope is that this will provide a dynamically consistent means to facilitate the extension of these semiclassical approaches to more complex molecular systems in a way that maintains their accuracy but makes them more computationally tractable.

We now review the MQC-IVR approach to evaluating a general matrix element of the form

$$\langle \mathbf{q}_f|\hat{U}|\mathbf{q}_i\rangle = \langle \mathbf{q}_f|e^{\frac{i}{\hbar}\hat{\mathrm{H}}t}\hat{\mathrm{B}}e^{-\frac{i}{\hbar}\hat{\mathrm{H}}t}|\mathbf{q}_i\rangle. \tag{5.10}$$

Substituting the HK form of the SC-IVR in place of the exact propagator, Eqn. 5.10 can be written as

$$\begin{aligned}\langle \mathbf{q}_f|\hat{U}|\mathbf{q}_i\rangle = (2\pi\hbar)^{-2N}\int \mathrm{d}\mathbf{q}_0 \int \mathrm{d}\mathbf{p}_0 \int \mathrm{d}\mathbf{q}'_\mathrm{t} \int \mathrm{d}\mathbf{p}'_\mathrm{t}\; C_t(\mathbf{p}_0,\mathbf{q}_0)C_{-t}(\mathbf{p}'_t,\mathbf{q}'_t) \\ \times\, e^{\frac{i}{\hbar}S_t(\mathbf{p}_0,\mathbf{q}_0)}e^{\frac{i}{\hbar}S_{-t}(\mathbf{q}'_t,\mathbf{p}'_t)}\langle \mathbf{q}_f|\mathbf{p}'_0\mathbf{q}'_0\rangle\langle \mathbf{p}'_t\mathbf{q}'_t|\hat{\mathrm{B}}|\mathbf{p}_t\mathbf{q}_t\rangle\langle \mathbf{p}_0\mathbf{q}_0|\mathbf{q}_i\rangle.\end{aligned} \tag{5.11}$$

The modified Filinov filtering technique is applied to Eqn. 5.11, where the complex phase considered is [2]

$$\begin{aligned}\phi(\mathbf{z}) =& S_t(\mathbf{p}_0,\mathbf{q}_0) + S_{-t}(\mathbf{p}_0,\mathbf{q}_0) + \frac{i}{2}(\mathbf{q}_0-\mathbf{q_i})\cdot\gamma_0\cdot(\mathbf{q}_0-\mathbf{q_i}) + \mathbf{p}_0\cdot(\mathbf{q}_0-\mathbf{q_i}) \\ &+ \frac{i}{2}(\mathbf{q}'_0-\mathbf{q_f})\cdot\gamma_0\cdot(\mathbf{q}'_0-\mathbf{q_f}) - \mathbf{p}'_0\cdot(\mathbf{q}'_0-\mathbf{q_f}) \\ &+ \frac{i}{4}\boldsymbol{\Delta}_q\cdot\gamma_t\cdot\boldsymbol{\Delta}_q + \frac{i}{4}\boldsymbol{\Delta}_p\cdot\gamma_t^{-1}\cdot\boldsymbol{\Delta}_p + \frac{1}{2}(\mathbf{p}'_t+\mathbf{p}_t)\cdot\boldsymbol{\Delta}_q,\end{aligned} \tag{5.12}$$

where $\hbar = 1$, $\mathbf{z} = (\mathbf{q}'_t, \mathbf{p}'_t, \mathbf{q}_0, \mathbf{p}_0)$, $\boldsymbol{\Delta}_x = \mathbf{x}'_t - \mathbf{x}_t$, $\mathbf{x} \in (\mathbf{p}, \mathbf{q})$ can be considered "jumps" at time t of the classical trajectory due to the operator $\hat{\mathrm{B}}$, which is assumed here to have no contribution to the complex phase. The unique feature of the MQC-IVR method is the way it takes advantage of this filtering approach to tune the level of approximation for individual system degrees of freedom through the Filinov parameter matrix.

To apply the filtering procedure, the derivatives of the phase are expressed

in terms of matrices $\mathbf{K}$ and $\mathbf{J}$, vector $\mathbf{y}$ (whose explicit forms are left out here for brevity), such that $\frac{\partial\phi(\mathbf{z})}{\partial\mathbf{z}} = \mathbf{K}\mathbf{y}$, and assuming the monodromy matrix has no explicit dependence on the integration variable $\frac{\partial^2\phi(\mathbf{z})}{\partial\mathbf{z}^2} = \mathbf{K}\frac{\partial\mathbf{y}}{\partial\mathbf{z}} = \mathbf{K}\mathbf{J}$ [127]. Finally, the Filinov damping factor (Eqn. 5.7) can be rewritten as [2]

$$\mathbf{F}(\mathbf{z};\tilde{\mathbf{c}}) = \frac{\det(\mathbf{K}^{\mathrm{T}} + i\tilde{\mathbf{c}}^{\mathrm{T}}\mathbf{J})^{\frac{1}{2}}}{\det(\mathbf{K}^{\mathrm{T}})^{\frac{1}{2}}} \exp\left[-\frac{1}{2}\mathbf{y}\cdot\tilde{\mathbf{c}}\cdot\mathbf{y}\right], \tag{5.13}$$

where $\tilde{\mathbf{c}} = \mathbf{K}^T\mathbf{c}\mathbf{K}$, such that Eqn. 5.11 can then be expressed as

$$\begin{aligned}\langle\mathbf{q}_f|\hat{U}|\mathbf{q}_i\rangle =& (2\pi)^{-2N}\int \mathrm{d}\mathbf{q}_0 \int \mathrm{d}\mathbf{p}_0 \int \mathrm{d}\boldsymbol{\Delta}_q \int \mathrm{d}\boldsymbol{\Delta}_p\, e^{iS_t(\mathbf{q}_0,\mathbf{p}_0)} e^{iS_{-t}(\mathbf{q}_t',\mathbf{p}_t')} \\ &\times C_t(\mathbf{p}_0,\mathbf{q}_0)\, C_{-t}(\mathbf{p}_t',\mathbf{q}_t') \frac{\det(\mathbf{K}^{\mathrm{T}} + i\tilde{\mathbf{c}}^{\mathrm{T}}\mathbf{J})^{\frac{1}{2}}}{\det(\mathbf{K}^{\mathrm{T}})^{\frac{1}{2}}} e^{-\frac{1}{2}\boldsymbol{\Delta}_q\cdot\mathbf{c}_q\cdot\boldsymbol{\Delta}_q} e^{-\frac{1}{2}\boldsymbol{\Delta}_p\cdot\mathbf{c}_p\cdot\boldsymbol{\Delta}_p} \\ &\times \langle\mathbf{q}_f|\mathbf{p}_0'\mathbf{q}_0'\rangle\langle\mathbf{p}_t'\mathbf{q}_t'|\hat{\mathrm{B}}|\mathbf{p}_t\mathbf{q}_t\rangle\langle\mathbf{p}_0\mathbf{q}_0|\mathbf{q}_i\rangle.\end{aligned} \tag{5.14}$$

Substituting this into the expression for the real-time correlation function Eqn. 5.8, on arrives at the MQC-IVR form for an N-dimensional system:

$$\begin{aligned}C_{\mathrm{AB},0}(t) =& (2\pi)^{-2N}\int \mathrm{d}\mathbf{q}_0 \int \mathrm{d}\mathbf{p}_0 \int \mathrm{d}\boldsymbol{\Delta}_q \int \mathrm{d}\boldsymbol{\Delta}_p\, e^{iS_t(\mathbf{q}_0,\mathbf{p}_0)} e^{iS_{-t}(\mathbf{q}_t',\mathbf{p}_t')} \\ &\times C_t(\mathbf{p}_0,\mathbf{q}_0)\, C_{-t}(\mathbf{p}_t',\mathbf{q}_t') \frac{\det(\mathbf{K}^{\mathrm{T}} + i\tilde{\mathbf{c}}^{\mathrm{T}}\mathbf{J})^{\frac{1}{2}}}{\det(\mathbf{K}^{\mathrm{T}})^{\frac{1}{2}}} e^{-\frac{1}{2}\boldsymbol{\Delta}_q\cdot\mathbf{c}_q\cdot\boldsymbol{\Delta}_q} e^{-\frac{1}{2}\boldsymbol{\Delta}_p\cdot\mathbf{c}_p\cdot\boldsymbol{\Delta}_p} \\ &\times \langle\mathbf{p}_0\mathbf{q}_0|\hat{\mathrm{A}}|\mathbf{p}_0'\mathbf{q}_0'\rangle\langle\mathbf{p}_t'\mathbf{q}_t'|\hat{\mathrm{B}}|\mathbf{p}_t\mathbf{q}_t\rangle,\end{aligned} \tag{5.15}$$

where the $|\mathbf{q}_i\rangle\langle\mathbf{q}_f|$ is the assumed form of $\hat{\mathrm{A}}$. In one instance, this method is applied to calculate the average position $\langle x_0(t)\rangle$ of a one-dimensional anharmonic model system defined by the potential,

$$V(x) = \frac{1}{2}m_x\omega_x^2x^2 - 0.1x^3 + 0.1x^4, \tag{5.16}$$

where, $m_x = 1$ a.u. and $\omega_x = \sqrt{2}$ a.u. This is simplified by considering the limit $\gamma_t \to \infty$ for the correlation function described by Eqn. 5.15 such that the integral over Δ_q can be taken analytically [128, 129]. Here $\hat{A} = |\Psi_i\rangle\langle\Psi_i|$, $|\Psi_i\rangle$ is a coherent

state $|p_i q_i\rangle$ with initial momentum $p_i = 0$ and position $q_i = 1$, and $\hat{B} = \hat{x}$. The final expression,

$$\begin{aligned}\langle x_0(t)\rangle =& 2^{-2}\pi^{-\frac{3}{2}} \int dq_0 \int dp_0 \int d\Delta_p \, \langle p_0 q_0|\Psi_i\rangle\langle\Psi_i|p_0' q_0'\rangle \\ & \times e^{i[S_t + S_{-t}]} x_t D_q(p_0, q_0, \Delta_p, c_p)\, e^{-\frac{1}{2}c_p\Delta_p},\end{aligned} \tag{5.17}$$

is then evaluated numerically using MC techniques with the sampling function

$$\omega(p_0, q_0, \Delta_p) = |\langle p_0 q_0|\Psi_i\rangle|^2 e^{-\frac{1}{2}c_p\Delta_p}. \tag{5.18}$$

To summarize the results of the one-dimensional anharmonic oscillator, we repeat these calculations. Figure 5.2 compares the MQC-IVR correlation functions for a range of choices of the tuning parameter c_p, with the exact quantum result included for comparison. Nearest the full semiclassical limit, where $c_p = 0.05$, the oscillations at long times are captured with a somewhat reduced amplitude. For $c_p = 100$, the correlation function was shown to be almost indistinguishable from the classical result (not included here for clarity), unable to capture the recurrence in oscillations. The intermediate values of c_p demonstrate the ability of the MQC-IVR to systematically tune between the full-semiclassical and classical limits of the real-time correlation function.

While the one-dimensional case underscores the tunability of the MQC-IVR, the extension to the two-dimensional model system highlights the utility of this sort of approach for describing complex systems. In this case, a heavier, harmonic mode is coupled to the previous anharmonic oscillator to illustrate how for complex systems, the coupling between modes may dampen quantum coherence effects. In the MQC-IVR framework, this corresponds to accurately describing quantum effects using a relatively large tuning parameter and far less computational effort [2]. An interesting observation noted in the original paper is that the tuning parameters necessary to achieve decent agreement with exact results depends largely on

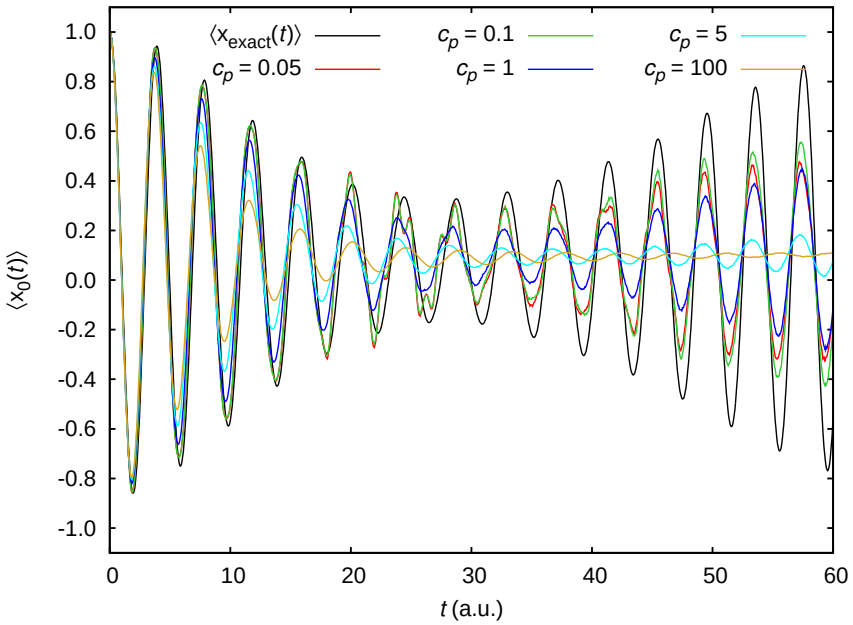

Figure 5.2: The average position $\langle x_0(t) \rangle$ of the one-dimensional anharmonic oscillator evaluated according to the MQC-IVR for $c_p = 0.05$ (red), 0.1 (green), 1 (blue), 5 (cyan), and 100 (gold), compared to the exact quantum result (black).

which mode is being observed. Ideally, we would like to derive a correction term that can more generally report on the error introduced by the MQC-IVR than observing the correlation functions themselves; this is the primary motive behind the work described herein.

Conveniently, methods like the Discrete Variable Representation can be used to calculate exact quantum correlation functions for a one-dimensional system. Therefore, by comparing these results to those obtained using the MQC-IVR, the physical error introduced in the average position by different levels of tuning in the MQC-IVR is easily quantifiable. This also serves as an approximate benchmark for the first, series-based error quantification approach outlined below; the leading order terms of the series are often sufficient for agreement with exact results [130–132], and so we compare the first order correction term derived here to this difference between the exact quantum result and the zeroth ordered semiclas-

sical treatment,

$$\delta \equiv \langle x_{\text{exact}}(t) \rangle - \langle x_0(t) \rangle. \tag{5.19}$$

In Figure 5.3, δ is plotted, for various choices of c_p. In general, the more ap-

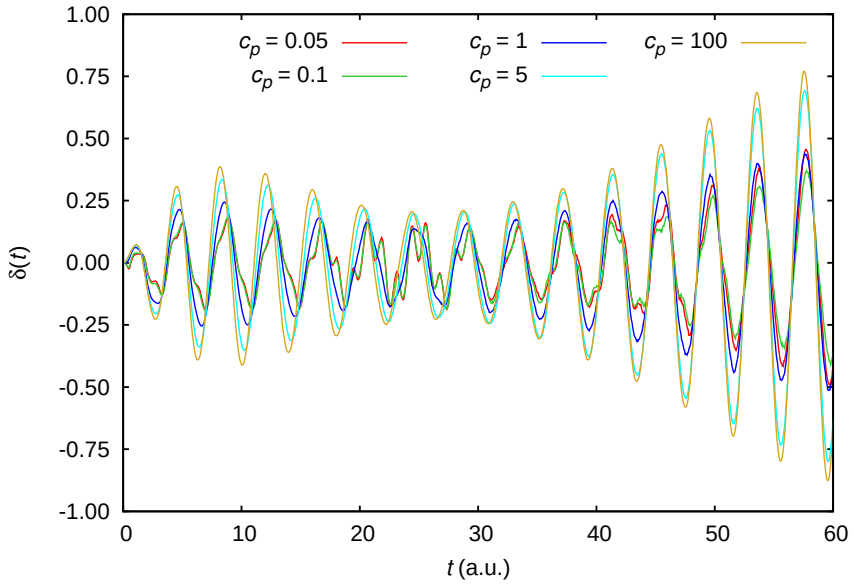

Figure 5.3: The difference (δ) between the average position of the anharmonic oscillator computed exactly, $\langle x_{\text{exact}}(t) \rangle$, and that according to the MQC-IVR, $\langle x_0(t) \rangle$, for $c_p = 0.05$ (red), $c_p = 0.1$ (green), $c_p = 1$ (blue), $c_p = 5$ (cyan), and $c_p = 100$ (gold).

proximate, or classical the treatment (larger c_p values, and thus smaller jumps at time t), the greater the error δ. Assuming that the first order correction term is sufficient for this model, δ for a given c_p should compare well to our computed $\langle x_1(t) \rangle$.

In Figure 5.4, the average of the exact position $\langle x_{ex}(t) \rangle$ is plotted against the position approximated by the MQC-IVR $\langle x_0(t) \rangle$ for different choices of the tuning parameter c_p as a compact representation of the error introduced for different levels of approximation within the MQC-IVR framework which is free of post-processing steps. Perfect agreement between the exact and semiclassical treatments would be indicated by a path oscillating back and forth on the line $y = x$, whereas those

whose paths trace the line $y = -x$ would be indicative of perfectly out of phase oscillations of equal magnitude in the two descriptions of position at a given time. Out of phase behavior is just barely visible at the long time limit of the case where $c_p = 100$ due to the loss in amplitude of the MQC-IVR approximation at these later times. Both a broadening of this path to form a sort of ellipse, or its tilt off of the diagonal, indicate a deviation of the semiclassical result from the exact solution. The width of the ellipse along the x-axis can, for example, serve as a measure of the relative error associated with each choice of the MQC-IVR tuning parameter. To maintain the ability to compare the error for different values of c_p at particular points in or spans of time in this condensed perspective, the color map can be used. Averaging along a particular time stretch of the paths over its distance from the line $y = x$ is another possible metric that could be used to assess the error over a given span of time without post-processing. However, while both Figures 5.3 and 5.4 are able to indicate the approximate nature of different choices of tuning parameter, as we mentioned above we would like to a more general approach to doing so. We resort to a semiclassical correction operator to guide the application of the MQC-IVR of real-time correlation functions to increasingly complex systems by:

1. providing a means to systematically quantify the error of the mixed-limit regime of tuning parameter choices, and
2. minimizing the error with respect to the tuning parameters and coherent state width.

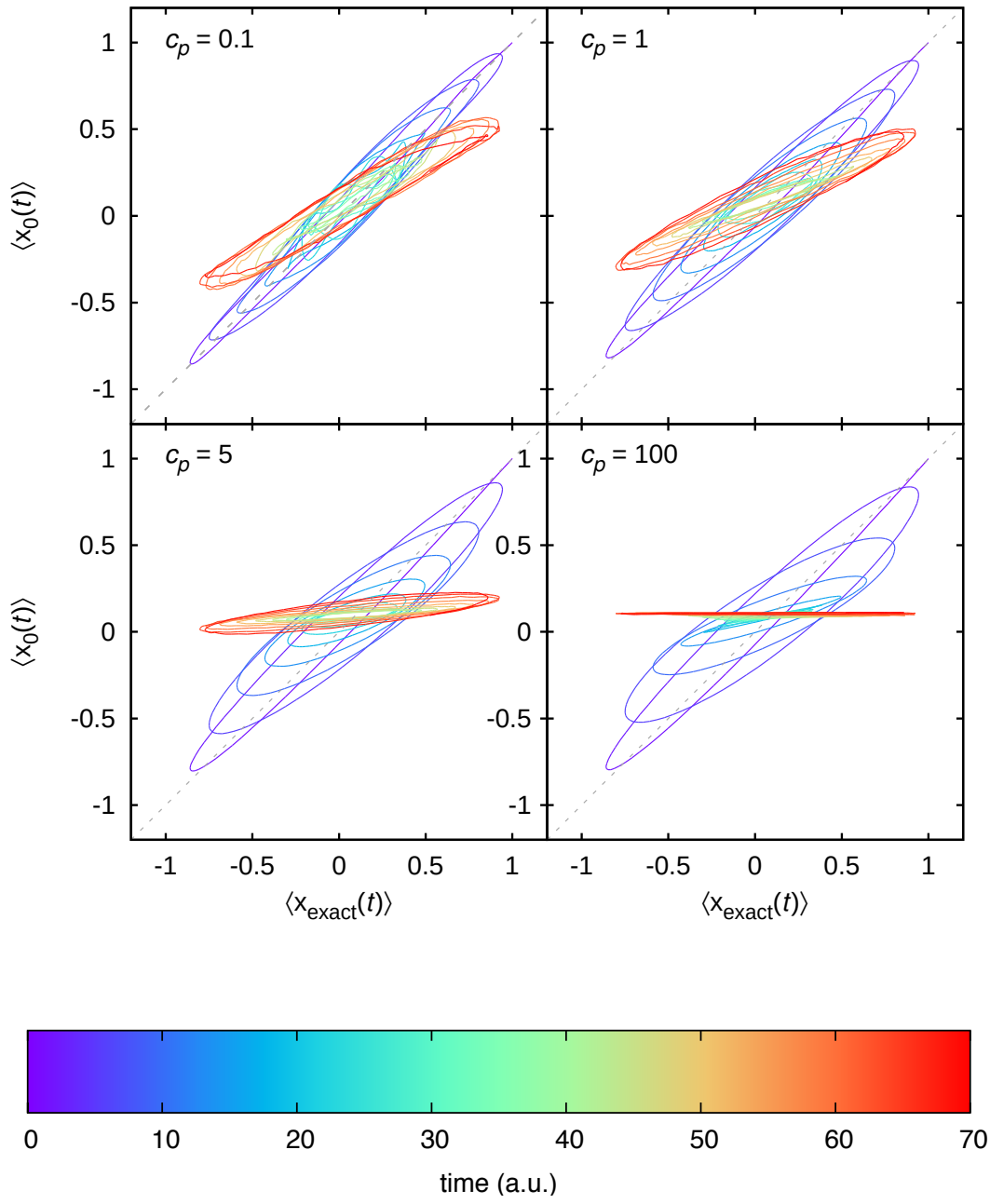

Figure 5.4: The semiclassically computed average position $\langle x_0(t)\rangle$ plotted relative to the exact $\langle x_{\text{exact}}(t)\rangle$ over 70 a.u. of time (indicated by the color gradient) for $c_p = 0.1, 1.0, 5.0, 100$.

5.2.2 A semiclassical correction

Comparing the Heisenberg equation of motion for a one-dimensional system with exact propagator $\hat{K}$,

$$i\hbar\frac{d}{dt}\hat{K} = \hat{H}\hat{K}, \tag{5.20}$$

to that with a semiclassical propagator, Pollak *et al.* show [118] that the SC-IVR propagator follows the expression

$$i\hbar\frac{d}{dt}\hat{K}_0 = \hat{H}\hat{K}_0 + \hat{G}. \tag{5.21}$$

For the HK propagator, this correction operator $\hat{G}$ is defined as [118]

$$\hat{G}(t) = \frac{1}{(2\pi\hbar)}\int dq_0 \int dp_0\, C_t(p_0, q_0, \gamma_0, \gamma_t) e^{\frac{i}{\hbar}S_t(p_0,q_0)} \Delta \mathrm{V}(\hat{\mathrm{q}}, \mathrm{t}) |\mathrm{p_t q_t \gamma_t}\rangle\langle \mathrm{p_0 q_0 \gamma_0}|, \tag{5.22}$$

where the explicit form of the potential difference operator $\Delta \mathrm{V}(\hat{\mathrm{q}}, \mathrm{t})$ depends on the system Hamiltonian of interest (provided below for the investigated model system). In this work, we explore two different approaches which employ the correction operator to systematically quantify the error in the MQC-IVR.

5.2.3 Deriving the first order physical correction to the MQC-IVR of real-time correlation functions

The SC-IVR series method developed by Pollak *et al.* [133] serves as a systematic approach to improve SC-IVR approximations through a series expansion. The zeroth order term of the series is the standard SC-IVR propagator, and each consecutive term is of increasing order in the correction operator. We briefly introduce this approach here and derive below (Section 5.2.3) the first order correction term to the real-time correlation function in the MQC-IVR framework [2].

Formally solving Eqn. 5.21, one can show that

$$\hat{K}_0 = \hat{K} + \frac{1}{i\hbar}\int_0^t d\tau\, \hat{K}(t-\tau)\hat{G}(\tau), \tag{5.23}$$

and representing the exact propagator as a series, a recursion relation is found [118]:

$$\hat{K}_{j+1}(t) = -\frac{1}{i\hbar}\int_0^t d\tau\, \hat{K}_j(t-\tau)\hat{G}(\tau). \tag{5.24}$$

The series is shown to converge quickly for multiple physically-motivated model systems [131, 133] and one can exploit this, comparing those terms that follow the zeroth order (conventional SC-IVR propagator) term for different SC-IVR treatments to quantify their relative errors.

To compute the corrections to a real-time correlation function in the MQC-IVR, we consider its series representation,

$$C_{\mathrm{AB}}(t) = C_{\mathrm{AB},0}(t) + C_{\mathrm{AB},1}(t) + \cdots, \tag{5.25}$$

where the j^{th} term is assumed to be of order j in the correction operator $\hat{G}$. While not strictly a convergent series, the first few terms are often sufficient to reproduce quantum results [133]. The zeroth order term is the original MQC-IVR expression [2], such that the first order correction term can be written as

$$C_{\mathrm{AB},1}(t) = \mathrm{Tr}\left[\hat{A}\hat{K}_0^{\dagger}(t)\hat{B}\hat{K}_1(t)\right] + \mathrm{c.c.} \tag{5.26}$$

Here, we attempt to take advantage of this series formalism to quantify the relative error associated with different tuning parameters as a way to guide there choice within the MQC-IVR description of real-time correlation functions.

Now, we derive the first order correction term to the real-time correlation function for an N-dimensional system according to the MQC-IVR approach. We begin

by expressing the first order correction term using the double HK initial value representation of the position matrix element as [134]

$$\begin{aligned}\langle \mathbf{q}_f|\hat{U}_1|\mathbf{q}_i\rangle = \frac{i}{\hbar}(2\pi\hbar)^{-3N}\int_0^t \mathrm{d}\tau \int \mathrm{d}\mathbf{q}_0 \int \mathrm{d}\mathbf{p}_0 \int \mathrm{d}\mathbf{q}_\tau \int \mathrm{d}\mathbf{p}_\tau \int \mathrm{d}\mathbf{q}_\mathrm{t}' \int \mathrm{d}\mathbf{p}_\mathrm{t}' \\ \times C_\tau(\mathbf{p}_0,\mathbf{q}_0)\, C_{t-\tau}(\mathbf{p}_{\bar{\tau}},\mathbf{q}_{\bar{\tau}})\, C_{-t}(\mathbf{p}_t',\mathbf{q}_t')\, e^{\frac{i}{\hbar}S_\tau(\mathbf{q}_0,\mathbf{p}_0)}\, e^{\frac{i}{\hbar}S_{t-\tau}(\mathbf{q}_{\bar{\tau}},\mathbf{p}_{\bar{\tau}})}\, e^{\frac{i}{\hbar}S_{-t}(\mathbf{q}_t',\mathbf{p}_t')} \\ \times \langle \mathbf{q}_f|\mathbf{p}_0'\mathbf{q}_0'\rangle\langle \mathbf{p}_t'\mathbf{q}_t'|\hat{B}|\mathbf{p}_t\mathbf{q}_t\rangle\langle \mathbf{p}_{\bar{\tau}}\mathbf{q}_{\bar{\tau}}|\Delta V(\hat{\mathbf{q}},\tau)|\mathbf{p}_\tau\mathbf{q}_\tau\rangle\langle \mathbf{p}_0\mathbf{q}_0|\mathbf{q}_i\rangle + \text{c.c.}\end{aligned} \tag{5.27}$$

To perform the modified Filinov filtering transformation, we collect the complex phase of the integrand in Eq. 5.27,

$$\begin{aligned}\phi(\mathbf{z}) = S_\tau(\mathbf{p}_0,\mathbf{q}_0) + S_{t-\tau}(\mathbf{p}_{\bar{\tau}},\mathbf{q}_{\bar{\tau}}) + S_{-t}(\mathbf{p}_t',\mathbf{q}_t') + \frac{i}{2}(\mathbf{q}_0-\mathbf{q}_i)\cdot\gamma_0\cdot(\mathbf{q}_0-\mathbf{q}_i) + \\ \mathbf{p}_0\cdot(\mathbf{q}_0-\mathbf{q}_i) + \frac{i}{2}(\mathbf{q}_0'-\mathbf{q}_f)\cdot\gamma_0\cdot(\mathbf{q}_0'-\mathbf{q}_f) - \mathbf{p}_0'\cdot(\mathbf{q}_0'-\mathbf{q}_f) \\ + \frac{i}{4}\boldsymbol{\Delta}_q\cdot\gamma_t\cdot\boldsymbol{\Delta}_q + \frac{i}{4}\boldsymbol{\Delta}_p\cdot\gamma_t^{-1}\cdot\boldsymbol{\Delta}_p + \frac{1}{2}(\mathbf{p}_t'+\mathbf{p}_t)\cdot\boldsymbol{\Delta}_q \\ + \frac{i}{4}\boldsymbol{\Delta}_q^c\cdot\gamma_\tau\cdot\boldsymbol{\Delta}_q^c + \frac{i}{4}\boldsymbol{\Delta}_p^c\cdot\gamma_\tau^{-1}\cdot\boldsymbol{\Delta}_p^c + \frac{1}{2}(\mathbf{p}_{\bar{\tau}}+\mathbf{p}_\tau)\cdot\boldsymbol{\Delta}_q^c,\end{aligned} \tag{5.28}$$

where the collective vector $\mathbf{z} = (\mathbf{q}_t', \mathbf{p}_t', \mathbf{q}_{\bar{\tau}}, \mathbf{p}_{\bar{\tau}}, \mathbf{q}_0, \mathbf{p}_0)$, we have introduced an additional "jump" in the positions and momenta of the classical trajectory $\boldsymbol{\Delta}_x^c = \mathbf{x}_{\bar{\tau}} - \mathbf{x}_\tau$ due to the potential difference operator (which stems from the correction operator), and following conventional wisdom we have neglected any contribution to the phase from both operators $\hat{\mathrm{B}}$ and $\Delta V(\hat{\mathbf{q}},\tau)$.

Following the MQC-IVR approach, we evaluate the first and second derivatives of the phase of the integrand with respect to $\mathbf{z}$, rewriting them in terms of matrix

$\mathbf{K}$, vector $\mathbf{k}$, and matrix $\mathbf{J}$, resulting in

$$\mathbf{Ky} = \begin{pmatrix} \mathbf{T}_{11} & \mathbf{T}_{12} & \mathbf{T}_{13} \\ \mathbf{T}_{21} & \mathbf{T}_{22} & \mathbf{T}_{23} \\ \mathbf{T}_{31} & \mathbf{T}_{32} & \mathbf{T}_{33} \end{pmatrix} \begin{pmatrix} \mathbf{q}'_0 - \mathbf{q}_f \\ \mathbf{q}_0 - \mathbf{q}_i \\ \boldsymbol{\Delta}_q \\ \boldsymbol{\Delta}_p \\ \boldsymbol{\Delta}^c_q \\ \boldsymbol{\Delta}^c_p \end{pmatrix}, \tag{5.29}$$

where

$$\mathbf{T}_{11} = \begin{pmatrix} -\mathbf{M}'^{\mathrm{T}}_{pq} + i\mathbf{M}'^{\mathrm{T}}_{qq}\gamma_0 & 0 \\ -\mathbf{M}'^{\mathrm{T}}_{pp} + i\mathbf{M}'^{\mathrm{T}}_{qp}\gamma_0 & 0 \end{pmatrix}, \mathbf{T}_{12} = \begin{pmatrix} \frac{i}{2}\gamma_t & -\frac{1}{2}\mathbf{I} \\ \frac{1}{2}\mathbf{I} & \frac{i}{2}\gamma_t^{-1} \end{pmatrix},$$

$$\mathbf{T}_{22} = \begin{pmatrix} \frac{1}{2}\overline{\mathbf{M}}^{\mathrm{T}}_{pq} - \frac{i}{2}\overline{\mathbf{M}}^{\mathrm{T}}_{qq}\gamma_t & -\frac{1}{2}\overline{\mathbf{M}}^{\mathrm{T}}_{qq} - \frac{i}{2}\overline{\mathbf{M}}^{\mathrm{T}}_{pq}\gamma_t^{-1} \\ \frac{1}{2}\overline{\mathbf{M}}^{\mathrm{T}}_{pp} - \frac{i}{2}\overline{\mathbf{M}}^{\mathrm{T}}_{qp}\gamma_t & -\frac{1}{2}\overline{\mathbf{M}}^{\mathrm{T}}_{qp} - \frac{i}{2}\overline{\mathbf{M}}^{\mathrm{T}}_{pp}\gamma_t^{-1} \end{pmatrix},$$

$$\mathbf{T}_{23} = \begin{pmatrix} \frac{i}{2}\gamma_\tau & -\frac{1}{2}\mathbf{I} \\ \frac{1}{2}\mathbf{I} & \frac{i}{2}\gamma_\tau^{-1} \end{pmatrix}, \mathbf{T}_{31} = \begin{pmatrix} 0 & i\gamma_0 \\ 0 & \mathbf{I} \end{pmatrix},$$

$$\mathbf{T}_{33} = \begin{pmatrix} \frac{1}{2}\mathbf{M}^{0\mathrm{T}}_{pq} - \frac{i}{2}\mathbf{M}^{0\mathrm{T}}_{qq}\gamma_\tau & -\frac{1}{2}\mathbf{M}^{0\mathrm{T}}_{qq} - \frac{i}{2}\mathbf{M}^{0\mathrm{T}}_{pq}\gamma_\tau^{-1} \\ \frac{1}{2}\mathbf{M}^{0\mathrm{T}}_{pp} - \frac{i}{2}\mathbf{M}^{0\mathrm{T}}_{qp}\gamma_\tau & -\frac{1}{2}\mathbf{M}^{0\mathrm{T}}_{qp} - \frac{i}{2}\mathbf{M}^{0\mathrm{T}}_{pp}\gamma_\tau^{-1} \end{pmatrix},$$

$$\mathbf{T}_{13} = \mathbf{T}_{21} = \mathbf{T}_{32} = \begin{pmatrix} 0 & 0 \\ 0 & 0 \end{pmatrix}, \tag{5.30}$$

and

$$\frac{\partial^2\phi(\mathbf{z})}{\partial\mathbf{z}^2} = \frac{\partial}{\partial\mathbf{z}}\mathbf{K}\mathbf{y} = \mathbf{K}\frac{\partial\mathbf{y}}{\partial\mathbf{z}} = \mathbf{K}\mathbf{J} = \mathbf{K}\begin{pmatrix} \mathbf{M}'_{qq} & \mathbf{M}'_{qp} & 0 & 0 & 0 & 0 \\ 0 & 0 & 0 & 0 & \mathbf{I} & 0 \\ \mathbf{I} & 0 & -\overline{\mathbf{M}}_{qq} & -\overline{\mathbf{M}}_{qp} & 0 & 0 \\ 0 & \mathbf{I} & -\overline{\mathbf{M}}_{pq} & -\overline{\mathbf{M}}_{pp} & 0 & 0 \\ 0 & 0 & \mathbf{I} & 0 & -\mathbf{M}^0_{qq} & -\mathbf{M}^0_{qp} \\ 0 & 0 & 0 & \mathbf{I} & -\mathbf{M}^0_{pq} & -\mathbf{M}^0_{pp} \end{pmatrix}, \tag{5.31}$$

respectively. The monodromy matrix elements $\mathbf{M}^0$ are associated with the initial stretch of the forward trajectory prior to the jump at time τ, $\overline{\mathbf{M}}$ with the stretch of the forward trajectory after time τ, and $\mathbf{M}'$ for the backward trajectory. The superscript T denotes the matrix transpose. To remove the dependence of the damping factor on the initial and final states of the system, we choose the Filinov parameter matrix to be

$$\tilde{\mathbf{c}} = \begin{pmatrix} 0 & 0 & 0 & 0 & 0 & 0 \\ 0 & 0 & 0 & 0 & 0 & 0 \\ 0 & 0 & \mathbf{c}_q & 0 & 0 & 0 \\ 0 & 0 & 0 & \mathbf{c}_p & 0 & 0 \\ 0 & 0 & 0 & 0 & \mathbf{c}^c_q & 0 \\ 0 & 0 & 0 & 0 & 0 & \mathbf{c}^c_p \end{pmatrix}, \tag{5.32}$$

where each term is as an $N \times N$ diagonal matrix such that the exponential factor of the modified Filinov smoothing term (Eq. 5.13) becomes

$$\begin{aligned} \exp\left[-\frac{1}{2}\mathbf{y}\cdot\tilde{\mathbf{c}}\cdot\mathbf{y}\right] = &\exp\left[-\frac{1}{2}\boldsymbol{\Delta}_q\cdot\mathbf{c}_q\cdot\boldsymbol{\Delta}_q\right]\exp\left[-\frac{1}{2}\boldsymbol{\Delta}_p\cdot\mathbf{c}_p\cdot\boldsymbol{\Delta}_p\right] \\ &\times\exp\left[-\frac{1}{2}\boldsymbol{\Delta}^c_q\cdot\mathbf{c}^c_q\cdot\boldsymbol{\Delta}^c_q\right]\exp\left[-\frac{1}{2}\boldsymbol{\Delta}^c_p\cdot\mathbf{c}^c_p\cdot\boldsymbol{\Delta}^c_p\right]. \end{aligned} \tag{5.33}$$

The MQC-IVR expression for the first order correction term of the position matrix

element (Eq. 5.27) is then

$$\begin{aligned}\langle \mathbf{q}_f|\hat{U}_1|\mathbf{q}_i\rangle = i(2\pi)^{-3N}\int_0^t \mathrm{d}\tau \int \mathrm{d}\mathbf{q}_0 \int \mathrm{d}\mathbf{p}_0 \int \mathrm{d}\boldsymbol{\Delta}_{\mathrm{q}}^{\mathrm{c}} \int \mathrm{d}\boldsymbol{\Delta}_{\mathrm{p}}^{\mathrm{c}} \int \mathrm{d}\boldsymbol{\Delta}_{\mathrm{q}} \int \mathrm{d}\boldsymbol{\Delta}_{\mathrm{p}} \\ \times\, C_\tau(\mathbf{p}_0,\mathbf{q}_0)\, C_{t-\tau}(\mathbf{p}_{\bar{\tau}},\mathbf{q}_{\bar{\tau}})\, C_{-t}(\mathbf{p}'_t,\mathbf{q}'_t)\frac{\det(\mathbf{K}^{\mathrm{T}}+i\tilde{\mathbf{c}}^{\mathrm{T}}\mathbf{J})^{\frac{1}{2}}}{\det(\mathbf{K}^{\mathrm{T}})^{\frac{1}{2}}} \\ \times\, e^{-\frac{1}{2}\boldsymbol{\Delta}_q\cdot\mathbf{c}_q\cdot\boldsymbol{\Delta}_q} e^{-\frac{1}{2}\boldsymbol{\Delta}_p\cdot\mathbf{c}_p\cdot\boldsymbol{\Delta}_p} e^{-\frac{1}{2}\boldsymbol{\Delta}_q^c\cdot\mathbf{c}_q^c\cdot\boldsymbol{\Delta}_q^c} e^{-\frac{1}{2}\boldsymbol{\Delta}_p^c\cdot\mathbf{c}_p^c\cdot\boldsymbol{\Delta}_p^c} \\ \times\, e^{i\left[S_\tau(\mathbf{q}_0,\mathbf{p}_0)+S_{t-\tau}(\mathbf{q}_{\bar{\tau}},\mathbf{p}_{\bar{\tau}})+S_{-t}(\mathbf{q}'_t,\mathbf{p}'_t)\right]}\langle \mathbf{q}_f|\mathbf{p}'_0\mathbf{q}'_0\rangle \\ \times\, \langle \mathbf{p}'_t\mathbf{q}'_t|\hat{B}|\mathbf{p}_t\mathbf{q}_t\rangle\langle \mathbf{p}_{\bar{\tau}}\mathbf{q}_{\bar{\tau}}|\Delta\hat{V}|\mathbf{p}_\tau\mathbf{q}_\tau\rangle\langle \mathbf{p}_0\mathbf{q}_0|\mathbf{q}_i\rangle + \text{c.c.},\end{aligned} \tag{5.34}$$

where we have set $\hbar = 1$. The MQC-IVR prefactor for the first order correction term is defined as

$$D(\mathbf{R}) \equiv C_\tau(\mathbf{p}_0,\mathbf{q}_0)\, C_{t-\tau}(\mathbf{p}_{\bar{\tau}},\mathbf{q}_{\bar{\tau}})\, C_{-t}(\mathbf{p}'_t,\mathbf{q}'_t)\frac{\det(\mathbf{K}^{\mathrm{T}}+i\tilde{\mathbf{c}}^{\mathrm{T}}\mathbf{J})^{\frac{1}{2}}}{\det(\mathbf{K}^{\mathrm{T}})^{\frac{1}{2}}}, \tag{5.35}$$

where $\mathbf{R} = (\mathbf{p}_0, \mathbf{q}_0, \boldsymbol{\Delta}_p, \boldsymbol{\Delta}_q, \boldsymbol{\Delta}_p^c, \boldsymbol{\Delta}_q^c, \mathbf{c}_p, \mathbf{c}_q, \mathbf{c}_p^c, \mathbf{c}_q^c)$. The denominator of Eq. 5.35 is simplified using the following property of $3N \times 3N$ block matrices

$$\begin{aligned}\det\begin{pmatrix}\mathbf{S}_{11} & \mathbf{S}_{12} & \mathbf{S}_{13}\\ \mathbf{S}_{21} & \mathbf{S}_{22} & \mathbf{S}_{23}\\ \mathbf{S}_{31} & \mathbf{S}_{32} & \mathbf{S}_{33}\end{pmatrix} = \det([\mathbf{S}_{11}-\mathbf{S}_{13}\mathbf{S}_{33}^{-1}\mathbf{S}_{31}]- \\ [\mathbf{S}_{12}-\mathbf{S}_{13}\mathbf{S}_{33}^{-1}\mathbf{S}_{32}][\mathbf{S}_{22}-\mathbf{S}_{23}\mathbf{S}_{33}^{-1}\mathbf{S}_{32}]^{-1}[\mathbf{S}_{21}-\mathbf{S}_{23}\mathbf{S}_{33}^{-1}\mathbf{S}_{31}]) \\ \times \det(\mathbf{S}_{22}-\mathbf{S}_{23}\mathbf{S}_{33}^{-1}\mathbf{S}_{32})\det(\mathbf{S}_{33}),\end{aligned} \tag{5.36}$$

such that the prefactor can be expressed as

$$D(\mathbf{R}) = \det(2i\gamma_0)^{-\frac{1}{2}}\det(\mathbf{K}^{\mathrm{T}}+i\tilde{\mathbf{c}}^{\mathrm{T}}\mathbf{J})^{\frac{1}{2}}. \tag{5.37}$$

In this way, the first order correction term of the MQC-IVR expression of the

real-time correlation function can be written as

$$\begin{aligned} C_{\mathrm{AB},1}(t) = i(2\pi)^{-3N} \int_0^t \mathrm{d}\tau \int \mathrm{d}\mathbf{q}_0 \int \mathrm{d}\mathbf{p}_0 \int \mathrm{d}\boldsymbol{\Delta}_{\mathrm{q}}^{\mathrm{c}} \int \mathrm{d}\boldsymbol{\Delta}_{\mathrm{p}}^{\mathrm{c}} \int \mathrm{d}\boldsymbol{\Delta}_{\mathrm{q}} \int \mathrm{d}\boldsymbol{\Delta}_{\mathrm{p}} \\ \times D(\mathbf{R}) e^{-\frac{1}{2}\boldsymbol{\Delta}_q \cdot \mathbf{c}_q \cdot \boldsymbol{\Delta}_q} e^{-\frac{1}{2}\boldsymbol{\Delta}_p \cdot \mathbf{c}_p \cdot \boldsymbol{\Delta}_p} e^{-\frac{1}{2}\boldsymbol{\Delta}_q^c \cdot \mathbf{c}_q^c \cdot \boldsymbol{\Delta}_q^c} e^{-\frac{1}{2}\boldsymbol{\Delta}_p^c \cdot \mathbf{c}_p^c \cdot \boldsymbol{\Delta}_p^c} \\ \times e^{i\left[S_\tau(\mathbf{q}_0,\mathbf{p}_0) + S_{t-\tau}(\mathbf{q}_{\bar{\tau}},\mathbf{p}_{\bar{\tau}}) + S_{-t}(\mathbf{q}'_t,\mathbf{p}'_t)\right]} \\ \times \langle \mathbf{p}_0\mathbf{q}_0|\hat{A}|\mathbf{p}'_0\mathbf{q}'_0\rangle \langle \mathbf{p}'_t\mathbf{q}'_t|\hat{B}|\mathbf{p}_t\mathbf{q}_t\rangle \langle \mathbf{p}_{\bar{\tau}}\mathbf{q}_{\bar{\tau}}|\Delta\hat{V}|\mathbf{p}_\tau\mathbf{q}_\tau\rangle + \text{c.c.} \end{aligned} \tag{5.38}$$

The MQC-IVR limits of the first order correction term, $C_{AB,1}(t)$

As one would expect, in the limit that $\tilde{\mathbf{c}} \to 0$, the MQC prefactor (Eq. 5.35) reduces to the original HK form, and the exponential factors due to the jumps in position and momentum go to unity, therefore returning the original, pre-filtered (full semiclassical) version of the first order correction term to the correlation function [134].

Determining the limit in which $\tilde{\mathbf{c}} \to \infty$ requires a bit more work. First, taking the limit of just those parts of Eq. 5.38 dependent on $\tilde{\mathbf{c}}$,

$$\begin{aligned} \lim_{\tilde{\mathbf{c}}\to\infty} e^{-\frac{1}{2}\boldsymbol{\Delta}_q \cdot \mathbf{c}_q \cdot \boldsymbol{\Delta}_q} e^{-\frac{1}{2}\boldsymbol{\Delta}_p \cdot \mathbf{c}_p \cdot \boldsymbol{\Delta}_p} e^{-\frac{1}{2}\boldsymbol{\Delta}_q^c \cdot \mathbf{c}_q^c \cdot \boldsymbol{\Delta}_q^c} e^{-\frac{1}{2}\boldsymbol{\Delta}_p^c \cdot \mathbf{c}_p^c \cdot \boldsymbol{\Delta}_p^c} D(\mathbf{R}) \\ = (2\pi)^{2N} \delta(\boldsymbol{\Delta}_q)\delta(\boldsymbol{\Delta}_p)\delta(\boldsymbol{\Delta}_q^c)\delta(\boldsymbol{\Delta}_p^c) D(\mathbf{R})^\infty \end{aligned} \tag{5.39}$$

where

$$D(\mathbf{R})^\infty = \lim_{\tilde{\mathbf{c}}\to\infty} \det(\mathbf{c}_q \mathbf{c}_p \mathbf{c}_p^c \mathbf{c}_p^c)^{-\frac{1}{2}} \det(2i\gamma_0)^{-\frac{1}{2}} \det(\mathbf{K}^{\mathrm{T}} + i\mathbf{c}^{\mathrm{T}}\mathbf{J})^{\frac{1}{2}}. \tag{5.40}$$

To evaluate the remaining limit, we first rewrite the second term of Eq. 5.40,

$$\begin{aligned}\det(\mathbf{K}^{\mathrm{T}} + i\mathbf{c}^{\mathrm{T}}\mathbf{J}) &= \det\begin{pmatrix} \mathbf{X}\mathbf{M}' & 0 & \mathbf{Y} \\ \mathbf{Z} & -\mathbf{Z}^{\mathrm{T}}\overline{\mathbf{M}} & 0 \\ 0 & \tilde{\mathbf{Z}} & -\tilde{\mathbf{Z}}^{\mathrm{T}}\mathbf{M}^0 \end{pmatrix}, \\ &= \det\left(\mathbf{X}\mathbf{M}' + \mathbf{Y}(-\tilde{\mathbf{Z}}^{\mathrm{T}}\mathbf{M}^0)^{-1}\tilde{\mathbf{Z}}(-\mathbf{Z}^{\mathrm{T}}\overline{\mathbf{M}})^{-1}\mathbf{Z}\right) \\ &\quad \times \det\left(-\mathbf{Z}^{\mathrm{T}}\overline{\mathbf{M}}\right)\det\left(-\tilde{\mathbf{Z}}^{\mathrm{T}}\mathbf{M}^0\right) \\ &= \det\left((\mathbf{X}\mathbf{M}')_{11}\mathbf{H}_{22} - (\mathbf{X}\mathbf{M}')_{12}\mathbf{H}_{21}\right)\det\left(-\mathbf{Z}^{\mathrm{T}}\overline{\mathbf{M}}\right)\det\left(-\tilde{\mathbf{Z}}^{\mathrm{T}}\mathbf{M}^0\right)\end{aligned} \tag{5.41}$$

where we used the property of determinants in Eq. 5.36, $\mathbf{H} = \mathbf{Y}(-\tilde{\mathbf{Z}}^{\mathrm{T}}\mathbf{M}^0)^{-1}\tilde{\mathbf{Z}}(-\mathbf{Z}^{\mathrm{T}}\overline{\mathbf{M}})^{-1}\mathbf{Z}$ and subscripts refer to corresponding matrix elements. Then,

$$D(\mathbf{R})^{\infty} = \det\left(\frac{2}{\gamma_0}(\gamma_o\mathbf{M}^{\mathrm{full}}_{qq} + \mathbf{M}^{\mathrm{full}}_{pp}\gamma_0 - i\gamma_0\mathbf{M}^{\mathrm{full}}_{qp}\gamma_0 + i\mathbf{M}^{\mathrm{full}}_{pq})\right)^{\frac{1}{2}} \tag{5.42}$$

where $\mathbf{M}^{\mathrm{full}}_{jk} = \frac{\partial j'_0}{\partial k_0}$ signify monodromy matrix elements of the entire trajectory (both forward and the backward stretches). Substituting this into Eq. 5.38 and analytically evaluating the integrals over the jump variables, which now only exist in the delta functions, corresponds to a trajectory which does not experience a jump in position or momentum at either time τ or t. Now, as the system takes the same path for the complete forward (both stretches) as for the backward propagation, $\mathbf{M}^{\mathrm{full}}_{jk} = \delta_{jk}\mathbf{I}$ such that $D(\mathbf{R})^{\infty}$ reduces to 2. The final expression for the limiting case where $\tilde{\mathbf{c}} \to \infty$ is

$$\begin{aligned}C_{\mathrm{AB},1}(t) = i\pi^{-N}\int_0^t \mathrm{d}\tau \int \mathrm{d}\mathbf{q}_0 \int \mathrm{d}\mathbf{p}_0 \\ \times e^{i\left[S_\tau(\mathbf{q}_0,\mathbf{p}_0)+S_{t-\tau}(\mathbf{q}_{\bar{\tau}},\mathbf{p}_{\bar{\tau}})+S_{-t}(\mathbf{q}'_t,\mathbf{p}'_t)\right]} \\ \times \langle \mathbf{p}_0\mathbf{q}_0|\hat{A}|\mathbf{p}'_0\mathbf{q}'_0\rangle\langle \mathbf{p}'_t\mathbf{q}'_t|\hat{B}|\mathbf{p}_t\mathbf{q}_t\rangle\langle \mathbf{p}_{\bar{\tau}}\mathbf{q}_{\bar{\tau}}|\hat{\Delta V}|\mathbf{p}_\tau\mathbf{q}_\tau\rangle + \text{c.c.}\end{aligned} \tag{5.43}$$

5.2.4 A second approach to quantifying the MQC-IVR error

Here, we introduce a second approach to quantifying the error inherent in different approximate levels of the MQC-IVR. It has been demonstrated that computing the expectation value of the correction operator itself can guide optimization of the series representation [130]. We adapt an analogous approach here for the real-time correlation function in an effort to find a general metric for reporting on the relative error associated with different parameterization choices in the MQC-IVR.

Heisenberg's equation of motion (Eqn. 5.20) tells us that that the time derivative of the quantum propagator is proportional to acting on the propagator by the system Hamiltonian $\hat{H}$. However, in the case of an approximate, semiclassical form of the propagator, these two terms are no longer equivalent and so the equation is modified to include a correction term $\hat{G}$ which accounts for their difference (recall Eqn. 5.21). In the first approach described above, following the work of Pollak *et al.* [133], we solve this differential equation to define the physical correction to the real-time correlation function. Here, we instead apply the modified time evolution equation (Eqn. 5.21) to the time correlation function of interest. Specifically, by substituting the HK initial value representation of the propagator into the exact real-time correlation function (Eqn. 5.8) and considering its derivative, through Eqn. 5.21 we arrive at the expression

$$i\hbar\frac{d}{dt}\mathrm{Tr}\left[\hat{A}\hat{K}_0^\dagger\hat{B}\hat{K}_0\right] = \left(\mathrm{Tr}\left[\hat{A}\hat{H}\hat{K}_0^\dagger\hat{B}\hat{K}_0\right] + \mathrm{Tr}\left[\hat{A}\hat{G}^\dagger\hat{B}\hat{K}_0\right]\right) + \text{c.c.} \tag{5.44}$$

Noting that the last term would be absent in the exact treatment, this term is considered here a correction, or measure of error, associated with the MQC-IVR correlation function. We compute this correction by considering a matrix element

of the form

$$\langle \mathbf{q}_f|\hat{K}_0^\dagger \hat{B}\hat{G}|\mathbf{q}_i\rangle = (2\pi)^{-2N}\int \mathrm{d}\mathbf{q}_0 \int \mathrm{d}\mathbf{p}_0 \int \mathrm{d}\mathbf{q}'_t \int \mathrm{d}\mathbf{p}'_t\, e^{iS_t(\mathbf{q}_0,\mathbf{p}_0)} e^{iS_{-t}(\mathbf{q}'_t,\mathbf{p}'_t)} \\ \times C_t(\mathbf{p}_0,\mathbf{q}_0) C_{-t}(\mathbf{p}'_t,\mathbf{q}'_t) \langle \mathbf{q}_f|\mathbf{p}'_0\mathbf{q}'_0\rangle\langle \mathbf{p}'_t\mathbf{q}'_t|\hat{\mathrm{B}}\hat{\Delta \mathrm{V}}|\mathbf{p}_t\mathbf{q}_t\rangle\langle \mathbf{p}_0\mathbf{q}_0|\mathbf{q}_i\rangle, \tag{5.45}$$

where we have inserted both an instance of the correction operator (Eqn. 5.22) as well as the (backward) HK propagator. Applying the modified Filinov transformation technique employed in the MQC-IVR [2], we arrive at the expression

$$\langle \mathbf{q}_f|\hat{K}_0^\dagger \hat{B}\hat{G}|\mathbf{q}_i\rangle = (2\pi)^{-2N}\int \mathrm{d}\mathbf{q}_0 \int \mathrm{d}\mathbf{p}_0 \int \mathrm{d}\boldsymbol{\Delta}_q \int \mathrm{d}\boldsymbol{\Delta}_p\, e^{iS_t(\mathbf{q}_0,\mathbf{p}_0)} e^{iS_{-t}(\mathbf{q}'_t,\mathbf{p}'_t)} \\ \times C_t(\mathbf{p}_0,\mathbf{q}_0) C_{-t}(\mathbf{p}'_t,\mathbf{q}'_t) \frac{\det(\mathbf{K}^{\mathrm{T}} + i\tilde{\mathbf{c}}^{\mathrm{T}}\mathbf{J})^{\frac{1}{2}}}{\det(\mathbf{K}^{\mathrm{T}})^{\frac{1}{2}}} e^{-\frac{1}{2}\boldsymbol{\Delta}_q\cdot\mathbf{c}_q\cdot\boldsymbol{\Delta}_q} e^{-\frac{1}{2}\boldsymbol{\Delta}_p\cdot\mathbf{c}_p\cdot\boldsymbol{\Delta}_p} \\ \times \langle \mathbf{q}_f|\mathbf{p}'_0\mathbf{q}'_0\rangle\langle \mathbf{p}'_t\mathbf{q}'_t|\hat{\mathrm{B}}\hat{\Delta \mathrm{V}}|\mathbf{p}_t\mathbf{q}_t\rangle\langle \mathbf{p}_0\mathbf{q}_0|\mathbf{q}_i\rangle, \tag{5.46}$$

where, similar to before, the assumption was made that neither operator $\hat{\mathrm{B}}$ or $\hat{\Delta \mathrm{V}}$ contribute to the imaginary phase of the integrand. Everything is defined as before with the exception of the matrices in the MQC-IVR prefactor term ($\mathbf{K}$, $\tilde{\mathbf{c}}$, and $\mathbf{J}$); we refer the reader to Ref. [2] for their details. This expression has the advantage over the physical first order correction term that it scales with the original MQC-IVR expression; it does not require the introduction of an additional integral over time, avoiding the necessity to propagate trajectories for all intermediate times $\tau < t$ for every t, or the introduction of a third set of phase space variables. Moreover, it avoids other sampling challenges one faces when evaluating the first order physical correction term, as we discuss below.

Because an exact analogy of this correction does not exist by definition, the full semiclassical-limit of the MQC-IVR is employed as a baseline for comparison. Notably, this comes with nearly no additional computational cost. The hope is that this correction can be used as a more general indicator of the relative error

associated with different parameterization choices in the MQC-IVR than assessing the time correlation function itself; as we saw [2], the optimal choice of tuning parameter in the two-dimensional model system depended on the mode being observed. Using this form of the correction, we hope to be able to introduce a metric that, along with information like the computational cost of competing parameter choices, can be exploited to optimize these simulations for systems of increasing complexity. We expect this to prove particularly useful for exploring the mixed limit scenarios of the MQC-IVR.

5.3 The Application of These Approaches to the Anharmonic Oscillator Model System

To demonstrate the ability of these approaches to quantify the error inherent in the correlation function defined by different levels of tuning the MQC-IVR [2], we calculate both the physical first order correction term to the average position $\langle x_1(t)\rangle$, as well as the more tractable correction term $\langle K_0^\dagger BG\rangle$ described in the previous section for the anharmonic model system (Eqn. 5.16).

Approach I: Evaluate $\langle x_1(t)\rangle$ *via* the *f*FB Scheme

To compute $\langle x_1(t)\rangle$, we consider a correlation of the form of Eqn. 5.38, where again, $\hat{A} = |\Psi_i\rangle\langle\Psi_i|$, $|\Psi_i\rangle \equiv |p_i q_i\rangle$, $p_i = 0$, $q_i = 1$, and $\hat{B} = \hat{x}$. In an effort to avoid introducing any additional error to $\langle x_1(t)\rangle$, absent by convention in the zeroth order term, we are interested in computing the full semiclassical limit with respect to the correction jump at time τ, $(c_p^c, c_q^c) \rightarrow 0$. We can simplify the

expression further by taking advantage of the specific form of the operator acting at time t, $\hat{B} = B(\hat{q})$, such that the first order correction to the correlation function (Eqn. 5.38) can be evaluated in the limit that $\gamma_t \rightarrow \infty$ [2, 128, 129],

$$\begin{aligned} C_{\mathrm{AB},1}(t) = i(2\pi)^{-3}(4\pi)^{\frac{1}{2}} \int_0^t d\tau \int dq_0 \int dp_0 \int d\Delta_q^c \int d\Delta_p^c \int d\Delta_p \\ \times e^{-\frac{1}{2}\Delta_p \cdot c_p \cdot \Delta_p} \\ \times e^{i\left[S_\tau(q_0,p_0)+S_{t-\tau}(q_{\bar{\tau}},p_{\bar{\tau}})+S_{-t}(q_t',p_t')\right]} \langle \Psi_i | p_0' q_0' \rangle \\ \times D_q B(\hat{q}_t) \langle p_{\bar{\tau}} q_{\bar{\tau}} | \hat{\Delta V} | p_\tau q_\tau \rangle \langle p_0 q_0 | \Psi_i \rangle + \text{c.c.}, \end{aligned} \tag{5.47}$$

where the prefactor in this case is expressed as

$$\begin{aligned} D_q = \ & \det(2i\gamma_0)^{-\frac{1}{2}} (4\gamma_\tau)^{-1} [iM_{pq}^0 + \gamma_0 M_{pp}^0 + \gamma_\tau (M_{qq}^0 - iM_{qp}^0 \gamma_0)] \\ & \times [(iM_{pp}' - \gamma_0 M_{qp}')(\bar{M}_{qq} - i\gamma_\tau \bar{M}_{qp}) + c_p(-M_{pp}' \bar{M}_{pq} - M_{pq}' \bar{M}_{qq} \\ & + i\bar{M}_{pq} M_{qp}' \gamma_0 + i\bar{M}_{qq} M_{qq}' \gamma_0 + i\bar{M}_{pp} M_{pp}' \gamma_\tau \\ & + iM_{pq}' \bar{M}_{qp} \gamma_\tau + \bar{M}_{pp} M_{qp}' \gamma_0 \gamma_\tau + \bar{M}_{qp} M_{qq}' \gamma_0 \gamma_\tau)]. \end{aligned} \tag{5.48}$$

Using the modified time evolution equation (Eqn. 5.21), one can show that [118]

$$\hat{\Delta V}(\hat{q}, t) = \frac{\gamma_t^2}{2}[\hat{q} - q_t]^2 - \frac{\gamma_t}{2} + i\frac{\dot{C}_t(p_0, q_0)}{C_t(p_0, q_0)} + V(q_t) - V(\hat{q}) + V'(q_t)[\hat{q} - q_t], \tag{5.49}$$

assuming constant coherent state widths, γ_0 and γ_t.

To evaluate the matrix element due to the correction jump, $\langle p_{\bar{\tau}} q_{\bar{\tau}} | \hat{\Delta V} | p_\tau q_\tau \rangle$, we insert a complete set of position states which allows us to pull the $\hat{\Delta V}$ out of the overlap and perform the integral over states to arrive at

$$\begin{aligned} C_{\mathrm{AB},1}(t) = \ & i2^{-2}\pi^{-5/2} \int_0^t d\tau \int dq_0 \int dp_0 \int d\Delta_q^c \int d\Delta_p^c \int d\Delta_p \\ & \times e^{-\frac{1}{2}\Delta_p \cdot c_p \cdot \Delta_p} \\ & \times e^{i\left[S_\tau(q_0,p_0)+S_{t-\tau}(q_{\bar{\tau}},p_{\bar{\tau}})+S_{-t}(q_t',p_t')\right]} \langle \Psi_i | p_0' q_0' \rangle \\ & \times D_q B(\hat{q}_t) \langle p_{\bar{\tau}} q_{\bar{\tau}} | p_\tau q_\tau \rangle \Delta V(q_\tau) \langle p_0 q_0 | \Psi_i \rangle + \text{c.c.}, \end{aligned} \tag{5.50}$$

where $\Delta V(q_\tau)$ is defined for the anharmonic model system as

$$\begin{aligned}\Delta V(q_\tau) = \frac{1}{160}\sqrt{\frac{\pi}{\gamma_\tau}}\Big[&80{\gamma_\tau}^2 q_\tau^2 + 16q_\tau^2(-10m_x{\omega_x}^2 + (3-4q_\tau)q_\tau) \\ &+ (8q_\tau(-10{\gamma_\tau}^2 + 10m{\omega_x}^2 + q_\tau(-3+4q_\tau))\Xi)/\gamma_\tau \\ &- \Xi^4/{\gamma_\tau}^4 - (12(\gamma_\tau + \Xi^2))/{\gamma_\tau}^3 + (20({\gamma_\tau}^2 - m\omega_x^2) \\ &\times (2\gamma_\tau + \Xi^2))/{\gamma_\tau}^2 - (-2\Xi \times (6 + \Xi^2/\gamma_\tau)){\gamma_\tau}^{-2}\Big] \\ &- \gamma_\tau/2 + i\frac{\dot{C}_\tau}{C_\tau} + V(q_\tau)\end{aligned} \tag{5.51}$$

with $\Xi = i(p_\tau - p_{\bar{\tau}}) + \gamma_\tau(q_\tau + q_{\bar{\tau}})$. Notably, for the harmonic oscillator, this term goes to zero.

The final form of the correlation function associated with the first order correction term 5.50 is evaluated according to the fFB scheme depicted in Figure 5.5. Instead of a single forward trajectory from point (p_0, q_0), at all possible intermediate values τ between time 0 and t a jump in both momentum and position takes place due to the operator $\hat{\Delta V}$:

$$\begin{aligned} p_\tau + \Delta_p^c &\to p_{\bar{\tau}} \\ q_\tau + \Delta_q^c &\to q_{\bar{\tau}}. \end{aligned} \tag{5.52}$$

The system is then time evolved by $(t-\tau)$, from $(p_{\bar{\tau}}, q_{\bar{\tau}})$ to (p_t, q_t). Figure 5.5 depicts this scheme for one such intermediate value of τ, however, a jump after every step $\Delta\tau$ for $0 \leq \tau \leq t$ is required for the evaluation of the correlation function at time t. Then, like in the FB-IVR, operator $\hat{B}$ acts on the system (in this case, just inducing a jump in momentum) and then the backward trajectory from point (p'_t, q'_t) to (p'_0, q'_0) ensues.

The integrals over phase space variables are evaluated using standard MC techniques with the sampling function

$$\Theta(q_0, p_0, \Delta_q^c, \Delta_p^c, \Delta_p) = |\langle p_0 q_0|\Psi_i\rangle|^2 e^{-\frac{1}{2}\Delta_p \cdot c_p \cdot \Delta_p} e^{-\frac{1}{2}\Delta_q^c \cdot \alpha_q^c \cdot \Delta_q^c} e^{-\frac{1}{2}\Delta_p^c \cdot \beta_p^c \cdot \Delta_p^c}. \tag{5.53}$$

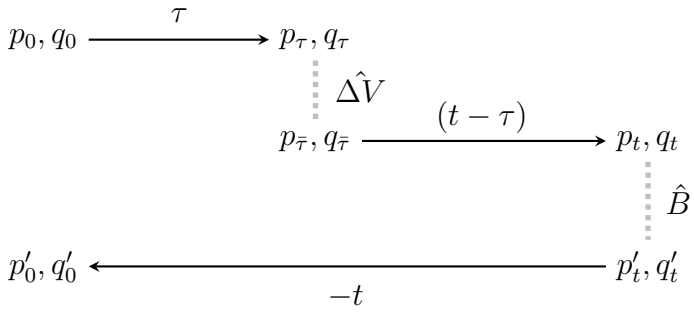

Figure 5.5: Schematic of the fFB approach

The exponential terms involving the jumps due to the correction operator (Δ_q^c and Δ_p^c) are included as a means to sample the jump at time τ, though it does introduce constraints on the sampling scheme. Ideally, we would like to explore jumps in these phase space variables consistent with the $(c_p^c, c_q^c) \;\rightarrow\; 0$ limits. However, we choose a value near the semiclassical-limit, $\alpha_q^c = \beta_p^c = 1$, to avoid sampling fFB trajectories where the instantaneous jumps due to the correction operator far exceed those induced by operator $\hat{B}$. In this scenario, we suspect that the greater discrepancy between the two forward stretches than that between the latter forward and backward trajectories may hinder sampling efforts, possibly by requiring a greater number of trajectories for convergence, as there would likely be much less cancelling of the phase between the (full) forward and backward stretches. Nevertheless, the near semiclassical limit seems sufficient.

Then, we evaluate

$$\begin{aligned} F = \; & i\,(2\pi^2 c_p\,\alpha_q^c\,\beta_p^c)^{-\frac{1}{2}} \int_0^t d\tau\, \frac{\langle \Psi_i | p'_0 q'_0 \rangle}{\langle \Psi_i | p_0 q_0 \rangle} e^{i\left[S_\tau(q_0,p_0)+S_{t-\tau}(q_{\bar{\tau}},p_{\bar{\tau}})+S_{-t}(q'_t,p'_t)\right]} \\ & \times D_q\, x_t\, \Delta V \langle p_{\bar{\tau}} q_{\bar{\tau}} | p_\tau q_\tau \rangle e^{\frac{1}{2}\Delta_q^c \cdot \alpha_q^c \cdot \Delta_q^c} e^{\frac{1}{2}\Delta_p^c \cdot \beta_p^c \cdot \Delta_p^c} \end{aligned} \tag{5.54}$$

for each of the classically evolved trajectories that stem from the MC sampled initial distribution of points in phase space. To ensure the correct branch of the complex square root in D_q is taken, we track the Maslov index. After averaging over all successful trajectories, the integral over τ is evaluated by Simpson's rule

with dτ set equal to the simulation time step; two times the real part of the result is the first order correction to the average position, $\langle x_1(t)\rangle$.

Preliminary results for the evaluation of the real-time correlation function corresponding to $\langle x_1(t)\rangle$ MQC-IVR of the correlation indicate that the timestep (dt) originally implemented for this model system (0.05 a.u.) is insufficient for discretization along τ in the first order correction term. This is illustrated here in Figure 5.6 as a dt-dependence of $\langle x_1(t)\rangle$ for various values of c_p. The δ values for each c_p, defined earlier as the difference between the exact quantum and (zeroth order) MQC-IVR result (Eqn. 5.19), is also included here as a rough guide for comparison. However, it should be noted that their direct comparison is only a robust measure in the case that no higher order terms contribute to the series, and this has not yet been explored for this model system in the MQC-IVR framework. The number of trajectories sampled is provided in Table 5.1, and equivalent for all of the timesteps presented at each value of c_p.

Table 5.1: Number of semiclassical trajectories used to evaluate $\langle x_1(t)\rangle$ at short times for different values of c_p in the MQC-IVR

c_p	N_{traj}
0.1	3.6×10^7
1	3.6×10^7
5	2.4×10^7
100	1.2×10^7

While across all values of c_p tested here, using either of the two smaller timesteps (0.01 or 0.005 a.u.) appears to improve the agreement with δ, it is interesting to note that at the later time shown, the intermediate timestep agrees best with δ. We believe that this is likely the result of needing higher order terms in the series for perfect agreement with the exact result and possibly a degree of approximation that was introduced by placing a constraint on sampling the cor-

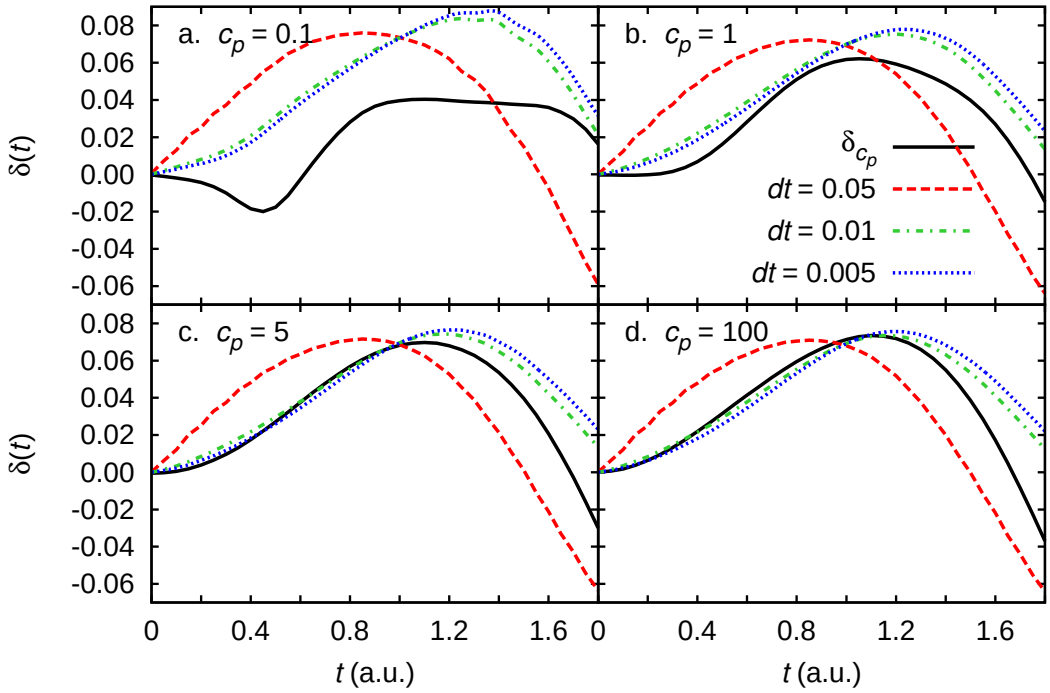

Figure 5.6: The first order correction to the position correlation function $\langle x_1(t)\rangle$ computed using $dt = 0.05$ (dashed red), 0.01 (dot-dashed green), and 0.005 a.u. (dotted blue), compared to the known difference δ (solid black) between the zeroth order MQC-IVR term and the exact result for (a.) $c_p = 0.1$, (b.) $c_p = 1$, (c.) $c_p = 5$, and (d.) $c_p = 100$.

rection jump at time τ, though this discrepancy has not been explored. Notably, it also seems as though the timestep dependence is worse in the more semiclassical cases, whereas the more approximately treated correlation function suffers less. This suggests that with increasing system complexity, or perhaps even with a model system made of up heavier modes, that the series-based approach at quantifying the MQC-IVR error may not be as limited as here by the choice of timestep.

Provided that none of the time integrated quantities of the system were showing a similar timestep-dependence, the integral over τ which evaluated by discretization as dt is suspect. In Figure 5.7 we plot both the real and imaginary parts of $\Delta V(\tau)$ for $t = 60$ a.u. For purely diagnostic purposes, a single trajectory was run with

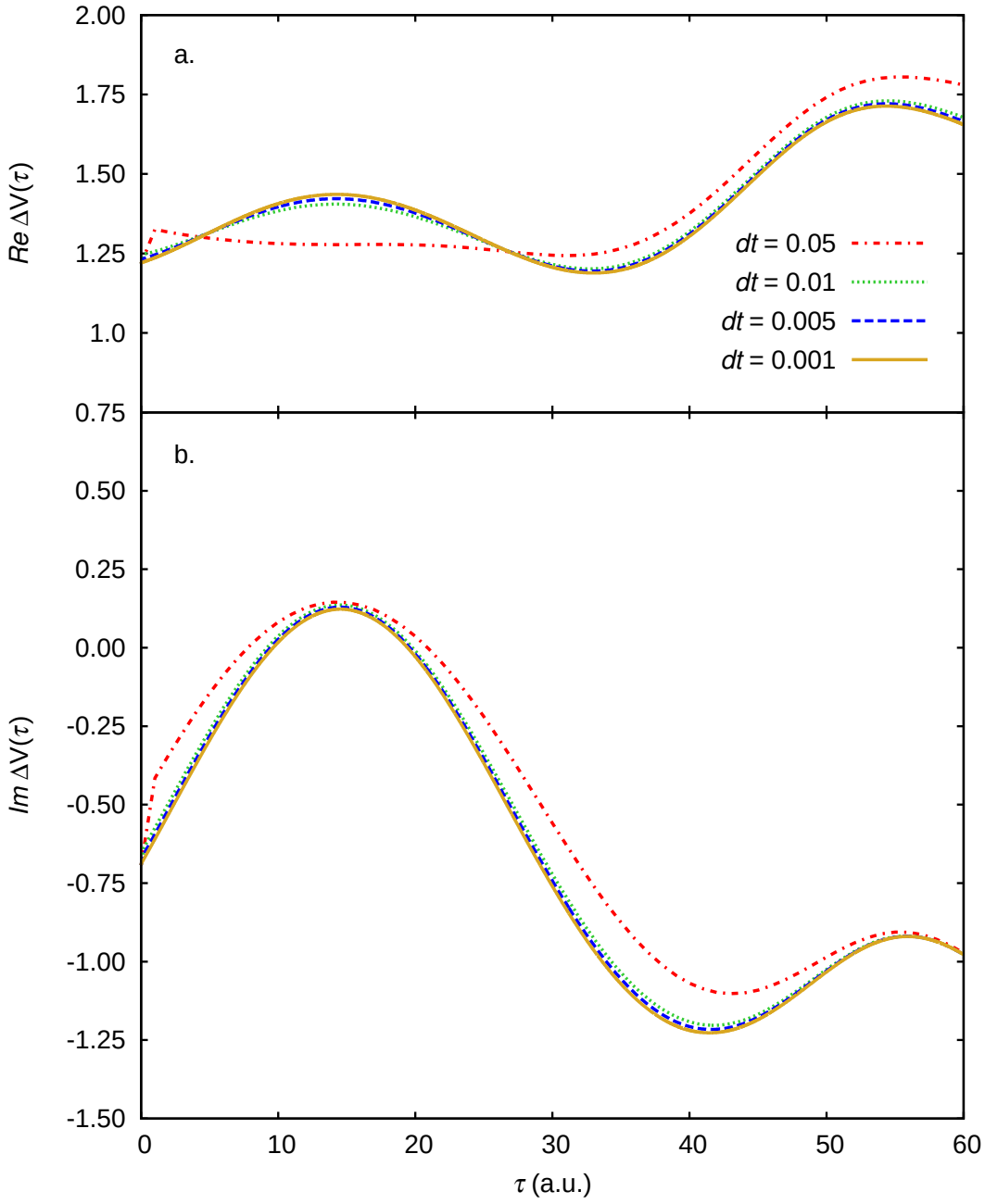

Figure 5.7: The (a.) real and (b.) imaginary parts of $\Delta V(\tau)$, which are integrated over time for evaluation of the first order correction term at $t = 60$ a.u., computed using $dt = 0.05$ (dot-dashed red), 0.01 (dotted green), 0.005 (dashed blue), and 0.001 a.u. (solid gold).

$c_p = 0.1$, $c_q = 1000$, and $\gamma_t = \gamma_0 = \sqrt{2}$ for a variety of timesteps. The convergence with respect to dt at smaller values demonstrates that the dt-dependence being witnessed is not necessarily due to the inability of Simpson's rule to approximate this time integral with $d\tau = dt$, but rather that ΔV itself needs to be evaluated more frequently. That the integrand experiences a dt-dependence through the necessary integration over all possible values of $\tau < t$ for each $\Delta V(t)$ indicates that we would need to rely on a prohibitively small timestep along the forward τ trajectory before we can accurately determine the time integral. Possible solutions might be to adopt an alternative integration scheme, or to simply use a smaller timestep for the τ time evolution than the remainder of the forward and then backward trajectory. However, at least for this model system, this is already quite a computationally expensive calculation and the necessary timestep would be too limiting for our purposes. Moreover, for the same reason, we do not explore the implications of this timestep-dependence at longer times.

Nevertheless, we suspect that computing the first order correction term could still prove a fruitful approach for other model systems, where perhaps the ΔV is more well behaved and so as a result there is less of a constraint on the choice of timestep. Moreover, in cases where there are more classical modes present to dampen quantum effects, it may be possible that by combination of both fewer MC sampling points necessary for convergence and the ability to use a larger timestep, the series-based correction might be suitable. However, one should note that this does require evaluating an additional phase-space integral and so in general will be a more computationally expensive task than the zeroth order term. For now, we turn to a second approach to calculate the relative error between MQC-IVR approximations which is far more tractable for the timescales of interest. In addition, it has the added advantage that for systems where this first approach does

prove feasible, there is potential with this next method to optimize the first order correction term attempted above with respect to the simulation parameters (*e.g.*, the choice coherent state width at time t [130]).

Approach II: Compute $\langle K_0^\dagger BG\rangle$

To get a sense of the error inherent in the propagation scheme due to the level of approximation introduced in the semiclassical MQC-IVR approach, we evaluate $\mathrm{Tr}\left[\hat{A}\hat{K}_0^\dagger\hat{B}\hat{G}\right]$ through the general matrix element $\langle\mathbf{q}_f|\hat{K}_0^\dagger\hat{B}\hat{G}|\mathbf{q}_i\rangle$ (Eqn 5.46), derived in the MQC-IVR framework. Again, with $\hat{A} = |\Psi_i\rangle\langle\Psi_i|$, $|\Psi_i\rangle \equiv |p_i q_i\rangle$, $p_i = 0$, $q_i = 1$, and $\hat{B} = \hat{x}$, we first determine the functional form of the term $\langle p_t' q_t'|\hat{x}\hat{\Delta}\hat{\mathrm{V}}|p_t q_t\rangle$ for the one-dimensional anharmonic oscillator (Eqn. 5.16). Inserting a complete set in position space between these two operators, and performing the integral analytically, we arrive at

$$\begin{aligned}\langle\Psi_i|\hat{K}_0^\dagger\hat{B}\hat{G}|\Psi_i\rangle = (2\pi)^{-2}\int \mathrm{d}q_0 \int \mathrm{d}p_0 \int d\Delta_q \int d\Delta_p\, e^{iS_t(q_0,p_0)}e^{iS_{-t}(q_t',p_t')} \\ \times D\, e^{-\frac{1}{2}\Delta_q\cdot c_q\cdot\Delta_q}e^{-\frac{1}{2}\Delta_p\cdot c_p\cdot\Delta_p} \\ \times \langle\Psi_i|p_0' q_0'\rangle\langle p_t' q_t'|p_t q_t\rangle\chi_t\langle p_0 q_0|\Psi_i\rangle,\end{aligned} \tag{5.55}$$

with

$$\begin{aligned}\chi_t = \frac{1}{320\gamma_t^5}\sqrt{\frac{\pi}{\gamma_t}}\Bigg[80\Xi\gamma_t^4\left(2i\frac{\dot{C}_\tau}{C_\tau} - \gamma_t + 2V(q_t) - 2V'(q_t)\cdot q_t + \gamma_t^2 q_t^2\right) \\ + 80\gamma_t^3\left(V'(q_t) - \gamma_t^2 q_t\right)(2\gamma_t + \Xi^2) - 20\gamma_t^3(\gamma_t^2 - m\omega_x^2) \\ - \Xi\left((6 + \Xi^2/\gamma_t) - (60\gamma_t^2 + \Xi^4 + 20\gamma_t\Xi^2)\right) \\ + 2\gamma_t\left(\Xi^4 + 12\gamma_t(\gamma_t + \Xi^2)\right)\Bigg]\end{aligned} \tag{5.56}$$

where Ξ is defined as before, except now a jump at time t (instead of τ), and D is equivalent to the general MQC-IVR prefactor [2]. The FB scheme used to evaluate this expression is similar to that used in the original MQC-IVR work,

with the additional evaluation of χ_t at each time and jumps in *both* the position and momentum at time t. As mentioned previously, this greatly reduces the computational effort as compared to the first order correction term, scaling with the original MQC-IVR expression.

The function used to sample the initial points in phase space and their jumps at time t is now

$$\Theta(q_0, p_0, \Delta_q, \Delta_p) = |\langle p_0 q_0 | \Psi_i \rangle|^2 e^{-\frac{1}{2}\Delta_q \cdot c_q \cdot \Delta_q} e^{-\frac{1}{2}\Delta_p \cdot \beta_p \cdot \Delta_p}. \tag{5.57}$$

From these points, we take the average of

$$F = (c_p c_q)^{-\frac{1}{2}} \frac{\langle \Psi_i | p_0' q_0' \rangle}{\langle \Psi_i | p_0 q_0 \rangle} e^{i\left[S_t(q_0,p_0) + S_{-t}(q_t',p_t')\right]} D\chi_t \langle p_t' q_t' | p_t q_t \rangle \tag{5.58}$$

evaluated at each point in time over all of the semiclassical trajectories.

In Figure 5.8, we compare the real and imaginary parts of $\langle K_0^\dagger BG \rangle$ for various choices of c_p, where $c_q = 1000$ always, and $\gamma_t = \gamma_0$. In both cases, there is an interesting resemblance to the average position correlation function (recall Figure 5.2). For both the real and imaginary parts, the closer to the classical limit the choice of c_p, the greater the discrepancy between it and the semiclassical-limit case ($c_p = 0.05$), as we would expect. The number of sampling trajectories for each value of c_p is provided in Table 5.2. Focusing on the real part of $\langle K_0^\dagger BG \rangle$, the

Table 5.2: Number of semiclassical trajectories used to evaluate $\langle K_0^\dagger BG \rangle$ at short times for different values of c_p in the MQC-IVR. In all instances, $c_q = 1000$.

c_p	N_{traj}
0.05	6.0×10^7
0.1	6.0×10^7
1.0	4.8×10^7
5.0	4.8×10^7
10	4.8×10^7
100	4.8×10^7

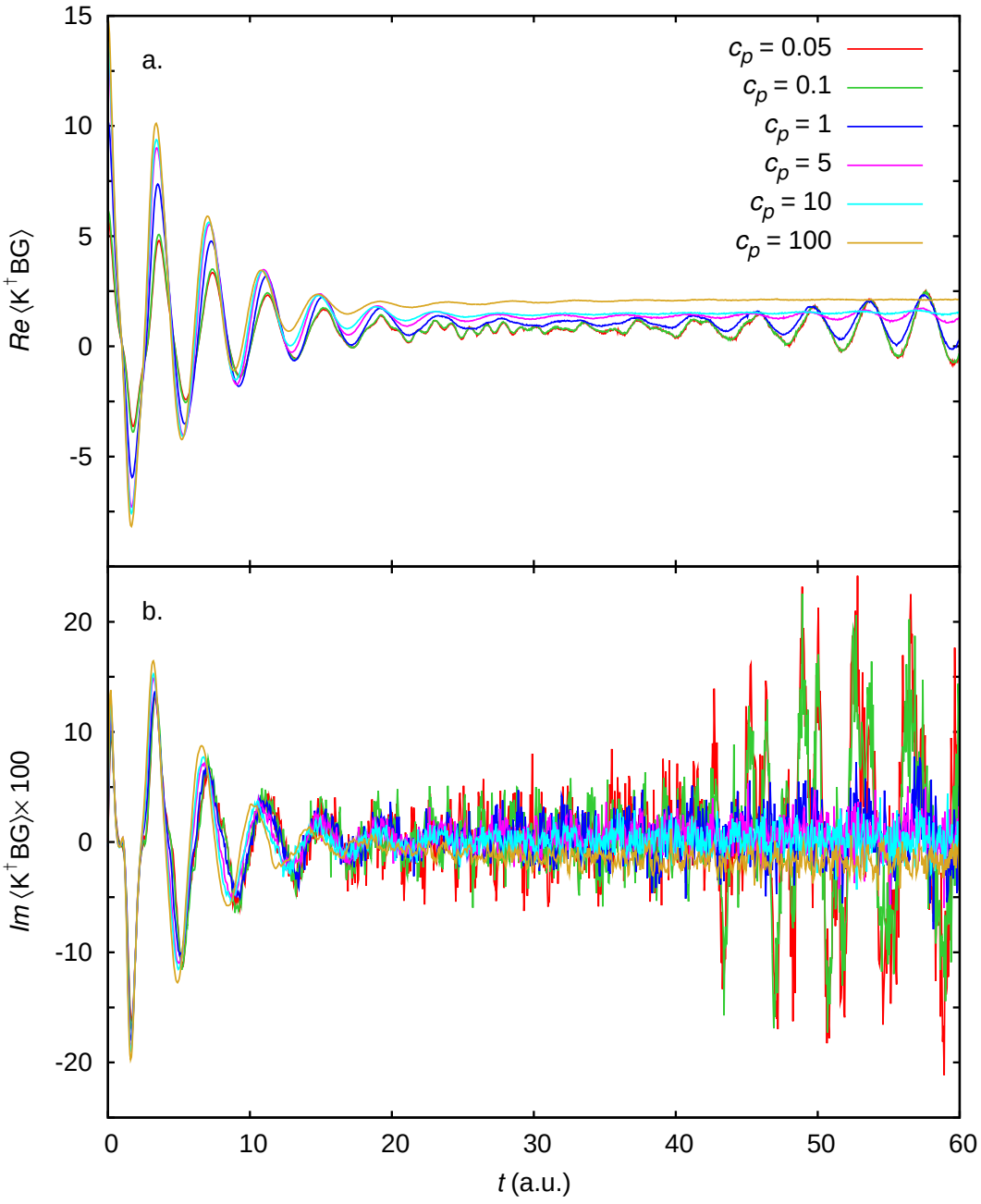

Figure 5.8: The (a.) real and (b.) imaginary part of the correction term $\langle K_0^\dagger BG\rangle$ plotted for $\gamma_t = \gamma_0 = \sqrt{2}$, $c_p = 1000$, and 0.05 (red), 0.1 (green), 1 (blue), 5 (magenta), 10 (cyan), and 100 (gold).

larger c_p, the greater its magnitude at short times as well as average at long times. We note that the more classical the treatment, the greater the loss in the amplitude of the oscillations relative to those at short times; whereas the semiclassical-limit starts with about half the oscillatory amplitude as the classical case, it maintains an oscillatory structure much longer, exhibiting recurrences almost half the original amplitude at later times. For the imaginary part, the discrepancy between different levels of tuning is far less pronounced at early times than at long times. However, at long times, we again only see ample recurrences of the oscillations for c_p values near those of the full semiclassical-limit ($c_p \leq 1$).

Figure 5.9 makes evident a dependence on the choice of coherent state width at time t on $\langle K_0^\dagger BG\rangle$, computed now using $\gamma_t = 10$. By comparing the results found using two different values of γ_t, both of which employed the same number of MC sampled points, we see that not only does the magnitude of the correction depend on this parameter, but perhaps more notably, that the statistical error present in the former ($\gamma_t = \gamma_0$) case is far greater than that for a slightly larger choice. This indicates that sampling efforts required to calculate this correction term to the same level of precision between different choices of γ_t may vary significantly, and one should consider the optimization of this parameter, however, this is not the focus of this work. Herein, we will focus our attention on the real part of the correction, $\mathrm{Re}\langle K_0^\dagger BG\rangle$, because it is both more well-behaved and we seek the error relative to the full semiclassical-limiting case, such that the fact that it spends less time in the vicinity of zero than the imaginary part should prove advantageous.

To try and better quantify the error between different levels of approximation within the MQC-IVR, we examine the time average of the absolute value of the

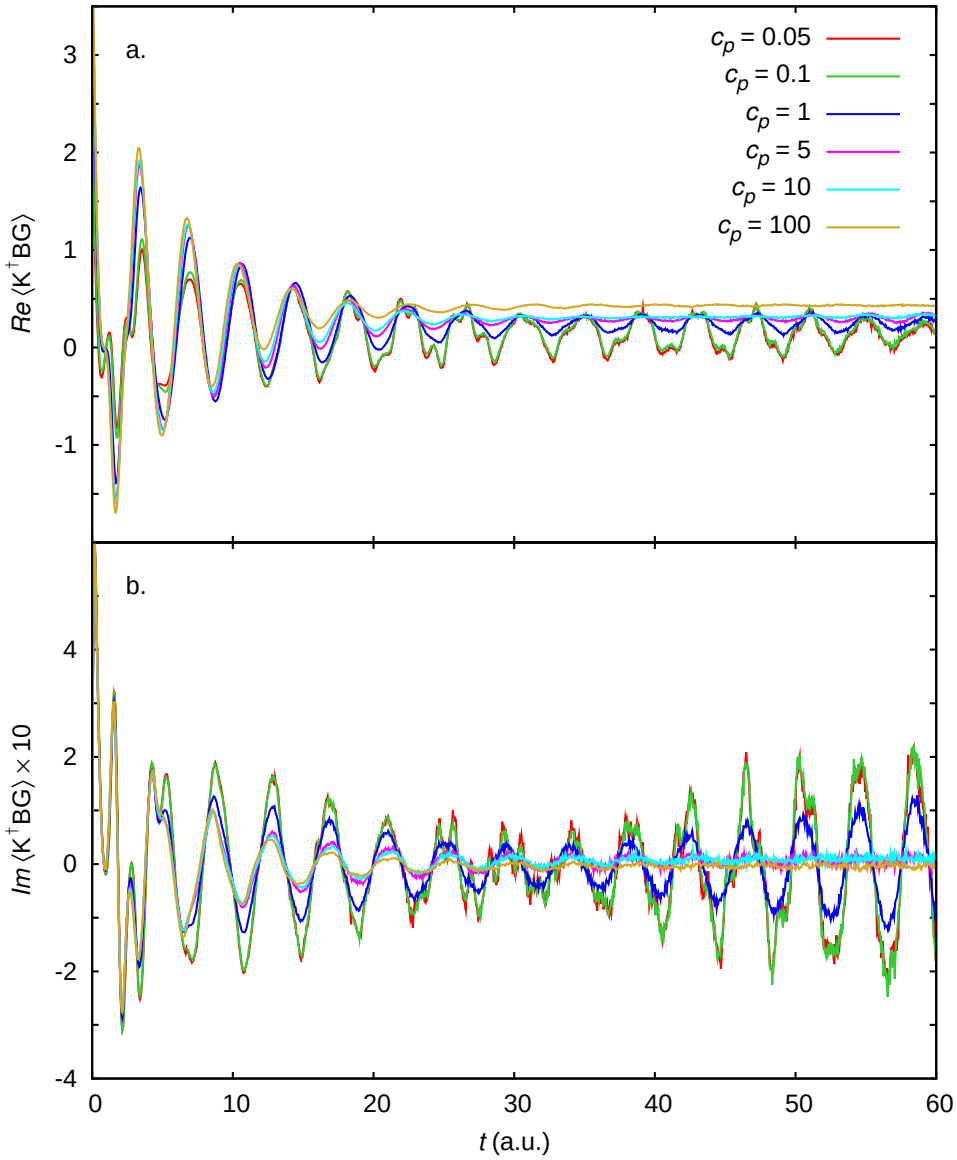

Figure 5.9: The (a.) real and (b.) imaginary part of the correction term $\langle K_0^\dagger BG\rangle$ plotted for $\gamma_t = 10$, $c_q = 1000$, and $c_p = 0.05$ (red), 0.1 (green), 1 (blue), 5 (magenta), 10 (cyan), and 100 (gold).

correction term's relative error:

$$\overline{\Delta E}_{\tilde{c}}(t) = \frac{1}{t}\int_0^t dt' \, |\Delta E_{\tilde{c}}(t')|, \tag{5.59}$$

where $\tilde{c}$ represents the set (c_q, c_p) of MQC-IVR tuning parameters being compared to the (full semiclassical) reference case $\mathrm{Re}\langle K_0^\dagger BG\rangle_{\mathrm{X}}$ with the relative error defined as

$$\Delta E_{\tilde{c}} = \frac{\mathrm{Re}\langle K_0^\dagger BG\rangle_{\mathrm{X}} - \mathrm{Re}\langle K_0^\dagger BG\rangle_{\tilde{c}}}{\mathrm{Re}\langle K_0^\dagger BG\rangle_{\mathrm{X}}}. \tag{5.60}$$

In Figure 5.10, where we have used $\tilde{c} = (c_q, c_p) = (1000, 0.05)$, the time average of the relative error $\overline{\Delta E}_{\tilde{c}}(t)$ agrees well with the previous qualitative assessment for each choice of the coherent state width. The magnitude of the correction increases with increasing c_p, or the level of approximation in the MQC-IVR treatment, as one might expect. Each begins at about $\Delta E_{\tilde{c}}(t) < 2$, and in general, increases readily, steadies out over intermediate times, and then grows again at late times, in the region where recurrences are seen in the more quantum limits of the MQC-IVR approximation to $\langle x_1(t)\rangle$ (see Figure 5.2). Comparing the trends seen between Figures 5.10 a. and b., we do note that the $\gamma_t = 10$ case shows a greater dependence on the c_p value used at later times than when $\gamma_t = \gamma_0 = \sqrt{2}$. Because each set here was calculated with respect to its $c_p = 0.05$, using the particular γ_t indicated and not referenced to the same point, we do not compare the absolute magnitudes of each treatment.

We now expand this analysis to try and better understand the less intuitive, mixed-limit cases of the MQC-IVR for this simple anharmonic oscillator model where now *both* tuning parameters dictating the magnitude of the 'jumps' (in position and momentum) at time t are varied. For the sake of brevity when dealing with many parameter combinations (γ_t, c_q, c_p), instead of plotting the $\overline{\Delta E}_{\tilde{c}}$ as a function over all time, we instead examine at specific points in time.

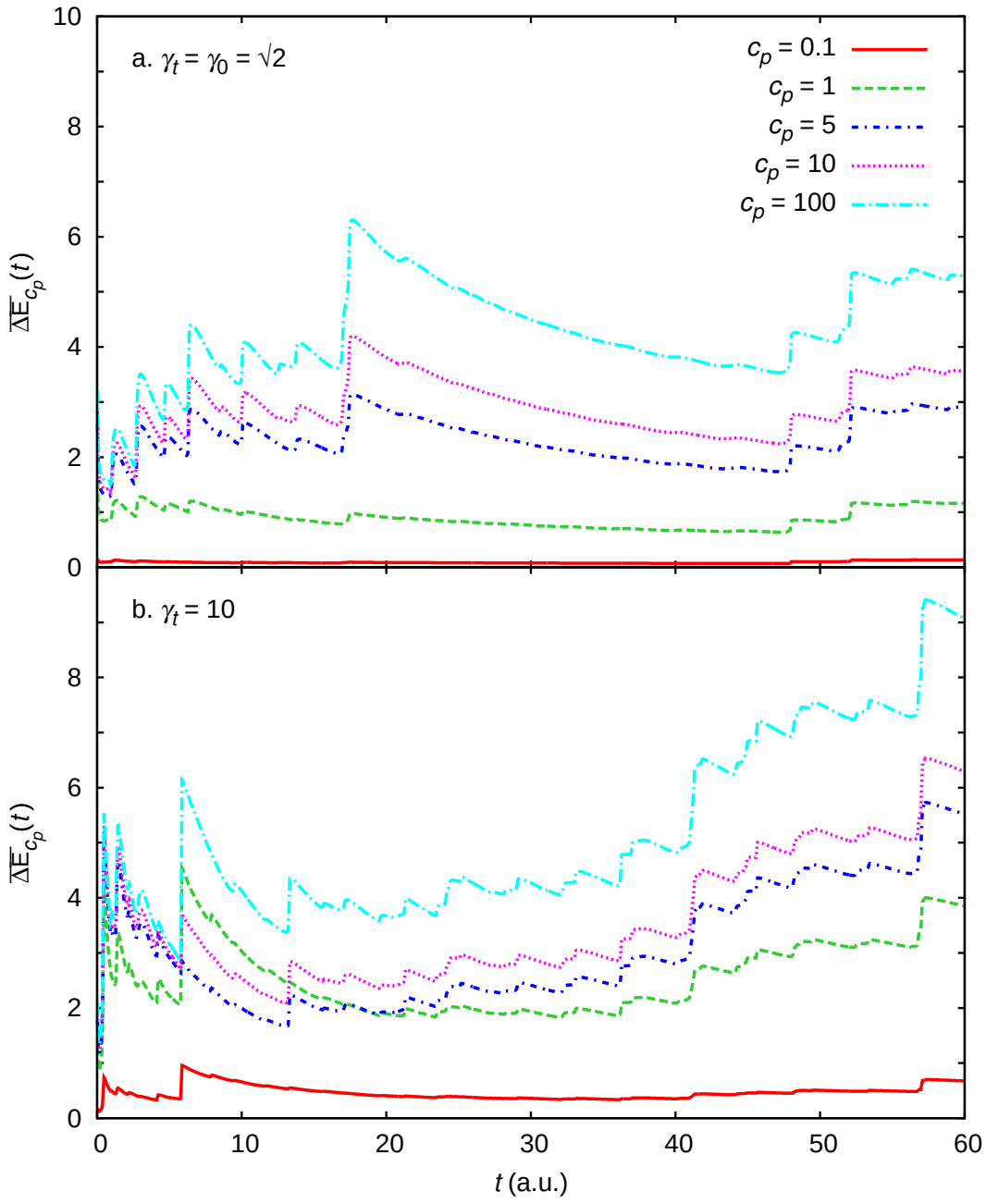

Figure 5.10: The relative error $\overline{\Delta E}_{\tilde{c}}(t)$ is shown for (a.) $\gamma_t = \gamma_0 = \sqrt{2}$ and (b.) $\gamma_t = 10$ where $c_q = 1000$ and $c_p = 0.1$ (solid red), 1 (dashed green), 5 (dot-dashed blue), 10 (dotted magenta), and 100 (dot-long dashed cyan).

In Figure 5.11, we consider all possible combinations of $c_q = 0.1, 1, 5, 1000$ with $c_p = 0.05, 0.1, 1, 5, 10, 100$ using $\gamma_t = \gamma_0$ at time points $t = 0, 10, 20$ and 30 a.u. Each combination is referenced with respect to the $c_q = c_p = 0.05$ with the same γ_t. Herein, all values computed used 60×10^6 MC points, except for the reference sets which employed 90×10^6 trajectories. The cells associated with each one of these combinations is shaded according to the value of $\overline{\Delta E}_{\tilde{c}}$ it holds to aid in their comparison.

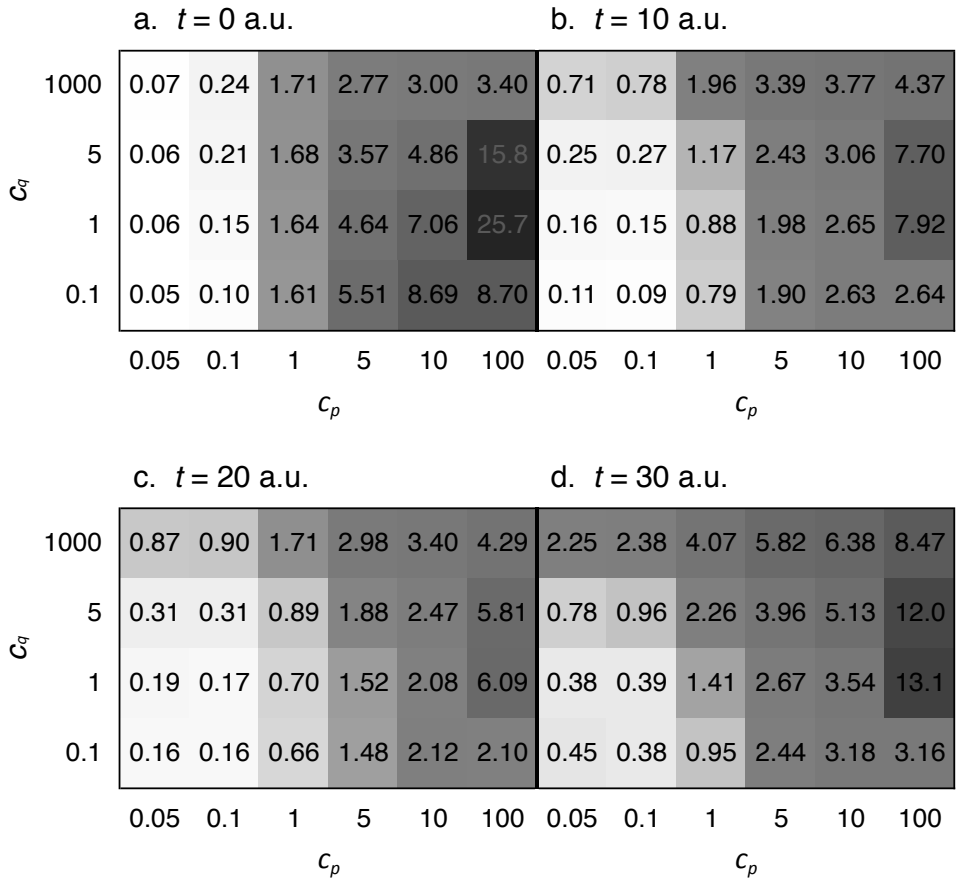

Figure 5.11: Time slice values of the relative error $\overline{\Delta E}_{\tilde{c}}$ with $\gamma_t = \gamma_0 = \sqrt{2}$ for (a.) $t = 0$ a.u., (b.) $t = 10$ a.u., (c.) $t = 20$ a.u., and (d.) $t = 30$ a.u.

A first obvious trend we see here is that the lower the tuning parameters, the greater it retains the structure of the reference case, maintaining low numbers for

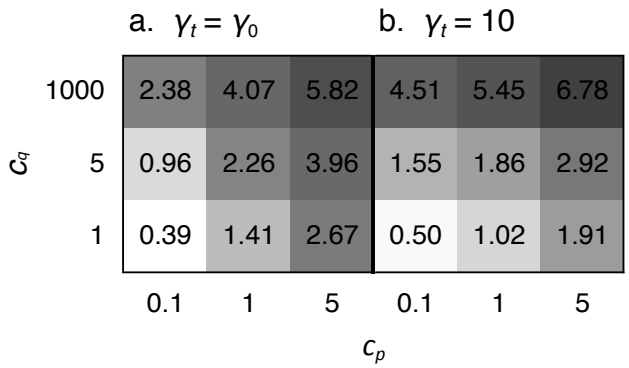

Figure 5.12: The relative error $\overline{\Delta E}_{\tilde{c}}$ at $t = 30$ a.u. for (a.) $\gamma_t = \gamma_0$ and (b.) $\gamma_t = 10$ computed using various sets (c_q, c_p).

all times observed. The time averaged error is clearly more strongly dependent on the value of c_p than c_q, which intuitively makes sense: the position is what is being measured by the correlation function, which can be simplified by enforcing that $\gamma_t \to \infty$ in the coherent state at time t. Without introducing any approximation, this renders one possible form of the correlation function independent of the jump associated with c_q, as was done in the original MQC-IVR work [2]. In light of this point, we note that the outliers, especially those in the initial time slice (Figure 5.11 a.), are likely artifacts of sampling a less physical situation, when large jumps in position (small c_q) are much larger than those in momentum (large c_p). Based on the values of the relative error at longer times (Figure 5.11 d.), the combination $c_q = 1$ and $c_p = 0.1$ would provide optimal results when considering both the relative error as well as the fact that the number of necessary MC points needed for convergence grows with decreasing tuning parameter values. We note that while generally speaking, these trends could have been predicted, this approach enables us to extract a quantified measure of the error at nearly no computational cost.

Guided by Figure 5.11, we choose a subset of tuning parameter combinations

to further explore this γ_t-dependence. In Figure 5.12, we compare the $t = 30$ a.u. values of the correction computed earlier with $\gamma_t = \gamma_0 = \sqrt{2}$, to ones where $\gamma_t = 10$. The trend of increasing error with increasing tuning parameters is maintained for this alternative choice of γ_t. Moreover, by comparing the difference between the time-sliced values of the relative error between the choice of $c_q = 1$ and $c_q = 5$ for each value of c_p, we see that for increasingly classical choices of the tuning parameter, the deviation increases steadily for $\gamma_t = \gamma_0$, but not $\gamma_t = 10$. This indicates a greater dependence on c_q in the case of $\gamma_t = \gamma_0$ than $\gamma_t = 10$. To validate this analysis for comparing tuning parameter choices for a given coherent state width, we return to evaluating the MQC-IVR real-time correlation function (now without using the infinite limit of the width), to confirm that the trends indicated by the relative error computed from the correction term are consistent with that we would see if we calculated the correlation function directly. We emphasize that, without using the same reference correction across different choices of γ_t, we are unable to comment on the relative error between them. However, for a given γ_t, this still provides a means to compare choices of the tuning parameters.

In Figure 5.13, we plot the average position estimated by the MQC-IVR approach for the one-dimensional anharmonic oscillator introduced above for $15 \leq t \leq 30$ a.u. (in the interest of clarity). Comparing the information provided by the time slice values of the relative error at 30 a.u. presented in Figure 5.12 to that gleaned from manual inspection of Figure 5.13, we see good agreement. Figure 5.12 indicates that for $\gamma_t = \gamma_0$, the sets of (c_q, c_p) can be ordered by increasing error as (1, 0.1), (5, 0.1), (1, 1), (5, 1), (1, 5), and (5, 5), in good agreement with Figure 5.13 a. For $\gamma_t = 10$, Figure 5.12 indicates a slight deviation from that trend, where and (5.0, 0.1) and (1, 1) are switched in order. Visually, it is difficult to discern due to the finer structure present on the oscillations in the more

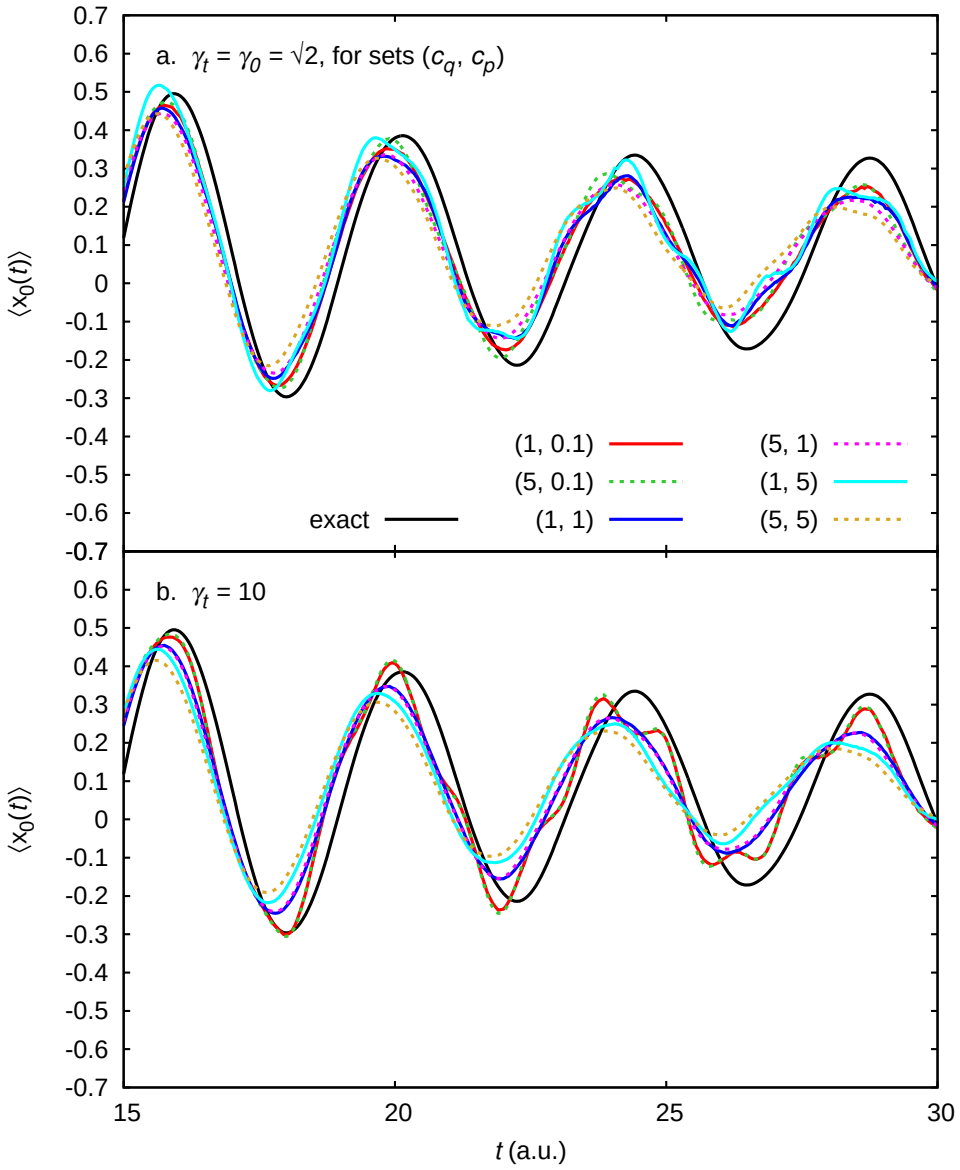

Figure 5.13: The average position $\langle x_0(t) \rangle$ of the one-dimensional anharmonic oscillator evaluated according to the MQC-IVR with (a.) $\gamma_t = \gamma_0$ and (b.) $\gamma_t = 10$ for the sets (c_q, c_p): (1, 0.1) (solid red), (5, 0.1) (dashed green), (1, 1) (solid blue), (5, 1) (dashed magenta), (1, 5) (solid cyan), and (5, 5) (dashed gold), compared to the exact result (solid black).

semiclassical-limit choices of tuning parameters, underscoring the necessity for a quantitative measure of the error. Moreover, $\gamma_t = \gamma_0$ has a greater dependence on the choice of c_q, whereas in the $\gamma_t = 10$, there appears to be minimal deviation (the dashed lines follow closely on the solid line of the same c_p). Notably, Figure 5.12 predicted this same behavior, which serves as further confirmation that the correction term derived here is able to systematically quantify the error in the MQC-IVR.

5.4 Conclusions & Future Directions

The advantage of using the MQC-IVR of the real-time correlation function to describe chemical processes is the ability to treat, within a consistent dynamic framework, a system consisting of both quantum- and classically-behaving components in a way that reduces the computational expense compared to the (generally intractable) quantum or full semiclassical-limit approach. Here, we derive a correction term that reports on the approximation nature of the MQC-IVR and enables us to further explore the mixed-limit regime. We demonstrate this approach as a way to quantify the error inherent in different choices of simulation parameters.

While the first order, physical correction term to the position correlation function proved infeasible for our purposes here, it may still prove useful for alternative systems. If the physical correction were of interest, one may want to consider using the second approach to optimize it with respect to the coherent state width, or to first identify regions of the parameter space they want to more closely explore as it is a much faster calculation.

The second approach we pursued proved to be more fruitful. As we saw, the

relative error metric that we defined using the correction term of a reference point (taken near the full semiclassical limit) proves at least a qualitative way to predict the same trends in parameter choices that the correlation function itself exhibited. While it can be used to compare the choice of tuning parameters, one setback of this approach is the inability to compare between choices of the coherent state width (γ_t). Ideally, we would like to devise a consistent reference point from which we could determine the error metric without having to resort to knowledge of the exact result. Addressing this point is an obvious next step in this work. Future extensions of this work could include looking into optimal c_p and c_q combinations at times greater than those looked at here, and for alternative model systems such as those of higher dimensions, to confirm that the trends follow intuitively.

Another important aspect of these calculations that was not deeply explored in the initial analysis of either approach to quantifying the error in the MQC-IVR is the computational cost. An alternative to the fFB integration (*e.g.*, a triple forward trajectory) scheme carried out to compute the first order, physical correction to the correlation function may prove more efficient. An extension of the second approach taken here to quantify the MQC-IVR error, which comes at almost no additional cost to the correlation function computation, might incorporate the number of MC sampling points necessary to reach convergence into a metric similar to $\overline{\Delta E}$ computed here.

APPENDIX A

CHAPTER 2 SUPPLEMENTARY INFORMATION

A.1 $Co(NH_3)_6^{3+}$ Optimization for Partial Charges

As described in the text, Mulliken analysis from gas-phase density functional theory is used to assign partial charges to the atoms of the TMC for the atomistic simulations. Using the Gaussian 09 [89] software package, the complex is optimized using the M06 hybrid functional [90] with the 6-31G(d,p) basis set [92] for N and H atoms and the LANL2DZ [91] basis set for Co. The resulting optimized structure is provided in Table A1. The computed energy at this configuration is -483.282740937 hartrees. Partial charges on H atoms from the Mulliken analysis were summed into the N to which they are bonded, and those net partial charges are averaged over each of the N atoms to achieve a total charge of +3 e on $Co(NH_3)_6{}^{3+}$. The resulting partial charges used in the simulation are +0.41281 e on Co and +0.43119 e on N.

A.2 Force Field Parameters for Atomistic Simulations

A.3 Solvent Relaxation Timescales

We demonstrate the ability of the approach outlined in this work to provide insight into solvent relaxation timescales. Defining a collective coordinate ΔU reminiscent of the solvent coordinate in Marcus theory [13], the energy difference between the

Table A1: Optimized $Co(NH_3)_6{}^{3+}$ geometry

atom type	x (Å)	y (Å)	z (Å)
Co	0.000192	0.000106	-0.000008
N	1.275211	-0.743840	1.357761
N	-1.280279	0.657544	-1.397605
N	1.159948	1.624901	-0.193382
N	-1.035952	0.985046	1.406268
N	-1.150609	-1.617457	0.288628
N	1.031384	-0.906287	-1.461649
H	0.954795	-0.687125	2.330209
H	1.469827	-1.741134	1.217457
H	2.200171	-0.300657	1.367293
H	-1.562368	-0.075561	-2.057387
H	-2.164499	1.026081	-1.030941
H	-0.920427	1.407129	-1.997678
H	0.720576	2.417464	-0.673103
H	1.456396	2.012570	0.708929
H	2.035037	1.469386	-0.705342
H	-1.268573	1.945628	1.131574
H	-1.938671	0.562311	1.648358
H	-0.555137	1.092274	2.305603
H	-2.100953	-1.540449	-0.089489
H	-0.785633	-2.487385	-0.113283
H	-1.286385	-1.839099	1.280812
H	1.970246	-1.220781	-1.193406
H	0.585346	-1.741836	-1.854485
H	1.187132	-0.301032	-2.275043

diabatic electronic states within the tight binding approximation is expressed as:

$$\Delta U(\mathbf{Q}) = -\frac{e}{4\pi\varepsilon_0}\sum_{k=1}^{N}\left(\frac{\mathrm{q_k}}{|\mathbf{Q}_\mathrm{D}-\mathbf{Q}_k|}-\frac{\mathrm{q_k}}{|\mathbf{Q}_\mathrm{A}-\mathbf{Q}_k|}\right). \tag{A.1}$$

Here, q_k the charge on solvent atom k, and $\mathbf{Q}_\mathrm{D}$, $\mathbf{Q}_\mathrm{A}$, and $\mathbf{Q}_k$ positions of the "donor" Co center, "acceptor" Co center, and solvent atom k, respectively. Time resolving the autocorrelation of ΔU provides insight into the relaxation time of the solvent environment. In this study, an initial relaxation time of about 300 fs is indicated (Fig. A1), consistent with solvent relaxation on the same timescale of our electronic transition (shown by κ in Fig. 2.5 in the main text), followed by a second longer relaxation mechanism that extends beyond the simulation time.

Table A2: Simulation Force Field Parameters

atom types	potential type[a]	parameter	value
Co-N	harmonic bond[b]	k_b[c]	352.5
		r_0	1.94 Å
Co-N	rigid bond[d]	$r^{\ddagger}$	2.05 Å
N-H	rigid bond	r	1.03 Å
Co-N-H	harmonic angle	k_θ[e]	30
		θ_0	114°
H-N-H	harmonic angle	k_θ[e]	44
		θ_0	104°
O-N	12-6	A^f	8.78×10^5
		B^g	7.83×10^2
H_{SPC}-N	12-6	A^f	6.09×10^2
		B^g	15.3
N-N	12-6	A^f	1.32×10^6
		B^g	1.03×10^3

[a] Functional forms of the potentials appropriate for the provided parameters are in accordance with the CHARMM [93] convention. [b] Parameter adapted from Ref. [56]; [c] harmonic bond force constant reported in units of kcal/mol $Å^{-2}$; [d] observed simulated transition state bond length in agreement with previously reported value [64, 73]; [e] harmonic angle force constant reported in units of kcal/mol rad^{-2}; [f] van der Waals 12-6 A parameter reported in units of kcal/mol $Å^{12}$; [g] van der Waals 12-6 B parameter reported in units of kcal/mol $Å^6$.

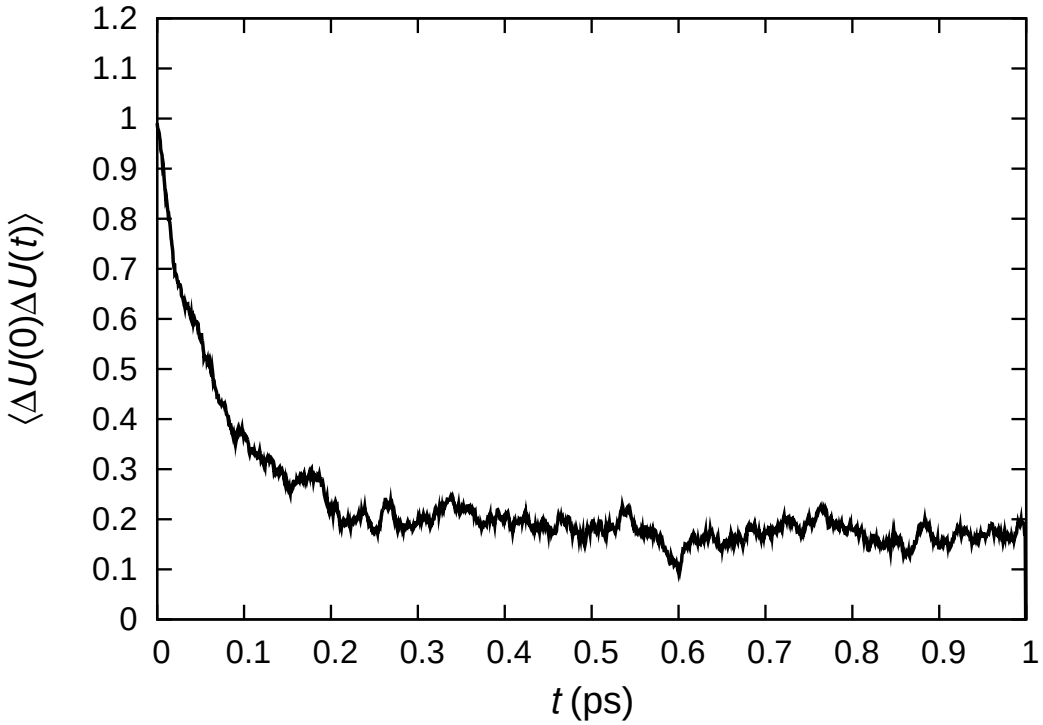

Figure A1: The normalized autocorrelation function of ΔU Eq. A.1 along RPMD trajectory time.

APPENDIX B

MODIFICATIONS TO THE DL_POLY SOURCE CODE

Here we present the necessary modifications made to the DL_POLY source code as described in the text of Chapter 3 above.[1] The variables introduced to the DL_POLY code are defined below:

- `Nbeads` — the total number of beads that make up the ring polymer
- `p`, `q` — matrices of the x, y, and z components of each bead's momentum and position
- `RPmass` — the mass of the beads associated with the kinetic term of the ring polymer Hamiltonian (can be fictitious when sampling statistical properties)
- `matrix` — the elements of the matrix which time evolves the ring polymer bead momenta and positions exactly (in the normal mode representation)
- `twown` — $2\omega_n$, where ω_n is defined below Eqn. 2.5 in Ch. 2
- `pi_n` — pi divided by the number of beads ($\pi/Nbeads$)
- `wk` — $2\omega_n \sin(k\pi/Nbeads)$; Note: k is referred to above in Ch. 3 as μ
- `wt` — $2\omega_n \sin(k\pi/Nbeads) \times \Delta t$
- `wm` — $2\omega_n \sin(k\pi/Nbeads) \times RPmass$
- `chg1`, `chg2`, `rcutX` — the charge on the first atom type, the second atom type, and the short range, electrostatic cutoff distance, respectively
- `fb`, `fbdes`, `difffb` — the current value of the bead count coordinate, the desired value, and their difference, respectively

[1] The adapted code along with sample input files are available on the Ananth group cluster Astra at /home/common/pi_poly.

- `kfb` — the force constant of the harmonic sampling constraint on the bead count coordinate
- `gammaifb`, `gammajfb`, `gammakfb` — the x, y, and z components of the force due to the bead count constraint

B.1 Performing the Mixed Time Evolution Scheme

We provide a snippit of code here from NVE_0_VV.F90 is provided which carries out the mixed time evolution scheme described in Chapter 3, Section 3.2.1. First, we loop over all atoms (`natms`) except for the last $n =$ `Nbeads` atoms in the simulation to update their velocities and positions in accordance with the standard VV algorithm.

```
Subroutine nve_0_vv                                    &
  (isw,lvar,mndis,mxdis,mxstp,tstep,strkin,engke,      &
  imcon,mxshak,tolnce,megcon,strcon,vircon,            &
  megpmf,strpmf,virpmf)
.
.
.
! first VV stage for classically treated particles
Do i = 1, (natms-Nbeads)
  If (weight(i) > 1.0e-6_wp) Then
    tmp=hstep/weight(i)
    vxx(i)=vxt(i)+tmp*fxt(i)
    vyy(i)=vyt(i)+tmp*fyt(i)
    vzz(i)=vzt(i)+tmp*fzt(i)
    xxx(i)=xxt(i)+tstep*vxx(i)
    yyy(i)=yyt(i)+tstep*vyy(i)
    zzz(i)=zzt(i)+tstep*vzz(i)
  End If
End Do
```

Next, we update *only* the bead momentums (velocities) conventionally,

```
! first VV stage for RP beads
do i = (natms - Nbeads + 1), natms
  p(1,i-natms+Nbeads) = vxx(i) * weight(i)
  p(2,i-natms+Nbeads) = vyy(i) * weight(i)
  p(3,i-natms+Nbeads) = vzz(i) * weight(i)
  q(1,i-natms+Nbeads) = xxt(i)
  q(2,i-natms+Nbeads) = yyt(i)
  q(3,i-natms+Nbeads) = zzt(i)
end do
```

the subroutine FFTBEADSTEPS is called,

```
call FFTbeadsteps(p, q, Nbeads, RPmass, tstep)
```

and then the bead momenta are half stepped according to the updated forces

```
! second VV stage
do i = (natms - Nbeads + 1), natms
  vxx(i) = p(1,i-natms+Nbeads) / weight(i)
  vyy(i) = p(2,i-natms+Nbeads) / weight(i)
  vzz(i) = p(3,i-natms+Nbeads) / weight(i)
  xxx(i) = q(1,i-natms+Nbeads)
  yyy(i) = q(2,i-natms+Nbeads)
  zzz(i) = q(3,i-natms+Nbeads)
end do
.
.
.
End Subroutine nve_0_vv
```

Within the FFTBEADSTEPS subroutine, the transformation to the normal mode representation takes place, the beads are evolved exactly, according to the free RP Hamiltonian, and then the transformation back to the bead representation takes place before returning to the NVE_0_VV.F90 subroutine:

```
Subroutine FFTbeadsteps(p, q, Nbeads, mass, dt)
```

```
.
.
.
! FFT --> transform to normal mode representation
do i = 1, 3
  call rfft(p(i, :), Nbeads)
  call rfftq(q(i, :), Nbeads)
end do

matrix(1,1) = 1.0_wp
matrix(2,1) = 0.0_wp
matrix(3,1) = dt/mass/stepfactor
matrix(4,1) = 1.0_wp

if (Nbeads .gt. 1) then
  ! calculate 2*omega_n up front given n (Nbeads),
  ! T, bead mass (mass)
  twown = 2.0_wp * Nbeads * kBToverhBar &
          * sqrt(5.48579909E-04/mass/Nbeads)
  pi_n  = pi/Nbeads

  ! (when Nbeads = 8, this is for beads 2-5):
  do k = 1, Nbeads/2
    wk      = twown * sin(k * pi_n)
    wt      = wk * dt/stepfactor
    wm      = wk * mass
    cos_wt  = cos(wt)
    sin_wt  = sin(wt)

    matrix(1,k+1) = cos_wt
    matrix(2,k+1) = -wm * sin_wt
    matrix(3,k+1) = sin_wt/wm
    matrix(4,k+1) = cos_wt
  end do

  ! (when Nbeads = 8, this is for beads 8-6):
  do k = 1, (Nbeads - 1)/2
    matrix(1,Nbeads-k+1) = matrix(1,k+1)
    matrix(2,Nbeads-k+1) = matrix(2,k+1)
    matrix(3,Nbeads-k+1) = matrix(3,k+1)
    matrix(4,Nbeads-k+1) = matrix(4,k+1)
  end do
end if
```

```
do k = 1, Nbeads ! updating the momenta and positions
  do i = 1, 3
    p_new  = p(i,k) * matrix(1,k) + q(i,k) * matrix(2,k)
    q(i,k) = p(i,k) * matrix(3,k) + q(i,k) * matrix(4,k)
    p(i,k) = p_new
  end do
end do

! inverse FFT --> transform back to Cartesian space
  do i = 1, 3
    call irfft(p(i, :), Nbeads)
    call irfftq(q(i, :), Nbeads)
  end do
.
.
.
End Subroutine FFTbeadsteps
```

A sample subroutine (RFFT) which utilizes the FFTW3 package for transformation of the bead momenta to the normal mode representation is provided below:

```
! perform FFTs with FFTW3

Subroutine rfft(momentum,N)
use kinds_f90

implicit none

! must point the cluster to the fftw library
include '/usr/include/fftw3.f'

integer, intent(in) :: N
real (kind = wp), intent(inout) :: momentum(N)
integer, parameter :: Nmax = 1024
integer :: Np
real (kind = wp) :: copy1a(Nmax), copy1b(Nmax)
real (kind = wp) :: factor
integer*8 :: plan1          ! (recommended in guide)

data Np /0/
save copy1a, copy1b, factor, plan1, Np
```

```
if (N .ne. Np) then
  if (Np .ne. 0) call dfftw_destroy_plan(plan1)
  call dfftw_plan_r2r_1d(plan1, N, copy1a,
       copy1b, FFTW_FORWARD, FFTW_MEASURE)
  factor = sqrt(1.0_wp/N)
  Np = N
end if

copy1a(1:N) = momentum
call dfftw_execute(plan1, copy1a, copy1b)
momentum = factor * copy1b(1:N)

End Subroutine rfft
```

B.2 Including the Energy of the Bead-Bead Interaction

In order to include the bead-bead harmonic 'bond' interaction energy in the total system energy of the simulation, a new functional **bdbd** is defined where only the energy is computed; because the force due to this interaction is accounted for in the normal mode propagation scheme, it is not included here. The code associated with this addition is included below:

```
Else If (keyb == 24) Then  ! bd-bd harmonic 'bond' definition
  k  = prmbnd(1,kk)
  r0 = prmbnd(2,kk)
  dr = rab-r0

  term  = k*dr
  omega = term*0.5_wp*dr

! this only used with normal mode propagation:
  gamma = 0.0_wp
! if not using normal mode propagation:  gamma = -term/rab
```

Notably, when this 'bond' functional is called between non-neighboring beads with

the bond parameter k set to null, we ensure electrostatics are neglected in all bead-bead interactions.

B.3 Imposing Short-ranged Cutoffs on Attractive Electrostatic Interactions

Below, we present the code appended to the VDW_FORCES.F90 subroutine that ensures oppositely charged atoms do not effectively "stick" to one another by introducing short-ranged cutoffs to their interactions.

```
! read in the charge of both atom types and then
! the short range cutoff from FIELD input file:
chg1  = prmvdw(1,k)
chg2  = prmvdw(2,k)
rcutX = prmvdw(3,k)

! subtracting off the force-shifted coulombic
! interaction and correcting for r <= rcutX:
If (rrr .le. rcutX) Then

    If (jatm <= natms .or. idi < ltg(jatm)) &
    eng   = chg1*chg2*r4pie0/epsq/engunit &
            *(1/rcutX - 1/rrr - rrr/rvdw**2 + 2/rvdw)
    gamma = -chg1*chg2*r4pie0/epsq/engunit &
            *(1/rrr - rrr/rvdw**2)/rsq

End If
```

We remind the reader that this implementation assumes a direct treatment of the vdW interactions.

B.4 Efficient Sampling of the Electron Transfer Reaction Coordinate

An example of the code added to the DL_POLY subroutine VDW_FORCES.F90 that enables sampling along the progress of the electron transfer process is provided below for the bead count reaction coordinate, f_b:

```
Else If (ityp == 38) Then  ! bead count (fb) 'vdW'
  difffb   = 0.0_wp
  fb       = 0.0_wp
  gammaifb = 0.0_wp
  gammajfb = 0.0_wp
  gammakfb = 0.0_wp

  Do gr = (natms-Nbeads+1), natms
    fb = 1.0_wp/(Nbeads*2.0_wp) &
         *(Tanh(bfb*zzz(gr))+1.0_wp) + fb
  Enddo

  ! recalling fb parameters from FIELD file:
  kfb    = prmvdw(1,k)
  fbdes  = prmvdw(2,k)
  difffb = fb - fbdes

  ! must divide out factor of 1024
  ! since calling as gh-bead interaction
  term = kfb * difffb  / (Nbeads * 1.0_wp)
  If (jatm <= natms .or. idi < ltg(jatm)) &
    eng=term*0.5_wp*difffb ! harmonic

  ! updating the forces:
  Do gr = (natms-Nbeads+1), natms
    gammakfb = -kfb/(2.0_wp*Nbeads)*bfb &
               *((1.0_wp/Cosh(bfb*zzz(gr)))**2) &
               *difffb
    ! updating the forces on each atom, avoiding
    ! double-counting by dividing out Nbeads
    fxx(gr) = fxx(gr)  ! no x or y force components
    fyy(gr) = fyy(gr)
```

```
  fzz(gr) = fzz(gr) + gammakfb/(Nbeads*1.0_wp)
Enddo
```

BIBLIOGRAPHY

[1] Rachel L. Kenion and Nandini Ananth. Direct simulation of electron transfer in the cobalt hexammine (II/III) self-exchange reaction. *Phys. Chem. Chem. Phys.*, 18(37):26117–26124, 2016.

[2] Sergey V. Antipov, Ziyu Ye, and Nandini Ananth. Dynamically consistent method for mixed quantum-classical simulations: A semiclassical approach. *J. Chem. Phys.*, 142(18):184102, 2015.

[3] Scott Habershon, David E. Manolopoulos, Thomas E. Markland, and Thomas F. Miller III. Ring-polymer molecular dynamics: Quantum effects in chemical dynamics from classical trajectories in an extended phase space. *Annu. Rev. Phys. Chem.*, 64(1):387–413, 2013.

[4] Thomas F. Miller III and David E. Manolopoulos. Quantum diffusion in liquid para-hydrogen from ring-polymer molecular dynamics. *J. Chem. Phys.*, 122(18):184503, 2005.

[5] Thomas F. Miller III and David E. Manolopoulos. Quantum diffusion in liquid water from ring polymer molecular dynamics. *J. Chem. Phys.*, 123(15):154504, 2005.

[6] Thomas F. Miller III. Isomorphic classical molecular dynamics model for an excess electron in a supercritical fluid. *J. Chem. Phys.*, 129(19):194502, 2008.

[7] Thomas E. Markland, Scott Habershon, and David E. Manolopoulos. Quantum diffusion of hydrogen and muonium atoms in liquid water and hexagonal ice. *J. Chem. Phys.*, 128(19):194506, 2008.

[8] Scott Habershon, Thomas E. Markland, and David E. Manolopoulos. Competing quantum effects in the dynamics of a flexible water model. *J. Chem. Phys.*, 131(2):024501, 2009.

[9] Thomas E. Markland, Joseph A. Morrone, Bruce J. Berne, Kunimasa Miyazaki, Eran Rabani, and David R. Reichman. Quantum fluctuations can promote or inhibit glass formation. *Nat. Phys.*, 7(2):134–137, 2011.

[10] Ian R. Craig and David E. Manolopoulos. Chemical reaction rates from ring polymer molecular dynamics. *J. Chem. Phys.*, 122(8):084106, 2005.

[11] Ian R. Craig and David E. Manolopoulos. A refined ring polymer molecular dynamics theory of chemical reaction rates. *J. Chem. Phys.*, 123(3):034102, 2005.

[12] Rosana Collepardo-Guevara, Ian R. Craig, and David E. Manolopoulos. Proton transfer in a polar solvent from ring polymer reaction rate theory. *J. Chem. Phys.*, 128(14):144502, 2008.

[13] Artur R. Menzeleev, Nandini Ananth, and Thomas F. Miller III. Direct simulation of electron transfer using ring polymer molecular dynamics: comparison with semiclassical instanton theory and exact quantum methods. *J. Chem. Phys.*, 135:074106–1–074106–17, 2011.

[14] Yury V. Suleimanov, Rosana Collepardo-Guevara, and David E. Manolopoulos. Bimolecular reaction rates from ring polymer molecular dynamics: Application to H+ $CH_4 \rightarrow H_2$+ CH_3. *J. Chem. Phys.*, 134(4):044131, 2011.

[15] Nicholas Boekelheide, Romelia Salomón-Ferrer, and Thomas F. Miller. Dynamics and dissipation in enzyme catalysis. *Proc. Natl. Acad. Sci.*, 108(39):16159–16163, 2011.

[16] Yury V. Suleimanov. Surface diffusion of hydrogen on Ni (100) from ring polymer molecular dynamics. *J. Phys. Chem. C*, 116(20):11141–11153, 2012.

[17] Joshua S. Kretchmer and Thomas F. Miller III. Tipping the balance between concerted versus sequential proton-coupled electron transfer. *Inorg. Chem.*, 55(3):1022–1031, 2016.

[18] Peter L. Walters and Nancy Makri. Quantum–classical path integral simulation of ferrocene–ferrocenium charge transfer in liquid hexane. *J. Phys. Chem. Lett.*, 6(24):4959–4965, 2015.

[19] C.A. Bignozzi, R. Argazzi, R. Boaretto, E. Busatto, S. Carli, F. Ronconi, and S. Caramori. The role of transition metal complexes in dye sensitized solar devices. *Coord. Chem. Rev.*, 257:1472–1492, 2013.

[20] Wanchun Xiang, Fuzhi Huang, Yi-Bing Cheng, Udo Bach, and Leone Spiccia. Aqueous dye-sensitized solar cell electrolytes based on the cobalt(II)/(III) tris(bipyridine) redox couple. *Energy Environ. Sci.*, 6:121–127, 2013.

[21] Simon Mathew, Aswani Yella, Peng Gao, Robin Humphry-Baker, Basile F. E. Curchod, Negar Ashari-Astani, Ivano Tavernelli, Ursula Rothlisberger,

Md. Khaja Nazeeruddin, and Michael Grätzel. Dye-sensitized solar cells with 13% efficiency achieved through the molecular engineering of porphyrin sensitizers. *Nat. Chem.*, 6:242–247, 2014.

[22] Sadig Aghazada, Peng Gao, Aswani Yella, Gabriele Marotta, Thomas Moehl, Joël Teuscher, Jacques-E Moser, Filippo De Angelis, Michael Grätzel, and Mohammad Khaja Nazeeruddin. Ligand engineering for the efficient dye-sensitized solar cells with ruthenium sensitizers and cobalt electrolytes. *Inorg. Chem.*, 55(13):6653–6659, 2016.

[23] Kazuhiko Maeda, Kentaro Teramura, Daling Lu, Nobuo Saito, Yasunobu Inoue, and Kazunari Domen. Noble-metal/Cr_2O_3 core/shell nanoparticles as a cocatalyst for photocatalytic overall water splitting. *Angew. Chem.*, 118(46):7970–7973, 2006.

[24] Stephan W. Kohl, Lev Weiner, Leonid Schwartsburd, Leonid Konstantinovski, Linda J. W. Shimon, Yehoshoa Ben-David, Mark A. Iron, and David Milstein. Consecutive thermal H_2 and light-induced O_2 evolution from water promoted by a metal complex. *Science*, 324(5923):74–77, 2009.

[25] Qiushi Yin, Jeffrey Miles Tan, Claire Besson, Yurii V. Geletii, Djamaladdin G. Musaev, Aleksey E. Kuznetsov, Zhen Luo, Ken I. Hardcastle, and Craig L. Hill. A fast soluble carbon-free molecular water oxidation catalyst based on abundant metals. *Science*, 328(5976):342–345, 2010.

[26] Rafael E. Rodríguez-Lugo, Mónica Trincado, Matthias Vogt, Friederike Tewes, Gustavo Santiso-Quinones, and Hansjörg Grützmacher. A homogeneous transition metal complex for clean hydrogen production from methanol–water mixtures. *Nat. Chem.*, 5(4):342–347, 2013.

[27] Jonah W. Jurss, Rony S. Khnayzer, Julien A. Panetier, Karim A. El Roz, Eva M. Nichols, Martin Head-Gordon, Jeffrey R. Long, Felix N. Castellano, and Christopher J. Chang. Bioinspired design of redox-active ligands for multielectron catalysis: effects of positioning pyrazine reservoirs on cobalt for electro- and photocatalytic generation of hydrogen from water. *Chem. Sci.*, 6:4954–4972, 2015.

[28] Kai Golibrzuch, Nils Bartels, Daniel J. Auerbach, and Alec M. Wodtke. The dynamics of molecular interactions and chemical reactions at metal surfaces: Testing the foundations of theory. *Annu. Rev. Phys. Chem.*, 66:399–425, 2015.

[29] Rudolph A. Marcus and Norman Sutin. Electron transfers in chemistry and biology. *BBA - Reviews on Bioenergetics*, 811(3):265–322, 1985.

[30] Harry B. Gray and Jay R. Winkler. Electron transfer in proteins. *Annu. Rev. Biochem.*, 65:537–561, 1996.

[31] Steven Y. Reece and Daniel G. Nocera. Proton-coupled electron transfer in biology: Results from synergistic studies in natural and model systems. *Annu. Rev. Biochem.*, 78:673–699, 2009.

[32] Mats H. M. Olsson, Ulf Ryde, and Bjrn O. Roos. Quantum chemical calculations of the reorganization energy of blue-copper proteins. *Protein Sci.*, 7(12):2659–2668, 1998.

[33] Emma Sigfridsson, Mats H. M. Olsson, and Ulf Ryde. Inner-sphere reorganization energy of ironsulfur clusters studied with theoretical methods. *Inorg. Chem.*, 40(11):2509–2519, 2001.

[34] Xenia Amashukeli, Nadine E. Gruhn, Dennis L. Lichtenberger, Jay R. Winkler, and Harry B. Gray. Inner-sphere electron-transfer reorganization energies of zinc porphyrins. *J. Am. Chem. Soc.*, 126(47):15566–15571, 2004. PMID: 15563186.

[35] Qin Wu and Troy Van Voorhis. Direct calculation of electron transfer parameters through constrained density functional theory. *J. Phys. Chem. A*, 110(29):9212–9218, 2006.

[36] Sabyasachi Bandyopadhyay, Atanu Rana, Kaustuv Mittra, Subhra Samanta, Kushal Sengupta, and Abhishek Dey. Effect of axial ligand, spin state, and hydrogen bonding on the inner-sphere reorganization energies of functional models of cytochrome p450. *Inorg. Chem.*, 53(19):10150–10158, 2014.

[37] Paul F. Barbara, Thomas J. Meyer, and Mark A. Ratner. Contemporary issues in electron transfer research. *J. Phys. Chem.*, 100(31):13148–13168, 1996.

[38] Antonín Vlček and Stanislav Záliš. Modeling of charge-transfer transitions and excited states in d6 transition metal complexes by DFT techniques. *Coord. Chem. Rev.*, 251(3):258–287, 2007.

[39] Bruce S. Brunschwig, Stanton Ehrenson, and Norman Sutin. Solvent reorga-

nization in optical and thermal electron-transfer processes. *J. Phys. Chem.*, 90(16):3657–3668, 1986.

[40] Yi-Ping Liu and Marshall D. Newton. Solvent reorganization and donor/acceptor coupling in electron-transfer processes: self-consistent reaction field theory and ab initio applications. *J. Phys. Chem.*, 99(33):12382–12386, 1995.

[41] C. L. Kneifel, M. D. Newton, and H. L. Friedman. Simulation of solvent isotope effects on aqueous ferrous and ferric ions. *J. Mol. Liq.*, 60(1):107–145, 1994.

[42] Claudio Amovilli, Vincenzo Barone, Roberto Cammi, Eric Cancès, Maurizio Cossi, Benedetta Mennucci, Christian S Pomelli, and Jacopo Tomasi. Recent advances in the description of solvent effects with the polarizable continuum model. *Adv. Quantum Chem.*, 32:227–261, 1998.

[43] Shuqiang Niu and Michael B. Hall. Theoretical studies on reactions of transition-metal complexes. *Chem. Rev.*, 100(2):353–406, 2000.

[44] Paolo Carloni, Ursula Rothlisberger, and Michele Parrinello. The role and perspective of ab initio molecular dynamics in the study of biological systems. *Acc. Chem. Res.*, 35(6):455–464, 2002.

[45] Carles Bo and Feliu Maseras. QM/MM methods in inorganic chemistry. *Dalton Trans.*, (22):2911–2919, 2008.

[46] J. Caro and L. L. Salcedo. Impediments to mixing classical and quantum dynamics. *Phys. Rev. A*, 60(2):842–852, 1999.

[47] Jaroslaw J. Szymczak, Franziska D. Hofmann, and Markus Meuwly. Structure and dynamics of solvent shells around photoexcited metal complexes. *Phys. Chem. Chem. Phys.*, 15:6268–6277, 2013.

[48] Akshaya K. Das, Rajadurai Vijay Solomon, Franziska Hofmann, and Markus Meuwly. Inner-shell water rearrangement following photoexcitation of tris (2, 2'-bipyridine) iron (II). *J. Phys. Chem. B*, 120(1):206–216, 2016.

[49] H. Azzouz and D. Borgis. Quantum simulation study of proton-transfer reactions in solution: from a molecular to a stochastic description. *J. Mol. Liq.*, 61(1):17–36, 1994.

[50] Lowell W. Ungar, Marshall D. Newton, and Gregory A. Voth. Classical and

quantum simulation of electron transfer through a polypeptide. *J. Phys. Chem. B*, 103(34):7367–7382, 1999.

[51] Paul V. Bernhardt and Peter Comba. Molecular mechanics calculations of transition metal complexes. *Inorg. Chem.*, 31(12):2638–2644, 1992.

[52] Peter Comba and Achim F. Sickmüller. Modeling of redox properties of (Hexaamine)cobalt(III/II) couples. *Inorg. Chem.*, 36(20):4500–4507, 1997.

[53] Clark R. Landis, Thomas Cleveland, and Timothy K. Firman. Valence bond concepts applied to the molecular mechanics description of molecular shapes. 3. applications to transition metal alkyls and hydrides. *J. Am. Chem. Soc.*, 120(11):2641–2649, 1998.

[54] Timothy K. Firman and Clark R. Landis. Valence bond concepts applied to the molecular mechanics description of molecular shapes. 4. transition metals with π-bonds. *J. Am. Chem. Soc.*, 123(47):11728–11742, 2001.

[55] J-K. Hwang, S. Creighton, G. King, D. Whitney, and A. Warshel. Effects of solute–solvent coupling and solvent saturation on solvation dynamics of charge transfer reactions. *J. Chem. Phys.*, 89(2):859–865, 1988.

[56] Chong Zheng, J. Andrew McCammon, and Peter G. Wolynes. Quantum simulation of nuclear rearrangement in electron transfer reactions. *Proc. Natl. Acad. Sci. U.S.A.*, 86(17):6441–6444, 1989.

[57] Bruce S. Brunschwig and Norman Sutin. Energy surfaces, reorganization energies, and coupling elements in electron transfer. *Coord. Chem. Rev.*, 187(1):233–254, 1999.

[58] Norman Sutin. Theory of electron transfer reactions: insights and hindsights. *Prog. Inorg. Chem*, 30:441–498, 1983.

[59] David Chandler and Peter G. Wolynes. Exploiting the isomorphism between quantum theory and classical statistical mechanics of polyatomic fluids. *J. Chem. Phys.*, 74(7):4078–4095, 1981.

[60] Robert A. Kuharski, Joel S. Bader, David Chandler, Michiel Sprik, Michael L. Klein, and Roger W. Impey. Molecular model for aqueous ferrous–ferric electron transfer. *J. Chem. Phys.*, 89(5):3248–3257, 1988.

[61] Massimo Marchi and David Chandler. Path-integral calculation of the tunnel splitting in aqueous ferrous–ferric electron transfer. *J. Chem. Phys.*, 95(2):889–894, 1991.

[62] M. Parrinello and A. Rahman. Study of an F center in molten KCl. *J. Chem. Phys.*, 80(2):860–867, 1984.

[63] Sven Larsson, Kenny Stąhl, and Michael C. Zerner. Hexaamminecobalt electron-self-exchange reaction. *Inorg. Chem.*, 25(17):3033–3037, 1986.

[64] R. G. Endres, M. X. LaBute, and D. L. Cox. Theory of adiabatic hexaamminecobalt self-exchange. *J. Chem. Phys.*, 118(19):8706–8714, 2003.

[65] D. R. Stranks. Mechanisms of some electron exchange reactions. *Faraday Discuss.*, 29:73–79, 1960.

[66] N. S. Biradar, D. R. Stranks, and M. S. Vaidya. Kinetics of isotopic exchange reactions. part 7.-electron exchange between cobaltic hexammine and cobaltous ammines. *Trans. Faraday Soc.*, 58:2421–2432, 1962.

[67] Ephraim Buhks, Mordechai Bixon, Joshua Jortner, and Gil Navon. The hexaamminecobalt electron-exchange reaction. *Inorg. Chem.*, 18(7):2014–2018, 1979.

[68] Bruce S. Brunschwig, Carol Creutz, Donal H. Macartney, T-K. Sham, and Norman Sutin. The role of inner-sphere configuration changes in electron-exchange reactions of metal complexes. *Faraday Discuss. Chem. Soc.*, 74:113–127, 1982.

[69] D. Geselowitz and H. Taube. Reexamination of the $Co(NH_3)_6^{3+/2+}$ self-exchange reaction. *Adv. Inorg. Bioinorg. Mech.*, 1:391–407, 1982.

[70] Anders Hammershoi, Daniel Geselowitz, and Henry Taube. Redetermination of the hexaaminecobalt (III/II) electron-self-exchange rate. *Inorg. Chem.*, 23(7):979–982, 1984.

[71] Comparison of electron-transfer matrix elements for transition-metal complexes: $t(_{2g}$.

[72] Marshall D. Newton. Electronic structure analysis of electron-transfer matrix elements for transition-metal redox pairs. *J. Phys. Chem.*, 92(11):3049–3056, 1988.

[73] Marshall D. Newton. The $Co(NH_3)_6$ exchange reaction: ground-state versus thermally excited pathways. *J. Phys. Chem.*, 95(1):30–38, 1991.

[74] Dongju Zhang, Yongjun Liu, Haiquan Hu, and Chengbu Liu. Inner-sphere reorganization for redox pairs $M(NH_3)_6^{2+/3+}$ (M = Mn, Fe, and Co): Models and calculations. *Int. J. Quant. Chem*, 86(5):468–477, 2002.

[75] M. X. LaBute, R. G. Endres, and D. L. Cox. An Anderson impurity model for efficient sampling of adiabatic potential energy surfaces of transition metal complexes. *J. Chem. Phys.*, 121(17):8221–8230, 2004.

[76] Richard Phillips Feynman, Albert R Hibbs, and Daniel F Styer. *Quantum mechanics and path integrals*. Courier Corporation, 2005.

[77] Bart De Raedt, Michiel Sprik, and Michael L. Klein. Computer simulation of muonium in water. *J. Chem. Phys.*, 80(11):5719–5724, 1984.

[78] Ian R. Craig and David E. Manolopoulos. Quantum statistics and classical mechanics: Real time correlation functions from ring polymer molecular dynamics. *J. Chem. Phys.*, 121(8):3368–3373, 2004.

[79] Timothy J. H. Hele, Michael J. Willatt, Andrea Muolo, and Stuart C. Althorpe. Boltzmann-conserving classical dynamics in quantum time-correlation functions:matsubara dynamics. *J. Chem. Phys.*, 142(13):134103, 2015.

[80] Timothy J. H. Hele, Michael J. Willatt, Andrea Muolo, and Stuart C. Althorpe. Communication: Relation of centroid molecular dynamics and ring-polymer molecular dynamics to exact quantum dynamics. *J. Chem. Phys.*, 142(19):191101, 2015.

[81] Timothy J. H. Hele. *Quantum transition-state theory*. Dissertation, University of Cambridge, 2014.

[82] Daan Frenkel and Berend Smit. *Understanding Molecular Simulation*. Academic Press, California, USA, 2 edition, 2002.

[83] G. M. Torrie and J. P. Valleau. Nonphysical sampling distributions in monte carlo free-energy estimation: Umbrella sampling. *J. Comput. Phys.*, 23(2):187–199, 1977.

[84] Shankar Kumar, John M. Rosenberg, Djamal Bouzida, Robert H. Swendsen, and Peter A. Kollman. The weighted histogram analysis method for free-energy calculations on biomolecules. i. the method. *J. Comput. Chem.*, 13(8):1011–1021, 1992.

[85] William Humphrey, Andrew Dalke, and Klaus Schulten. Vmd: visual molecular dynamics. *J. Mol. Graph.*, 14(1):33–38, 1996.

[86] Charles L. Brooks, B. Montgomery Pettitt, and Martin Karplus. Structural and energetic effects of truncating long ranged interactions in ionic and polar fluids. *J. Chem. Phys.*, 83(11):5897–5908, 1985.

[87] Ilian T. Todorov, William Smith, Kostya Trachenko, and Martin T. Dove. Dl_poly_3: new dimensions in molecular dynamics simulations via massive parallelism. *J. Mater. Chem.*, 16(20):1911–1918, 2006.

[88] Herman J. C. Berendsen, James P. M. Postma, Wilfred F. van Gunsteren, and Jan Hermans. Interaction models for water in relation to protein hydration. In *Intermolecular forces*, pages 331–342. Springer, 1981.

[89] M. J. Frisch, G. W. Trucks, H. B. Schlegel, G. E. Scuseria, M. A. Robb, J. R. Cheeseman, G. Scalmani, V. Barone, B. Mennucci, G. A. Petersson, H. Nakatsuji, M. Caricato, X. Li, H. P. Hratchian, A. F. Izmaylov, J. Bloino, G. Zheng, J. L. Sonnenberg, M. Hada, M. Ehara, K. Toyota, R. Fukuda, J. Hasegawa, M. Ishida, T. Nakajima, Y. Honda, O. Kitao, H. Nakai, T. Vreven, J. A. Montgomery, Jr., J. E. Peralta, F. Ogliaro, M. Bearpark, J. J. Heyd, E. Brothers, K. N. Kudin, V. N. Staroverov, R. Kobayashi, J. Normand, K. Raghavachari, A. Rendell, J. C. Burant, S. S. Iyengar, J. Tomasi, M. Cossi, N. Rega, J. M. Millam, M. Klene, J. E. Knox, J. B. Cross, V. Bakken, C. Adamo, J. Jaramillo, R. Gomperts, R. E. Stratmann, O. Yazyev, A. J. Austin, R. Cammi, C. Pomelli, J. W. Ochterski, R. L. Martin, K. Morokuma, V. G. Zakrzewski, G. A. Voth, P. Salvador, J. J. Dannenberg, S. Dapprich, A. D. Daniels, Ö. Farkas, J. B. Foresman, J. V. Ortiz, J. Cioslowski, and D. J. Fox. Gaussian 09 Revision C.01, 2009.

[90] Y. Zhao and D. G. Truhlar. The M06 suite of density functionals for main group thermochemistry, thermochemical kinetics, noncovalent interactions, excited states, and transition elements: two new functionals and systematic testing of four m06-class functionals and 12 other functionals. *Theor. Chem. Acc.*, 120:215–241, 2008.

[91] P. Jeffrey Hay and Willard R. Wadt. Ab initio effective core potentials for

molecular calculations. potentials for the transition metal atoms Sc to Hg. *J. Chem. Phys.*, 82(1):270–283, 1985.

[92] Warren J. Hehre, Robert Ditchfield, and John A. Pople. Selfconsistent molecular orbital methods. xii. further extensions of gaussiantype basis sets for use in molecular orbital studies of organic molecules. *J. Chem. Phys.*, 56(5):2257–2261, 1972.

[93] A. D. MacKerell Jr., D. Bashford, M. Bellott, Jr. R. L. Dunbrack, J. D. Evanseck, M. J. Field, S. Fischer, J. Gao, H. Guo, S. Ha, D. Joseph-McCarthy, L. Kuchnir, K. Kuczera, F. T. K. Lau, C. Mattos, S. Michnick, T. Ngo, D. T. Nguyen, B. Prodhom, W. E. Reiher, B. Roux, M. Schlenkrich, J. C. Smith, R. Stote, J. Straub, M. Watanabe, J. Wiórkiewicz-Kuczera, D. Yin, and M. Karplus. All-atom empirical potential for molecular modeling and dynamics studies of proteins. *J. Phys. Chem. B*, 102(18):3586–3616, 1998.

[94] LiHong Hu and Ulf Ryde. Comparison of methods to obtain force-field parameters for metal sites. *J. Chem. Theory Comput.*, 7(8):2452–2463, 2011.

[95] Maurus H. Schmid, Thomas R. Ward, and Markus Meuwly. Toward a broadly applicable force field for d_6-piano stool complexes. *J. Chem. Theory Comput.*, 9(5):2313–2323, 2013.

[96] Nedialka Iordanova, Helene Decornez, and Sharon Hammes-Schiffer. Theoretical study of electron, proton, and proton-coupled electron transfer in iron bi-imidazoline complexes. *J. Am. Chem. Soc.*, 123(16):3723–3733, 2001.

[97] Loup Verlet. Computer "experiments" on classical fluids. I. Thermodynamical properties of lennard-jones molecules. *Phys. Rev.*, 159:98–103, Jul 1967.

[98] Hans C Andersen. Rattle: A velocity version of the shake algorithm for molecular dynamics calculations. *J. Comput. Phys.*, 52(1):24–34, 1983.

[99] Michele Ceriotti, Michele Parrinello, Thomas E. Markland, and David E. Manolopoulos. Efficient stochastic thermostatting of path integral molecular dynamics. *J. Chem. Phys.*, 133(12):124104, 2010.

[100] Justine P Roth, Scott Lovell, and James M. Mayer. Intrinsic barriers for electron and hydrogen atom transfer reactions of biomimetic iron complexes. *J. Am. Chem. Soc.*, 122(23):5486–5498, 2000.

[101] Nandini Ananth. Mapping variable ring polymer molecular dynamics: A path-integral based method for nonadiabatic processes. *J. Chem. Phys.*, 139(12):124102, 2013.

[102] Jessica R. Duke and Nandini Ananth. Simulating excited state dynamics in systems with multiple avoided crossings using mapping variable ring polymer molecular dynamics. *J. Phys. Chem. Lett.*, 6(21):4219–4223, 2015.

[103] Jessica Ryan Duke and Nandini Ananth. State space path integrals for electronically nonadiabatic reaction rates, doi: 10.1039/c6fd00123h. *Faraday Discuss.*, 2016.

[104] Artur R. Menzeleev, Franziska Bell, and Thomas F. Miller III. Kinetically constrained ring-polymer molecular dynamics for non-adiabatic chemical reactions. *J. Chem. Phys.*, 140(6):064103, 2014.

[105] Ilian T. Todorov and William Smith. *The DL_POLY User Manual*. version 4.03 available from external link: http://www.ccp5.ac.uk/DL_POLY/.

[106] Matteo Frigo and Steven G. Johnson. The design and implementation of fftw3. *Proceedings of the IEEE*, 93(2):216–231, 2005.

[107] Babak Pashaei, Hahsem Shahroosvand, and Parisa Abbasi. Transition metal complex redox shuttles for dye-sensitized solar cells. *RSC Adv.*, 5:94814–94848, 2015.

[108] Thomas W. Hamann, Florian Gstrein, Bruce S. Brunschwig, and Nathan S. Lewis. Measurement of the dependence of interfacial charge-transfer rate constants on the reorganization energy of redox species at n-ZnO/H_2O interfaces. *J. Am. Chem. Soc.*, 127(40):13949–13954, 2005.

[109] Norman Sutin. *Nuclear and Electronic Factors in Electron Transfer*, chapter 3, pages 25–43. 1991.

[110] Rudolph A. Marcus. Electron transfer reactions in chemistry. Theory and experiment. *Rev. Mod. Phys.*, 65(3):599, 1993.

[111] Rudolph A. Marcus. On the theory of oxidation-reduction reactions involving electron transfer. I. *J. Chem. Phys*, 24(5):966–978, 1956.

[112] W. F. Libby. Theory of electron exchange reactions in aqueous solution. *J. Phys. Chem.*, 56(7):863–868, 1952.

[113] N.S. Hush. Distance dependence of electron transfer rates. *Coord. Chem. Rev.*, 64:135–157, 1985.

[114] Rudolph A. Marcus. Exchange reactions and electron transfer reactions including isotopic exchange. Theory of oxidation-reduction reactions involving electron transfer. Part 4.—A statistical-mechanical basis for treating contributions from solvent, ligands, and inert salt. *Discussions of the Faraday Society*, 29:21–31, 1960.

[115] Mei Chou, Carol Creutz, and Norman Sutin. Rate constants and activation parameters for outer-sphere electron-transfer reactions and comparisons with the predictions of marcus theory. *J. Am. Chem. Soc*, 99(17):5615–5623, 1977.

[116] Michael J. Weaver and Edmund L. Yee. Activation parameters for homogeneous outer-sphere electron-transfer reactions. comparisons between self-exchange and cross reactions using marcus' theory. *Inorg. Chem.*, 19(7):1936–1945, 1980.

[117] Ariela Burg and Dan Meyerstein. Is it always correct to use the marcus cross relation for calculations of electron self-exchange rates? *Inorganica Chimica Acta*, 363(4):737–740, 2010.

[118] Joachim Ankerhold, Markus Saltzer, and Eli Pollak. A study of the semiclassical initial value representation at short times. *J. Chem. Phys.*, 116(14):5925–5932, 2002.

[119] John H. Van Vleck. The correspondence principle in the statistical interpretation of quantum mechanics. *Proc. Natl. Acad. Sci.*, 14(2):178–188, 1928.

[120] Martin C Gutzwiller. *Chaos in Classical and Quantum Mechanics*, volume 1. Springer Science & Business Media, 1991.

[121] Lawrence S. Schulman. *Techniques and applications of path integration*. Courier Corporation, 2012.

[122] William H. Miller. Classical-limit quantum mechanics and the theory of molecular collisions. *Adv. Chem. Phys*, 25(1):69–177, 1974.

[123] Michael F. Herman and Edward Kluk. A semiclasical justification for the use of non-spreading wavepackets in dynamics calculations. *Chem. Phys.*, 91(1):27–34, 1984.

[124] Michael Thoss and Haobin Wang. Semiclassical description of molecular dynamics based on initial-value representation methods. *Annu. Rev. Phys. Chem.*, 55:299–332, 2004.

[125] Kenneth G. Kay. Semiclassical initial value treatments of atoms and molecules. *Annu. Rev. Phys. Chem.*, 56:255–280, 2005.

[126] Xiong Sun and William H. Miller. Forward-backward initial value representation for semiclassical time correlation functions. *J. Chem. Phys.*, 110(14):6635–6644, 1999.

[127] Michael Thoss, Haobin Wang, and William H. Miller. Generalized forward–backward initial value representation for the calculation of correlation functions in complex systems. *J. Chem. Phys.*, 114(21):9220–9235, 2001.

[128] William H. Miller. Including quantum effects in the dynamics of complex (ie, large) molecular systems. *J. Chem. Phys.*, 125(13):132305, 2006.

[129] Nandini Ananth, Charulatha Venkataraman, and William H. Miller. Semiclassical description of electronically nonadiabatic dynamics via the initial value representation. *J. Chem. Phys.*, 127(8):084114, 2007.

[130] Shesheng Zhang and Eli Pollak. Optimization of the semiclassical initial value representation of the exact quantum-mechanical real time propagator. *J. Chem. Phys.*, 119(21):11058–11063, 2003.

[131] Shesheng Zhang and Eli Pollak. A prefactor free semiclassical initial value series representation of the propagator. *J. Chem. Phys.*, 121(8):3384–3392, 2004.

[132] Shesheng Zhang and Eli Pollak. Hybrid prefactor semiclassical initial value series representation of the quantum propagator. *J. Chem. Theory Comput.*, 1(3):345–352, 2005.

[133] Shesheng Zhang and Eli Pollak. Monte carlo method for evaluating the quantum real time propagator. *Phys. Rev. Lett.*, 91:190201, 2003.

[134] Eva Martin-Fierro and Eli Pollak. Forward-backward semiclassical initial value series representation of quantum correlation functions. *J. Chem. Phys.*, 125(16):164104, 2006.